SYMMETRY BREAKING IN CHEMICAL INTERACTIONS

A Dissertation Presented to

the Faculty of the Department of Physics

University of Houston

In Partial Fulfillment

of the Requirements for the Degree

Doctor of Philosophy

By

Jon Golden

December 2016

SYMMETRY BREAKING IN CHEMICAL INTERACTIONS

Jon Golden

APPROVED:

Dr. Vassiliy Lubchenko, Chairman

Dr. Eric Bittner

Dr. Margaret S. Cheung

Dr. Oomman Varghese

Dr. Lowell Wood

Dean, College of Natural Sciences and Mathematics

Acknowledgement

The author wishes to express his sincere gratitude to Dr. Vassiliy Lubchenko for taking him on as a graduate student and providing the opportunity to work on this truly unique and interesting problem. I would also like to thank the members of the theoretical chemistry division, Dr. Eric Bittner, Dr. Dima Bevzenko, Dr. Ho Yin Chan, Vladimir Lankevich, Alexi Lukyanov, Roman Dmietriev and Kush Patel who have made my time here very pleasant.

This work has been supported by the National Science Foundation Grants CHE-0956127, CHE-1465125, the Welch Foundation Grant E- 1765, the Arnold and Mabel Beckman foundation and the Sloan Research Fellowship. The author acknowledges the use of the Maxwell/Opuntia Cluster and the advanced support from the Center of Advanced Computing and Data Systems at the University of Houston and the Texas Advanced Computing Center (TACC) at The University of Texas at Austin for providing HPC resources.

SYMMETRY BREAKING IN CHEMICAL INTERACTIONS

An Abstract of a Dissertation Presented to
the Faculty of the Department of Physics
University of Houston

In Partial Fulfillment
of the Requirements for the Degree
Doctor of Philosophy

By
Jon Golden
December 2016

Abstract

We develop a unified description of the chemical bond, in which distinct types of bonding can be thought of as mediated by electrons with differing degrees of localization. Rooted in the venerable density-functional theory, the present method shows that localized and delocalized electrons can be treated similarly to distinct phases of a single-component substance. Transitions between these phases are accompanied by changes in the translational symmetry and can be either discontinuous or continuous, the control parameters being the density and electronegativity variation. In the present picture, electron-delocalized and localized regimes correspond with the metallic and ionic bond respectively. Coexistence between the two types of bonding corresponds with the multicenter bond. At sufficiently low densities, the multicenter bond undergoes a further symmetry lowering transition resulting in a coexistence of the covalent and closed-shell, secondary interactions.

We discover that symmetry-breaking in the electronic wave function may take place even when the underlying atomic lattice remains symmetric. Such transitions delineate regimes in which the bond-order is well-defined in that it is largely insensitive to bond deformation. We find that if the localized-molecular orbitals cover all nearest-neighbor bonds in a putative structure, the latter is either stable or, at worst, metastable. This finding suggests a high-throughput, automated procedure for screening candidate compounds and structures with regard to stability.

Despite the intrinsically quantum-mechanical nature of electronic bands in solids, the interplay between delocalized and localized electrons is similar to that arising during the classical liquid-to-solid transition. In contrast with classical systems, the metal-insulator transition can be continuous, as we show using both direct modelling

and a coarse-grained, Landau-Ginzburg description. In a yet more dramatic departure from classical systems, quantum-mechanical treatment of degenerate charge-density-wave (CDW) states shows that interfaces between distinct CDW states must host special midgap electronic states. These states are of topological origin and are robust with respect to elastic deformation. Such midgap states are intrinsic to structural glasses and quantitatively account for several puzzling light-induced phenomena in amorphous chalcogenide alloys; the chalcogenides are of interest in applications such as phase-change computer memory.

Contents

Acknowledgement iii

1 Motivation and Brief Summary of the Thesis 1

2 The chemical bond as an emergent phenomenon 12

2.1 Overview 12

2.2 Motivation 13

2.3 Interplay of covalent, secondary, multi-center, and ionic interactions: Small molecules 22

2.4 Hierarchy of chemical interactions: The solid state 35

2.5 Discussion 48

3 Bond assignment as a symmetry breaking 58

3.1 Overview 58

3.2 Motivation 59

3.3 Bonding from the viewpoint of localized molecular orbitals 63

3.4 Symmetry breaking in the bond assignments in small molecules with directed interactions 68

3.5 Bond assignment in a solid 79

3.6 Discussion 87

4 Degenerate charge density waves: miscibility of localized and metallic states 92

4.1 Overview 92
4.2 Motivation 93
4.3 A simple quantum mechanical model of solvation 95
4.4 Miscibility and the metal-insulator transition 105
4.5 Discussion 122

5 Bulk chalcogenides: Vestiges of Broken Symmetry and the Associated Midgap Electronic States 124

5.1 Overview 124
5.2 Chalcogenides as symmetry broken versions of symmetric parent structures 125

6 Summary and Future Work 138

Appendices 144

A Appendix 145

A.1 Potential energy of the AsH_2-AsH-AsH_2 trimer 145
A.2 Fluctuation-induced lowering of the symmetry breaking 146
A.3 Lack of promotion of $3d$ electrons 146
A.4 Dependence of symmetry breaking on the $pp\sigma$ bond electron count . . 147
A.5 Electronegativity variation suppression of the electronic transition . . 147
A.6 Dependence of symmetry breaking on the $pp\sigma$ bond electron count . . 149
A.7 Effects of electronegativity variation 149
A.8 Reparametrization of antimony in PM6 149
A.9 Re-parametrization of MOPAC PM6 basis set under pressure 150
A.10 Locating the transition densities for the simple cubic-to-bcc transition 154
A.11 Hysteretic behavior of the energy as a function of the electronegativity variation 156

A.12 Stability of the simple cubic structure to rhombohedral distortion . . 156

A.13 Ab-initio potential energy surface for the AsH_2-AsH-AsH_2 trimer . . . 158

A.14 Ab-initio verification of electronic symmetry breaking for symmetric AsH_2-AsH-AsH_2 trimer 158

A.15 Absence of MO term crossing during AsH_2-AsH-AsH_2 trimer dilation 159

A.16 Correspondence between two-center LMOs and spatial dimerization in 20 atom ring molecule 159

Bibliography **167**

List of Figures

1.1 Two hypothetical linear molecules, AsH_2-AsH-As_2 shown in panels (a) and (b) and AsH_2-AsH_2-AsH_2 shown in panels (c) and (d), chosen to demonstrate symmetric and symmetry broken ground states. 2

1.2 The 4-electron/3-center bonding configuration from the l.h.s. of Fig. 1.1. Two ways to plot the symmetry breaking behavior as the molecule is uniformly stretched, panel (b) shows the bond length difference, (c) shows individual bond lengths as a function of the overall trimer length 3

1.3 Bond length difference behavior from panel (b) of Figure 1.2 shown in panel (a) for comparison with notional magnetization behavior of the classical Ising model in panel (b), data shown is representative only, magnetization M and temperature T are dimensionless in this figure. 4

1.4 Individual bond length data from panel (c) of Figure 1.1 recast parametrically as $b_2(b_1)$ is shown in panel (a) for comparison with Cl-Sb-Cl trimeric motifs found in the search of solid-state compounds by Landrum and Hoffmann. 5

1.5 Alternative presentation of Landrum and Hoffman data for Br-Sb-Br trimeric motifs showing bond lengths as a function of overall trimer length to highlight evolution of covalent/secondary bonds from the multi-center interaction. 6

1.6 Application of the ZL symmetry breaking structural framework to rhombohedral arsenic. Covalent bonds corresponding to the thick bold lines on the rhombohedral lattice in panel (a) map to what we term "links" on the simple cubic parent structure in panel (b) shows. . . . 7

1.7 Mutually complementary bond order waves in black phosphorus, panel (a) and rhombohedral arsenic, panel (b). Electron density, concentrated in the interatomic regions identified by high bond order would form stripes. 8

1.8 Four examples of crystal structures from the Pn_2Ch_3 group of compounds demonstrating the ambiguity in coordination present in these materials. As_2S_3 sample in panel (a) hosts a strong covalent bonds and weaker secondary bonds at each center. Both Bi and S are 3-coordinated in the stibnite structure shown in panel (c). The As atoms are 6-coordinated while Te has only 3 contacts as seen in the As_2Te_3 structure seen in panel (b). Every atom shown in the Bi_2Te_3 sample in panel (d) is octahedrally coordinated. 9

1.9 Phase diagram for relevant chemical interactions in a binary compound as a function of density and electronegativity. Label "sc" stands for simple cubic and "bcc" for body-centered cubic. 10

1.10 Manifestations of electronic midgap excitations in As_2S_3 as a result of illumination at bandgap frequency. Panel (a) shows density of unpaired spins growing with exposure time. Panel (b) shows appearance of sub-gap absorption following bandgap frequency illumination. . . . 11

2.1 *Left*: The lengths of the two bonds in three-center bonding configurations compiled by Landrum and Hoffman [1]. *Left*: The Landrum-Hoffmann data replotted to show the two bond lengths as functions of the trimer length per bond. 16

2.2 **(a)** Structure of Bi_2Te_3 illustrating coexistence of multicenter, covalent and secondary bonding. **(b)** Structure of As_2S_3 illustrating that the bonding is essentially covalent within the double layers. Sums of pertinent covalent radii are provided for the reader's reference. . . . 19

2.3 Lewis diagrams and the electronic configurations for the three-center $pp\sigma$ bond in the molecule AsH_2-AsH_n-AsH_2 trimer, $n = 0, 1, 2$. The dashed lines for $n = 0$ and $n = 2$ reflect the relative weakness of the $pp\sigma$ bond compared with the four electron configuration, which also happens to obey the Lewis octet rule. 22

2.4 The equilibrium As-As bond bond lengths for the 3/4 case as functions of the overall trimer length, per bond, c.f. right top panel of Fig. 2.1. The energies are calculated using MOPAC and NWChem, see text. The arsenic atoms are constrained to lie on a straight line, while the As-H bonds lie in planes perpendicular to that line. The As-H bonds are fixed at length 1.5 Å ; mutual angle 90° for the terminal bonds, see the inset. The molecule has two reflection planes. 23

2.5 Walsh diagrams showing individual MO energies as functions of the displacement Δb of the central arsenic for the 3/4 trimer As_3H_5. The distance $b_1 + b_2$ between the terminal arsenics is 5.98 Å, which is just below the meanfield symmetry breaking point. The left and right panels show MOPAC PM6 data NWChem, respectively; note the difference in the horizontal ranges. 26

2.6 **(a)** The dependence of the cohesive and repulsive parts of the MOPAC-inferred energy of the 3/4 trimer As_3H_5 on the location of the middle arsenic, with the green and blue dashed lines respectively, in the symmetric state indicated in panel **(b)**. The solid red line shows the total energy; the circle indicate the location of the stable minima. **(c)** Same as (a), but in a symmetry broken configuration. There are two equivalent minima now. Panel **(d)** displays the dependence of the absolute values of the curvatures of the repulsive and cohesive parts at $\Delta b = 0$, on the trimer length. 28

2.7 The solid black line shows the dependence of the MOPAC-inferred cohesive energy as a function of the location of the middle arsenic for the 3/4 trimer As_3H_5. The sum of the MOPAC terms from Fig. 2.5 that stabilize and destabilize the symmetric state shown in green and blue respectively. The individual contribution of the lowest term is shown in red. 29

2.8 The s and p content of the localized molecular orbitals (LMOs), as functions of the trimer length per bond for the 3/4 trimer As_3H_5. The LMOs on the opposite sides of the symmetry breaking are exemplified in the insets. 31

2.9 Same as Fig. 2.8, but for the 3/3 trimer As_3H_6. The vertical dashed line indicates the length at which the spatial symmetry is broken. Note that localized molecular orbitals exhibit a symmetry breaking while the molecule is still symmetric. 32

2.10 The dependences of the bond lengths $b_{1,2}$ for 3/4 trimers XH_2-XH-XH_2 (X = As, Sb, Bi), normalized by the respective critical length b_c, shown as a function of the reduced "per-bond" trimer length $\tilde{b} = (b_1+b_2)/2b_c$. The inset displays the ratio of the critical length in terms of the corresponding covalent and ionic radii for each element. 33

2.11 A number of bifurcation diagrams for pnictogen and chalcogen containin 3/4 trimers shown in reduced coordinates, as in Fig. 2.10. To maintain the 4 electron count, a chalcogen is passivated with one fewer hydrogen than a pnictogen. 34

2.12 The structure of rhombohedral arsenic at normal conditions can be thought of as two face-centered cubic lattices, shown in purple and green, shifted relative to each other along the [111] direction. At sufficiently high pressures, the magnitude of the shift vanishes corresponding to a transition from the rhombohedral to simple-cubic lattice. 37

2.13 Phase diagram of chemical interactions. The abscissa corresponds with the mass density, assuming each atom has the same mass as arsenic. The ordinate gives the absolute value of the electronegativity difference 2ϵ between pseudo-arsenic and pseudo-antimony atoms; the two artificial elements form either the simple-cubic (sc) or body-centered cubic (bcc) structure, by construction; the dashed lines delineate the coexistence of the two phases. The left-bottom corner is occupied by a less-symmetric structure, value of density at ϵ matches that for the transition between rhombohedral and simple-cubic arsenic. See text for explanation of the symbols. 38

2.14 **(a)** A specific instance of term-crossing for the ground state of the pseudo-pnictogen compound from Fig. 2.13. **(b)** The corresponding dependence of the electron density differential $\Delta\rho$ as determined directly using MOPAC-computed density matrix and by numerically differentiating the $E(\epsilon)$ curves from panel (a). The differentiation was performed using the best parabolic fit to the $E(\epsilon)$ curves. Although numerically similar, the two curves are not identical because MOPAC does not solve the Schrödinger equation exactly. In both panels, the horizontal axis ε represents the difference in electronegativity between the two atom types in the solid. In panel (b) the differential quantity $\Delta\rho$ on the vertical axis is derived from the dimensionless electron (probability) density 55

2.15 **(a)** The inherent electronic energy from Eq. (2.5) as a function of the electron density differential $\Delta\rho$, corresponding to Fig. 2.14. **(b)** The modified energy $\widetilde{E}^{(\mathrm{inh})}(\Delta\rho) \equiv E^{(\mathrm{inh})}(\Delta\rho) - \epsilon_0\,\Delta\rho$ whose minima correspond to the equilibrium values of $\Delta\rho$ when the externally imposed electronegativity variation is equal to ϵ_0. 56

2.16 *Left*: The ELF=1/2 surface at the onset of metallicity. *Right*: The ELF=1/2 surface in the metallic regime. In both panels, the metallic and ionic regions are shown as filled and empty region, respectively. The cavities correspond to the ionic cores. 57

3.1 **(a)** Graphical representation of the eigenvectors of the three-orbital Hückel energy function (3.4). **(b)** The localized molecular orbitals (LMOs) corresponding with panel (a). Note that the two orbitals have the same energy, $(E_1 + E_2)/2$. 66

3.2 The trimers AsH_2-AsH-AsH_2 (panel (a)) and AsH_2-AsH_2-AsH_2 (panel (b)), corresponding to 3-center/4-electron and 3-center/3-electron $pp\sigma$ bond. In all figures below except Figs. 3.3, 3.4, and 3.9, $b_1 = b_2$. . . . 69

3.3 The contour plot of the potential energy of the 3/4 trimer, Fig. 3.2(a), as a function of the trimer length per bond $b \equiv (b_1 + b_2)/2$ and the distance of the center arsenic from the midpoint between the terminal arsenics, $\Delta b \equiv (b_1 - b_2)/2$. The stable, symmetric state is marked by the filled red circle, the corresponding equilibrium trimer length is indicated by a thin vertical dashed line. The dashed, bifurcating graph shows the minimum energy at fixed value of b. 70

3.4 The eqilibrium values of the As-As bond lengths for a fixed value of the overal trimer length, according to the dashed line on Fig. 3.3; **(a)** as functions of the trimer length per bond, **(b)** plotted parametrically, for the longer bond vs. the shorter bond. 71

3.5 The bonding contribution of the LMOs as functions of the As-As bond length $b = b_1 = b_2$, for the 3/4 case. 72

3.6 We display, as functions of the As-As bond length $b = b_1 = b_2$: **(a)**, the bond center number for the LMOs from Fig. 3.5; **(b)**, the Wiber bond index. Note the latter is computed using the density matrix and does not rely on the localization procedure. 73

3.7 Scatter plots of the changes in the expansion coefficients of the MOs, **(a)**, and LMOs, **(b)**, upon the symmetry breaking transition in Fig. 3.5, vs. their average values. 75

3.8 The energies of the MOs responsible for the $pp\sigma$ bond and the lone pair on the central arsenic, as functions of the As-As bond length $b = b_1 = b_2$, for the 3/4 case. 76

3.9 The contour plot of the potential energy of the 3/3 trimer, Fig. 3.2(a), as a function of the trimer length per bond $b \equiv (b_1 + b_2)/2$ and the distance of the center arsenic from the midpoint between the terminal arsenics, $\Delta b \equiv (b_1 - b_2)/2$. The metastable symmetric configuration is marked by the filled red circle. The dashed, bifurcating graph shows the minimum energy at fixed value of b. 77

3.10 The bonding contribution of the LMOs as functions of the As-As bond length $b = b_1 = b_2$, for the 3/3 molecule. 78

3.11 We display, as functions of the As-As bond length $b = b_1 = b_2$: **(a)**, the bond center number for the LMOs from Fig. 3.10; **(b)**, the Wiber bond index. Note the latter is computed using the density matrix and does not rely on the localization procedure. 79

3.12 The localized molecular orbitals for the ground state of benzene. . . . 79

3.13 The localized molecular orbitals on the $(AsH_2)_{20}$ ring molecule shown for clarity as two sets. Within each set, the orbitals are equivalent. The density is apprently sufficiently high so that each two-center $pp\sigma$ bond is filled; $b = 2.48\mathring{A}$, bond index = 1.97. 81

3.14 The localized molecular orbitals on the $(AsH_2)_{20}$ at a lower density. The bond length $b = 2.57$, bond index = 1.98. 82

3.15 The LMOs for the 24-member ring $(AsH_2)_{24}$. $b = 3.46\mathring{A}$, bond index = 1.98 83

3.16 64 atom cubic arsenic sample at reduced density showing single chains of localized orbitals along each axis to illustrate how bond assignments in the lattice form a pattern suggestive of rhombohedral geometry . . 84

3.17 64 atom cubic arsenic sample at reduced density showing plane layers of localized bonding orbitals. Frames (a) and (b) show X and Y plane 3 center bond layers respectively. 2-center Z plane shown in (c). . . . 85

3.18 simple cubic lattice with bond connections edited to match metastable black phosphorus structure, a single example of chain localized bond pattern shown for each axis is shown for clarity 86

3.19 a single plane layer of X oriented chains showing the coexistence of a single odd configuration amongst what was formerly a uniformly aligned set forming the black phosphorus type bond pattern. 87

3.20 LMO linear combinations at high density (a) and low density (b). . . 90

4.1 The spectrum of an on-site CDW insulator ($\varepsilon_1 = 1$, $\bar{t}_1 = 1$, $t_1 = 0$, $N_1 = 200$) in contact with a metal ($\varepsilon_2 = 0$, $\bar{t}_2 = 1$, $t_2 = 0$, $N_2 = 250$) is shown in red line with a symbol. The spectra of the standalone components are placed on the graph so as to ease comparison with the spectrum of the combined system. The horizontal axis shows site number along the $N = N_1 + N_2$ member chain. 98

4.2 The "solvation" energy from Eq. (4.3) as a function of ε_1, $N_1 = 100$, $N_2 = 102$. In all cases, $\bar{t}_1 = 1$, $t_1 = t_2 = 0$. 99

4.3 The "solvation" energy from Eq. (4.3) for two bond-order insulators, as a function of t_1. Here, $\varepsilon_1 = \varepsilon_2 = 0$, $t_1 = t_2 = 1$, $t_2 = 0$. *Inset*: The stabilization due to bringing two metals in contact, as a function of $\bar{t}_1$. Here, $\varepsilon_1 = \varepsilon_2 = t_1 = t_2 = 0$, $\bar{t}_2 = 1$. $N_1 = 100$, $N_2 = 102$. 100

4.4 The on-site, P_{ii}, and off-site, $(P_{i,i+1} + P_{i+1,i})$, entries of the density matrix near an interface for the compound system $N_1 = 202$, $N_2 = 200$, $\varepsilon_1 = 0.5$, $\varepsilon_2 = 0$, $\bar{t}_1 = \bar{t}_2 = 1$, $t_1 = t_2 = 0$. *Inset*: The corresponding order parameters from Eq. (4.10) and (4.19). The horizontal axis shows site number for the $N = N_1 + N_2$ member chain. The vertical axis shows dimensionless, on-site electron density values. 101

4.5 The dimensionless overlap between two wave-functions, from Eq. (4.9) for three systems: $N = 22+20$, $102+100$, and $202+200$, as a function of $\varepsilon = \varepsilon_1 = \varepsilon_2$. In the reference system, $\varepsilon = 0$. For both (compound) systems, $\bar{t}_1 = \bar{t}_2 = 1$, $t_1 = 0$, $t_2 = 0.01$. ε and t are dimensionless energy quantities from the tight-binding model in Eq. 4.1 103

4.6 **(a)** The inherent energy corresponding to Eq. (4.1). $\bar{t} = 1$, $t = 0$. Curves 1 and 2 correspond to the bare case and that with an added interaction $A\rho^2/2$, $A = -2$. **(b)** The inherent energy corresponding to Eq. (4.1), $\bar{t} = 1$, $t = 0$, with an added interaction $A\rho^2/2 + C\rho^4/4$, $A = 0.5$. Curves 1, 2, and 3 correspond to $C = -4$, -4.5, and -5.5, respectively. Dimensionless ρ values are represented by the horizontal axis. 109

4.7 The presence of a non-concave portion in the inherent energy $E^{\text{inh}}(\rho)$, c.f. curve 1 from Fig. 4.6(b), corresponds with the presence of two terms in the energy proper, as a function of the electronegativity variance ε. The slopes ε_{1s} and ε_{12s} at the inflection points of the $E^{\text{inh}}(\rho)$ curve correspond with the term ends for the energy $E(\varepsilon)$. The term-crossing becomes genuine in the thermodynamic limit, according to Fig. 4.5. 111

4.8 **(a)** A metastable minimum in $E^{\text{inh}}(\rho)$ is thermodynamically significant when it corresponds to a bulk-degenerate configuration. When $E_{\text{inh}}(-\rho)$ is defined for both signs of ρ and $E_{\text{inh}}(-\rho) = E_{\text{inh}}(\rho)$ (the $\rho < 0$ portion not shown), such a metastable minimum corresponds to a genuine, symmetry-related term-crossing for the actual energy. . 113

4.9 . **(a)** The structures of rhombohedral arsenic, **(a)**, and black phosphorus **(b)**. Two alternative, mutually complementary ways to connect the atoms are shown with thick solid and thin dashed lines, respectively. We have reduced the distortion away from the simple-cubic lattice, compared with the actual structures, for clarity. 116

4.10 The blue and red depict the hexagonal and triangular lattices respectively. The top graphic demonstrates the two lattices mutually complement each other and thus correspond to opposite signs of the order parameter ρ. 118

4.11 A hypothetical, rotationally-symmetric free energy profile as a function of the strength of the charge-density wave, ρ and η standing for the on-site and off-site components, respectively. The semi-circle at the bottom of the potential exemplifies a hypothetical trajectory in the (ρ, η) space for a transition between two distinct CDW states. . . 119

4.12 The contour plot of the energy profile corresponding to Eq. (4.1), Legendre transformed according Eq. (4.13) and with the added penalty for lattice distortion in the form of $1.5\,t^2$. The solid line corresponds with $\epsilon = 0.144$. Quantities represented on both axes are dimensionless. 121

5.1 Cartoon p orbitals superimposed on the rhombohedral lattice for arsenic using the network of $pp\sigma$ bonds to illustrate the system of intersection chains model. On the lattice d and d' indicate the covalent and secondary bond lengths respectively, angles α and β show the deviation from simple cubic geometry, $\alpha \neq 90\,\text{deg}$ and $\beta \neq 180\,\text{deg}$. 125

5.2 Covalent bonding example of parent structure authority. Panels (a) and (b) show elemental As and P relaxing to their native A7 and A17 structures respectively, from the parent structures shown in green. Panel (c) shows As in the metastable black phosphorus as a result of relaxation from the A17 parent structure. 126

5.3 Simple cubic parent structure candidates for all four lattice types found in the group 15-16 binary intermetallics compounds. 127

5.4 1D chain patterns identified in the orpiment crystal structure of As_2Se_3. Double layers in orpiment structure are composed of roughly perpendicular *ladder* patterns like the one shown here. The parent structure for As_2Se_3 developed by ZL contains vacancies. Notional vacancies in the crystal structure are indicated by hollow circles. Pentameric units in As_2Se_3 are terminated by vacancies, only a single 5 atom chain is visible in this small sample. 128

5.5 1D chain patterns identified in a double layer of the stibnite crystal structure of Sb_2Se_3. The symmetry broken pentameric units shown have the trimer-dimer pattern identified in panel (2) of Figure 5.8. . . 128

5.6 1D chain patterns identified in the tetradymite crystal structure of Bi_2Se_3. Apparently octahedral coordinated structure in panel (a) is only slightly symmetry broken as shown by identification of slightly weaker *secondary* bonds in panel (b). This coordination corresponds to the chain dimer-monomer-dimer pattern identified in panel (3) of Figure 5.8 129

5.7 1D chain patterns identified in the Gd_2Cl_3 crystal structure of As_2Te_3. This coordination corresponds to the chain trimer-dimer pattern identified in panel (2) of Figure 5.8 130

5.8 Progression of symmetry breaking in a Te-As-Te-As-Te five atom unit under uniform dilation, starting from high density symmetric pentamer (1) through dimer-monomer-dimer motif (4). 131

5.9 Individual chain defect prescription for an elemental material with dimerized chains such as arsenic. Arsenic cluster on right shows H addition prescription applied to form an over-coordinated defect on central chain. 132

5.10 The results of over and under-coordinated defect stimulation on a single central chain in a small arsenic cluster following geometry optimization with the MOPAC PM6 method. The actual spectrum for each cluster is shown on the right, units for the vertical energy axis are (ev). The dashed outline identifies the defect associated midgap state in each case. 133

5.11 Prototype process for generating coordination defect and associated midgap state in an elemental solid, where relaxation of H passivated parent structure leads to electronic midgap state shown in spectrum on right. 134

5.12 A malcoordination stimulated within a single plane layer of As_2Se_3 by removing a passivating hydrogen to shift the CDW on that pentameric unit to the complementary pattern to break symmetry. Units for the spectrum shown on the right are electron-volts. 134

5.13 Relative energy shifts of the midgap state in response to externally imposed double occupancy. Under-coordinated charged states and their associated geometries are shown in panels (a) and (b). Over-coordinated charged states appear in panels (c) and (d). Energy units for the spectra in the central panel are (ev). 135

5.14 Unpaired spin density in an over-coordinated cluster of elemental arsenic. Spin density units derive from a sum over ψ^2 quantities, so they are dimensionless. 136

5.15 Hydrogen-passivated arsenic selenide cluster, following geometry optimization using NWChem HF method with a double-zeta basis set. Good agreement with crystal coordination is evident in the interior along with only a modest amount of surface reconstruction. 136

5.16 The hydrogen-passivated arsenic selenide parent structure shown in panel (a), following limited geometry optimization using the NWChem HF method with double-zeta basis set. Highlighted atom at top right has one passivating H removed to stimulate an over-coordination defect on the diagonal double chain structure as shown in panel (b). Panel (c) shows a portion of the cluster spectrum, energy units for the vertical axis are ev, the dashed line ellipse identifies the defect associated midgap state. 137

A.1 Potential energy surface for 3/4 trimer AsH_2-AsH_1-AsH_2 as a function of central atom displacement and the chain length per bond. Minimum energy contour shown in bold to highlight symmetry breaking. 145

A.2 Fractional contribution of atomic $3s$ and $3d$ orbitals to a molecular orbital of an arsenic trimer, as a function of atomic separation according to an Orca all-electron HF calculation. [2, 3] 147

A.3 Dimensionless reduced bond lengths for three arsenic trimers, AsH_2-AsH_n-AsH_2 trimer, as functions of the overall dimensionless trimer length per bond, $\tilde{b} = (b_1 + b_2)/2b_c$. The three cases, $n = 0, 1, 2$, correspond to a five, four, and three electron $pp\sigma$ bond, respectively. Both axes are scaled by the corresponding critical bond length b_c. . . 148

A.4 Dimensionless separation length δ between the electronic and spatial transitions, normalized by the critical bond length $b_c^{(\text{spatial})}$ to suppress to the atomic number and size influences, shown as a function of electronegativity variation ε between the terminal and central atoms. . . 149

A.5 Dimensionless reduced bond lengths for three arsenic trimers, AsH_2-AsH_n-AsH_2 trimer, as functions of the overall dimensionless trimer length per bond, $\tilde{b} = (b_1 + b_2)/2b_c$. The three cases, $n = 0, 1, 2$, correspond to a five, four, and three electron $pp\sigma$ bond bond, respectively. Both axes are scaled by the corresponding critical bond length b_c. . . 150

A.6 Bond lengths for several heteronuclear 3/4 trimers XH_2-YH_1-XH_2 and YH_2-XH_1-YH_2, as functions of the overall trimer length per bond. . 151

A.7 Critical lengths for the heteronuclear 3/4 trimers XH_2-YH_1-XH_2 and YH_2-XH_1-YH_2 from Fig. A.6. $b_c^{>}$ and $b_c^{<}$ correspond to the situation where the more electronegative elements is placed in the central and terminal position, respectively. b_c^1 and b_c^1 denote the critical lengths for the homonuclear trimer XH_2-XH_1-XH_2 or YH_2-YH_1-YH_2. 152

A.8 Overlay of s function overlaps as a function of separation for As-As, As-Sb and Sb-Sb bonds. 153

A.9 Overlay of $s-p$ function overlaps as a function of separation for As-As and As-Sb bonds. 154

A.10 Overlay of $p-p$ function overlaps as a function of separation for As-As and As-Sb bonds. 155

A.11 Overlay of $d-d$ function overlaps as a function of separation for As-As, As-Sb and Sb-Sb bonds. 156

A.12 Composition of the p atomic orbital in $pp\sigma$ bonding MO in arsenic trimer as a function of interatomic separation, from ORCA aug-cc-pvtz all electron HF calculations. Dimensionless amplitude-squared values for the five basis functions represented on vertical axis. 157

A.13 Orbital exponent scaling function behavior for simple cubic and body centered cubic lattices, illustrated using the ratio of the scaled exponent $\xi(a)$ to the original PM6 value ξ_0, the dimensionless amount of scaling is represented by the vertical axis. 158

A.14 Linear core-core repulsion pseudo-potential scaling functions for simple cubic and body centered cubic lattices. The amount of dimensionless scaling is represented by the vertical axis. 159

A.15 Maxwell construction determination of the first order simple cubic to bcc phase transition for the pseudo-arsenic material at $\epsilon = 0$. The density index shown on the horizontal axis is an internal variable used in the PM6 calculations to set a common density in both the simple cubic and bcc lattices, the values of 18 and 30 marked with vertical dashed lines correspond to the experimentally observed boundaries of the first order transition. 160

A.16 A sample of the "sweep" protocol demonstrating an overshoot of a term crossing. 161

A.17 Onset of susceptibility to small distortion towards rhombohedral structure marking continuous transition from metallic to multicenter bonding 161

A.18 Energy contour plot obtained from HF solutions using NWChem, for central As displacement as a function of average bond length $b = (b_1 + b_2)/2$. Energy units on color bar are atomic units (a.u.) 162

A.19 Bond length plot obtained for the AsH_2-AsH-AsH_2 trimer from the potential energy surface for displacement of the central As atom. The bond lengths are developed from the minimum energy contour. Circles show semi-empirical PM6 method data, squares represent ab-initio HF data obtained with NWChem using the aug-cc-pvtz-pp basis and small core pseudo-potential. 163

A.20 NBO6 localized molecular orbital analysis within Gaussian09 for symmetric trimer at $b = 3.2$ $\mathring{A}$. 164

A.21 Molecular orbital terms near the HOMO for a symmetric AsH_2-AsH-AsH_2 trimer as it undergoes dilation, b indicates the average bond length per atom above which symmetry is broken. 165

A.22 At high density where every interatomic region hosts a 2-center localized bond orbital, the total energy of the molecule is stable with respect to displacement of every other atom (dimerization). The central minimum shows that a symmetry lowering distortion (bond length alternation) is energetically costly. 165

A.23 At high density the two sets of LMOs have nearly identical bond order, as the ring molecule is dilated, the symmetry is broken and one set of LMOs retains 2-center character as demonstrated by BO ≈ 2 while the other set gradually decreases. 166

A.24 Coincident with breaking of bond order symmetry a non-central minimum develops in the potential energy scan, bond length alternation is favored below this density. 166

List of Tables

Chapter 1

Motivation and Brief Summary of the Thesis

Consider the two hypothetical linear arsenic molecules in Fig. 1.1: AsH_2-AsH-AsH_2 (top) and AsH_2-AsH_2-AsH_2 (bottom). The bonding between the arsenic atoms is mediated by four and three electrons, respectively. The four-electron bond happens to be stabilized in a symmetric configuration, whereby the two As-As bonds are equal in length. It is not a conventional bonding scheme in that the molecule is held together by a *three* center bond, not a pair of textbook two-center bonds. This three-center bond is an example of a multi-center bond. On the other hand, the three-electron bond in the AsH_2-AsH_2-AsH_2 molecule is not stable in the symmetric configuration but, instead breaks up and forms a loose complex between a covalently bonded dimer AsH_2-AsH_2 and an AsH_2 radical. This arrangement breaks the reflection symmetry of ground state for the four electron case. Already the simple

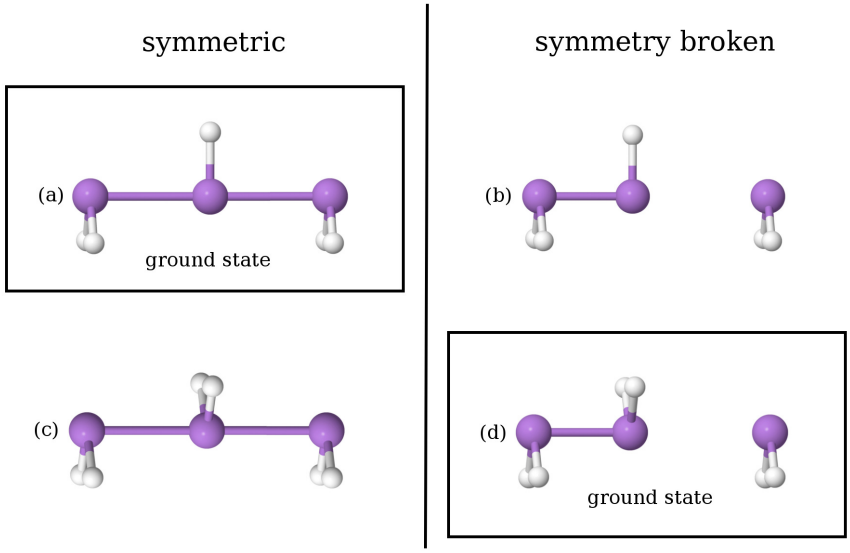

Figure 1.1: Two hypothetical linear molecules, AsH_2-AsH-As_2 shown in panels (a) and (b) and AsH_2-AsH_2-AsH_2 shown in panels (c) and (d), chosen to demonstrate symmetric and symmetry broken ground states.

example in Fig. 1.1 suggests that changes in the spatial symmetry of a molecule and corresponding bonding type are intrinsically related.

To bring home the notion of symmetry breaking we optimize the AsH_2-AsH_2-AsH_2 molecule in Figure 1.1 at a fixed overall length, for several values of the latter length. (Only one of those lengths corresponds with the actual ground state.) Panel (b) demonstrates that if the trimer is forced to be longer than a certain critical length, the middle arsenic cannot remain in the middle, but, instead, must choose the nearest neighbor, thus breaking the symmetry. Similarly, the three electron bonded molecule would become symmetric, if squeezed below a certain critical length. The symmetry breaking observed for sufficiently long molecules—or, equivalently, at sufficiently low densities— is not unlike the symmetry breaking that takes place in the Ising ferromagnet below the Curie point, shown in Figure 1.3. It is also instructive to

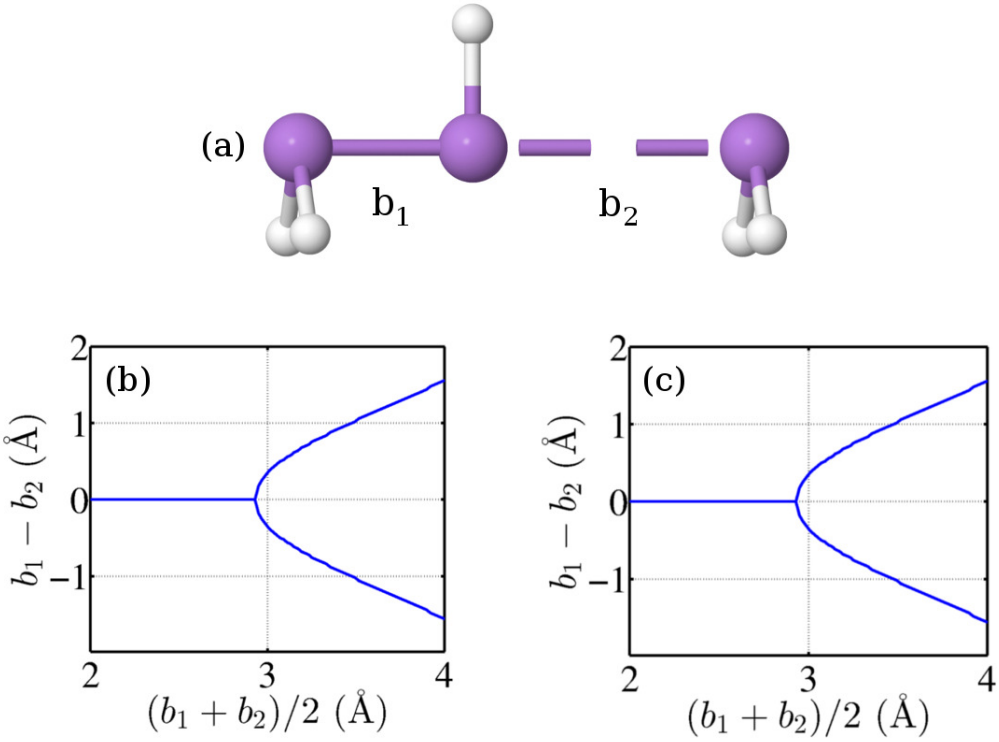

Figure 1.2: The 4-electron/3-center bonding configuration from the l.h.s. of Fig. 1.1. Two ways to plot the symmetry breaking behavior as the molecule is uniformly stretched, panel (b) shows the bond length difference, (c) shows individual bond lengths as a function of the overall trimer length

plot the longer bond length, b_2, as a function of the shorter bond length, b_1, see Figure 1.4(a).

The symmetry breaking pattern in the small, trimeric molecule above turns out to be surprisingly general: Landrum and Hoffmann [1] have cataloged the bond lengths in similar linear trimeric bond configurations using thousands of crystallographic files in the Cambridge Structural Database (CSD) [4]. Each point on their scatter plot, Fig. 1.4(b), corresponds to an individual compound. A linear segment can be seen near the horizontal axis. The corresponding, nearly symmetric configuration

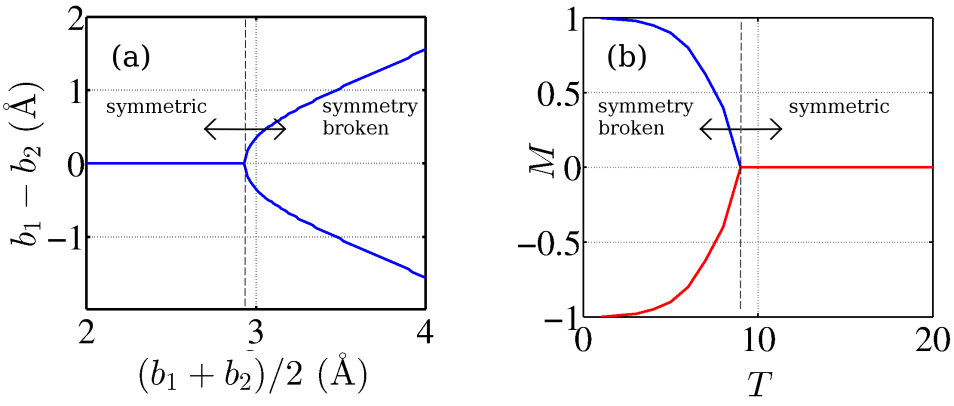

Figure 1.3: Bond length difference behavior from panel (b) of Figure 1.2 shown in panel (a) for comparison with notional magnetization behavior of the classical Ising model in panel (b), data shown is representative only, magnetization M and temperature T are dimensionless in this figure.

$b_1 \approx b_2$ is analogous to the symmetric ground state in Fig. 1.1(a). The other segment, $b_1 \neq b_2$, corresponds with the symmetry broken part of the configurational space. One can also see this by recasting the bond lengths b_1, b_2 taken from Landrum and Hoffmann's plot as functions of the overall size of the molecular fragment $b_1 + b_2$ in Fig. 1.5, to be compared with Fig. 1.2.

Perhaps the purest form of the symmetry breaking resulting in the emergence of the covalent bond in the *bulk* is realized in the transition from the high pressure, simple-cubic structure of elemental arsenic to the rhombohedral structure characteristic of normal conditions, see Fig. 1.6. The rhombohedral structure sets in as the system must choose between two equivalent, mutually complementary lattices shown in Fig. 1.7. The resulting, stripe-like pattern of bond strength and, hence, electronic density is often called a *charge-density wave* (CDW).

The ambiguity in the bonding within intermetallic compounds exhibits itself in

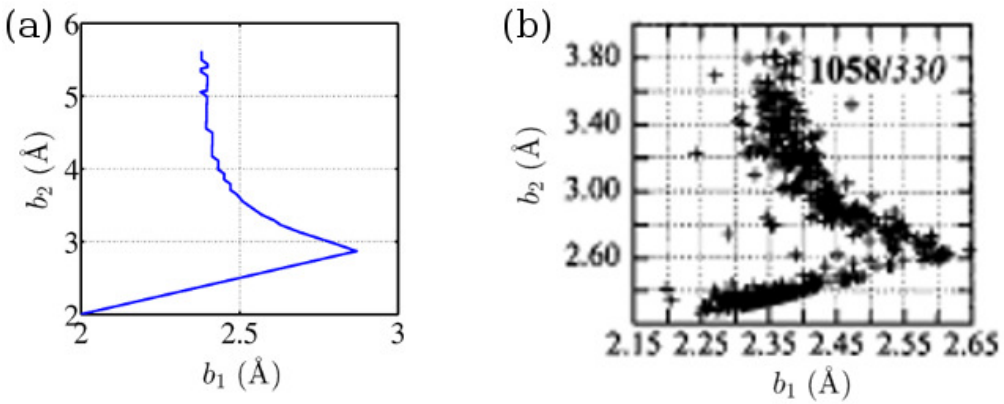

Figure 1.4: Individual bond length data from panel (c) of Figure 1.1 recast parametrically as $b_2(b_1)$ is shown in panel (a) for comparison with Cl-Sb-Cl trimeric motifs found in the search of solid-state compounds by Landrum and Hoffmann.

elemental arsenic as a result of pressure changes. A family of Pn_2Ch_3 compounds exhibits such ambiguity readily already at normal conditions. Here Pn (pnictogen) and Ch (chalcogen) stand for elements P, As, Sn, Bi of group 15 and elements S, Se, Te from group 16. Although made of elements with identical sets of valence electrons, the compounds from this family exhibit very diverse coordination patterns, as shown in Fig. 1.8. We observe that the chalcogen can have anywhere between two and six neighbors, the two extremes corresponding to the perfect Lewis octet and a hypervalent, multi-center bonding scheme.

The surprising variety of bonding in those chemically-similar compounds, on the one hand, and the accompanying symmetry changes, on the other hand, can be rationalized on a systematic basis. At the level of small, trimeric units, the symmetry breaking is shown to result from the interplay of cohesive interactions and the repulsion between the ionic cores, also subject to the variation in electronegativity. In 3D, bulk materials, the interplay becomes more complicated, however the main control

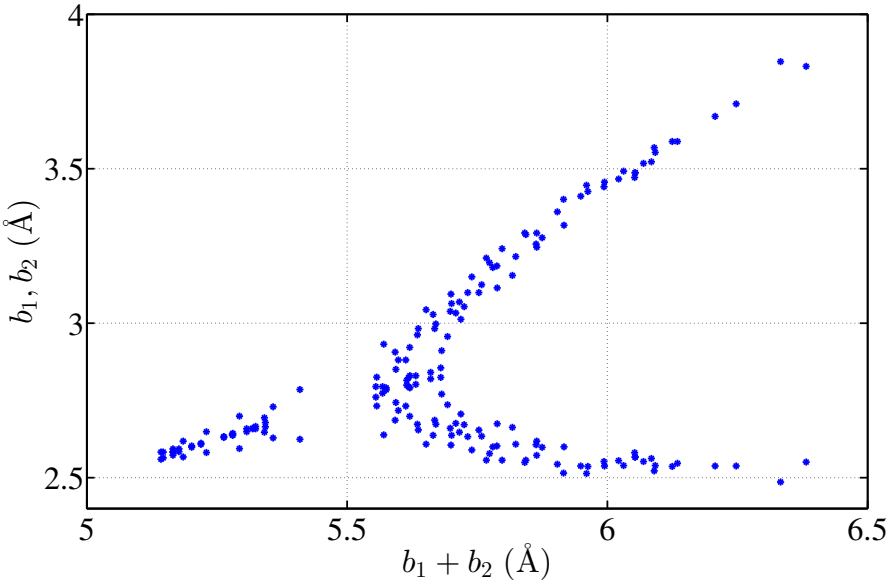

Figure 1.5: Alternative presentation of Landrum and Hoffman data for Br-Sb-Br trimeric motifs showing bond lengths as a function of overall trimer length to highlight evolution of covalent/secondary bonds from the multi-center interaction.

parameters, the density and electronegativity variation, are still the same. The main distinction between small molecules and bulk materials is the possibility of itinerant charge carriers in the latter. We arrive at a view in which the canonical chemical interactions are viewed as sectors on a phase diagram, see Fig. 1.9. The sector boundaries correspond with continuous or discontinuous transitions between phases of a compound. In addition to the multicenter and covalent/secondary interactions, the ionic bond emerges when the electronegativity exceeds a certain threshold value. Insofar as the metallic and ionic bond correspond with delocalized and localized electrons, we arrive at the conclusion that the coexistence between two charge-density waves characterized by sufficiently differing degrees of electron-localization is analogous to bringing together two substances that do not mix well, similarly to oil and

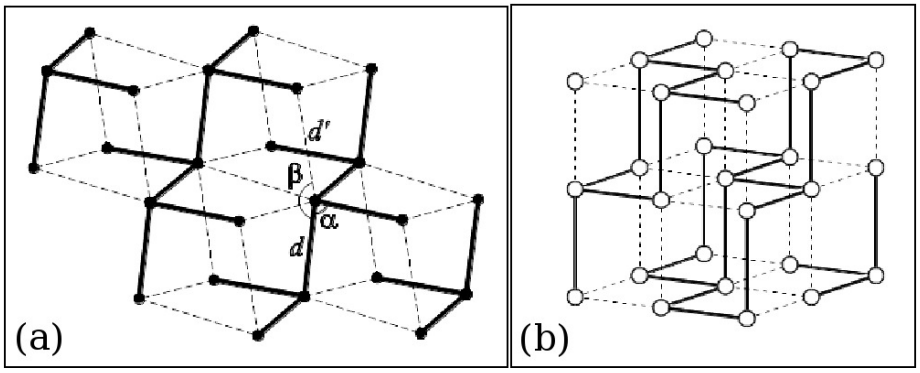

Figure 1.6: Application of the ZL symmetry breaking structural framework to rhombohedral arsenic. Covalent bonds corresponding to the thick bold lines on the rhombohedral lattice in panel (a) map to what we term "links" on the simple cubic parent structure in panel (b) shows.

water. These results are covered in Chapter 2.

According to the phase diagram in Fig. 1.9, the emergence of the covalent bond is accompanied by a spatial symmetry breaking in the nuclear arrangement, similarly to the trimeric example in Figs. 1.1-1.3. In contrast, the lowering of the translational symmetry during the metal-insulator transition is not accompanied by changes in the underlying lattice, but is essentially electronic. The nuclei simply set the overall density scale. This phenomenon is observed already at the trimer level. In such small molecules, electron localization can be quantified using a well-established localization procedure, in which one transitions to a new set of mutual orthogonal electronic orbitals that minimize electron-electron repulsion between the orbitals. These new orbitals can be interpreted as one's best guess for the electronic composition of the canonical two-center bonds. We will observe, in Chapter 3, that the stability (or metastability) of the molecule or a solid alike can be traced to whether the

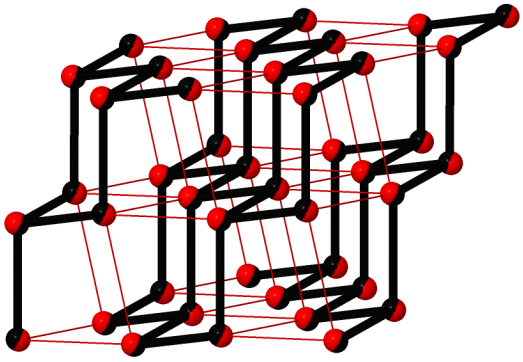

Figure 1.7: Mutually complementary bond order waves in black phosphorus, panel (a) and rhombohedral arsenic, panel (b). Electron density, concentrated in the interatomic regions identified by high bond order would form stripes.

inter-atomic spaces for nearest neighbors are all covered by the so constructed two-center bonds. Several, fascinating examples of breaking of point-symmetries will be demonstrated. Also in Chapter 3, we propose that the connection between the sufficient coverage of the inter-atomic spaces by the localized molecular orbitals can be used to design a high-throughput procedure for initial screening of candidate compounds for stability, without the need for the computationally-costly geometric optimization.

In Chapter 4, we make a systematic connection between the notion of coexistence of charged density waves with differing degrees of electron localization and the coexistence of distinct thermodynamic phases. Our formal tool is a Landau-Ginzburg density functional that builds, starting with a tight-binding Hamiltonian in the non-interacting limit. Rooted in the venerable density-functional theory, [5] the present approach allows one to added interactions in a straightforward way, using an expansion in terms of the strength of the charge density wave. The method self-consistently

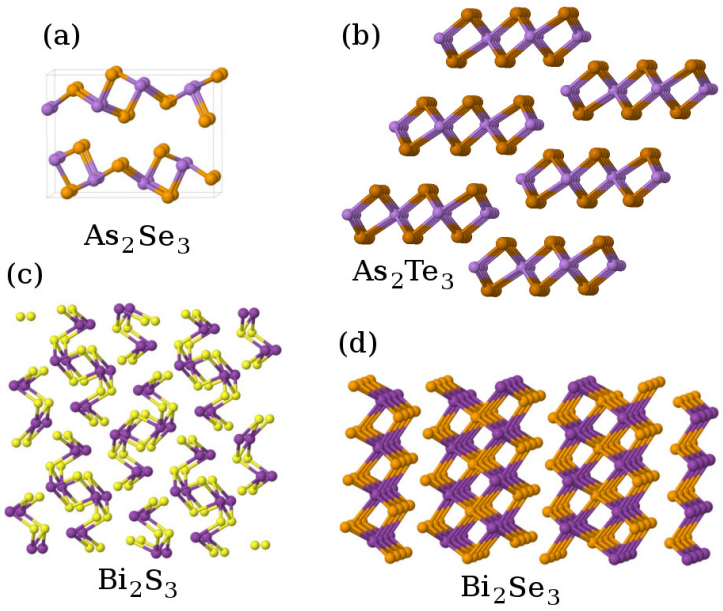

Figure 1.8: Four examples of crystal structures from the Pn_2Ch_3 group of compounds demonstrating the ambiguity in coordination present in these materials. As_2S_3 sample in panel (a) hosts a strong covalent bonds and weaker secondary bonds at each center. Both Bi and S are 3-coordinated in the stibnite structure shown in panel (c). The As atoms are 6-coordinated while Te has only 3 contacts as seen in the As_2Te_3 structure seen in panel (b). Every atom shown in the Bi_2Te_3 sample in panel (d) is octahedrally coordinated.

yields that the phase with more localized electrons is also less polarizable. This notion allows us to connect metal-insulator transition with the classic phenomenon of poor miscibility of substances with sufficiently distinct polarizabilities, such as oil and water. We confirm the findings from Chapter 2 that the metal-insulator transition could be either discontinuous or continuous, even in the presence of interactions. The possibility of such continuous transitions had been dismissed previously by Mott and others. [6] Furthermore, we establish that the transition's being discontinuous is likely caused not by the exciton condensation mechanism put forth by Mott, but is of

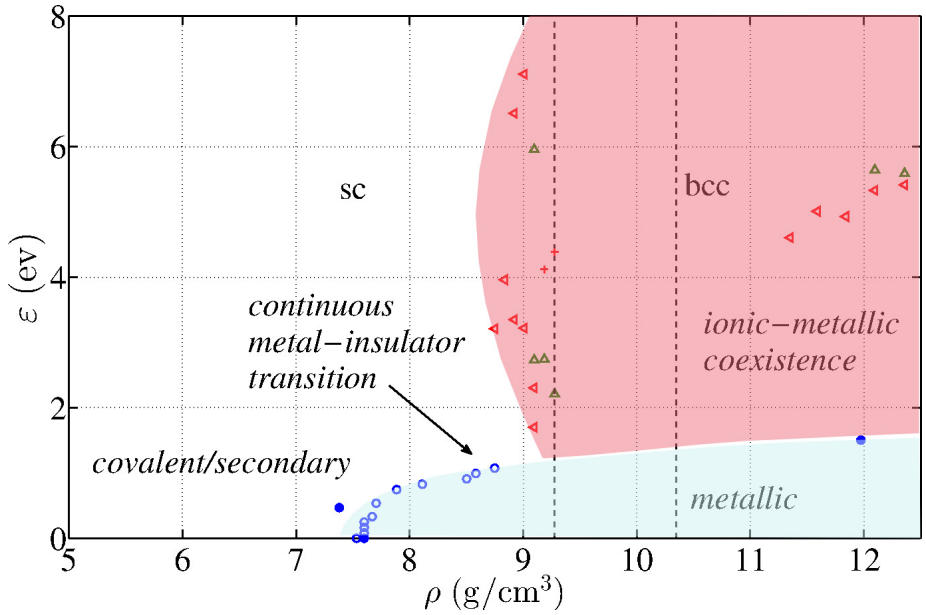

Figure 1.9: Phase diagram for relevant chemical interactions in a binary compound as a function of density and electronegativity. Label "sc" stands for simple cubic and "bcc" for body-centered cubic.

more general, symmetry-related nature. This symmetry-related mechanism operates during the classical liquid-to-solid transition. [7] The latter is always discontinuous.

Yet the possibility of a continuous symmetry-breaking transition in electronic systems is not the only distinction between the latter, quantum-mechanical systems and classical liquids. Perhaps more interesting is the finding that interfaces between distinct CDW states, if present, must host very special midgap electronic states. Zhugayevych and Lubchenko [8–10] have argued the midgap states account for the mysterious light-induced phenomena in amorphous chalcogenide alloys, such as midgap optical absorption and ESR signal, see Fig. 1.10. Amorphous chalcogenides are of significant technological importance, the most common application being re-writable optical drives. We have succeeded in generating bulk structures

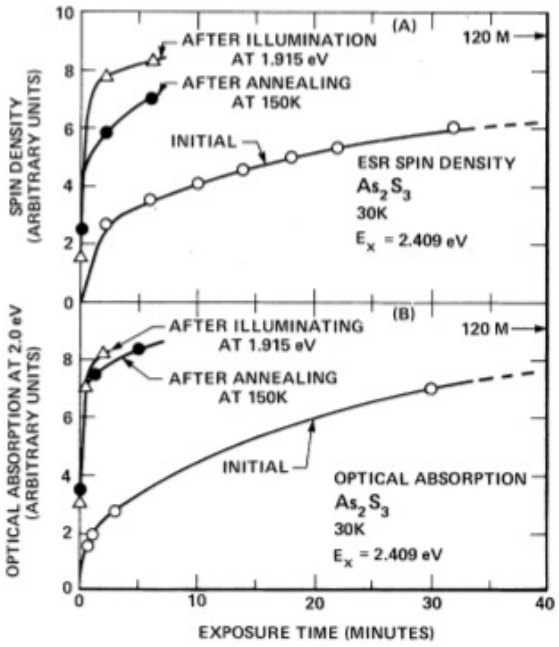

Figure 1.10: Manifestations of electronic midgap excitations in As_2S_3 as a result of illumination at bandgap frequency. Panel (a) shows density of unpaired spins growing with exposure time. Panel (b) shows appearance of sub-gap absorption following bandgap frequency illumination.

that host such midgap states, as in Fig. 5.11. The need for vacancies in the structure for compounds As_2Se_3 complicates the notion of a system of quasi-one dimensional motifs requisite for the midgap states. Despite this complication, we show the midgap states are robust. These results are covered in Chapter 5.

Chapter 2

The chemical bond as an emergent phenomenon

2.1 Overview

We argue that the covalent bond and various closed-shell interactions can be thought of as symmetry broken versions of one and the same interaction, viz., the multi-center bond. We use specially chosen molecular units to show that the symmetry breaking is controlled by density and electronegativity variation. Depending on the precise combination of these factors, the symmetry breaking transition can be either continuous or discontinuous. When present, the discontinuity is ordinarily weak so that the transition region is still approximately subject to a law of corresponding states. We further argue on the inherent relation of the covalent, closed-shell, and multi-center interactions with ionic and metallic bonding. These can be viewed as

distinct sectors on a phase diagram with density and electronegativity variation as control variables; the ionic and covalent/secondary sector are associated with on-site and bond-order charge density wave respectively, the metallic sector with an electron liquid. Thus the canonical types of the chemical bond are argued to be well defined. While displaying a contiguity at low densities, the metallic and ionic interactions are better viewed at high densities as distinct phases separated by a discontinuous transition. In this picture, multi-center interactions are viewed as a co-existence or hybrid of the metallic and ionic bond, the two engendered by delocalized and localized electrons respectively. Near sector boundaries and co-existence regions on the phase diagram of interactions, solids are expected to show a propensity for displacive transitions while allowing for effective, semi-empirical descriptions. One corollary of the present argument is that the conventional, two-center covalent bond can be viewed as a low-density relic of cohesive forces arising in the bulk-condensed state.

2.2 Motivation

Chemical bonding is traditionally discussed in terms of the covalent, ionic, and metallic bond [11], and weaker, closed-shell interactions such as secondary, donor-acceptor, hydrogen, and van der Waals [12, 13]. The distinction between these canonical bond types is not always clear-cut. For instance, a directional, multi-center [14] bond holding together identical atoms has an inherent ionic feature: In a three-center, linear $pp\sigma$ bond, [15, 16] the central atom contributes only a half orbital to each of the

individual $pp\sigma$ bonds. [17] The terminal atoms, on the other hand, each contribute one full orbital, implying a non-uniform charge distribution over the bond. At the same time, the three-center $pp\sigma$ bond can be thought of as a limiting case of the metallic bond, since the appropriate electron count for an infinite chain corresponds to a half-filled band [14]. This identification is consistent with the metallic luster of compounds in which covalent and secondary bonds are comparable in length [13]. In solid-state contexts, interplay between ionic and covalent interactions is often discussed using the van Arkel-Ketelaar triangle for binary compounds [18–21]; or revealed, for instance, in the taxonomies of classical valence compounds and Zintl phases [22, 23]. Contiguity between the metallic and ionic extremes is exemplified by metal-ammonia solutions [24], whose electric conductance ranges between largely electronic and ionic, depending on the concentration of the metal.

Despite their distinct phenomenologies, canonical types of bonding are not always easy to distinguish on formal grounds, the case of the metallic bond being particularly subtle. Indeed, cohesive interactions in periodic solids are usually discussed either in terms of molecular orbitals (MO) or in terms of plane-wave, Bloch electronic states. [25] The two approaches are not equivalent: The majority of *aperiodic* condensed phases, such as liquids, frozen glasses, or amorphous films, are expressly not Bloch solids. (Within the Born-Oppenheimer approximation, liquids are solids as far as the electrons are concerned.) Yet the Bloch and MO approaches are often perceived as equivalent. In fact, there have been calls to do away with the concept of the metallic bond altogether, by including it under the broader rubric of covalent interactions. [26] Electron delocalization in aperiodic solids is of much subtler nature

than in crystals [27, 28]; one no longer speaks of allowed energy bands but, instead of *mobility* bands. The latter are defined in a relatively narrow sense that individual molecular orbitals (MOs) extend further than the mean-free path of a charge carrier, a notion that harks back to the original motivation for introducing the metallic bond via the mobility of the electrons [11]. The most important feature of the metallic bond is that the electrons do indeed comprise a liquid; an arbitrarily weak field results in a particle flow. No such flow can take in insulators, where the electrons are fully localized.

In its ideal form—even if unachievable in actual compounds—the metallic bond is isotropic, not directional. This may directly reveal itself in the material's being close-packed and/or malleable. Metallic substances tend to be poor glass-formers and decrease in volume upon crystallization, as perfect hard spheres would. In contrast, bond directionality, as in water, silicon, or germanium, may even lead to expansion during freezing. From the MO viewpoint, metals are special in that they possess a bulk density of (formally non-bonding) states that can be easily occupied at arbitrarily low temperatures. In contrast, the canonical covalent bond is defined most unambiguously as being due to filled states. From a thermodynamics vantage point, metallic and covalent interactions can be thought of as distinct since the metallic and insulating phases are separated by a phase transition. [28] This viewpoint will prove most instructive in the present context, the pertinent order parameter having to do with the degree of localization of the electronic liquid.

The lack of clear dichotomies between canonically distinct chemical interactions is brought home by a systematic study by Landrum and Hoffmann [1], who have

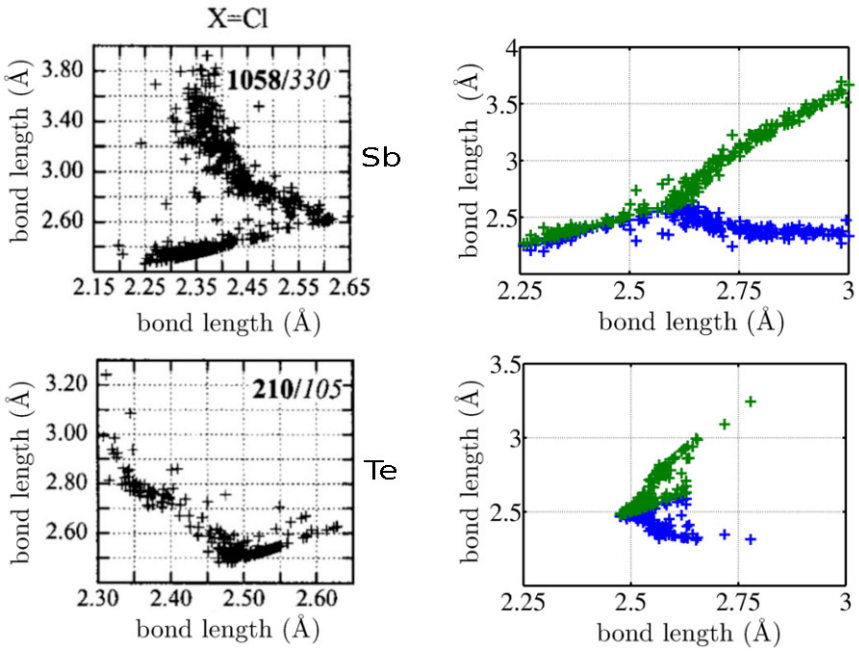

Figure 2.1: *Left*: The lengths of the two bonds in three-center bonding configurations compiled by Landrum and Hoffman [1]. *Left*: The Landrum-Hoffmann data replotted to show the two bond lengths as functions of the trimer length per bond.

screened thousands of compounds in the Oxford Structural Database for near linear trimeric motifs XQX, where Q stands for Sb or Te and X for F, Cl, Br, or I. Select parametric plots of the lengths b_1 and b_2 of the two individual bonds, from Ref. [1], are reproduced here on the l.h.s. of Fig. 2.1. The three-center bond is directional and exhibits back-bonding. [1] Indeed, the negative slopes of the $b_2 \neq b_1$ portions of the parametric curves on the l.h.s. of Fig. 2.1 imply that shortening of the weaker bond supplies electrons into the anti-bonding orbital of the stronger bond, resulting in weakening of the latter. The shorter bond in the $b_2 \neq b_1$ portions can be short enough to be considered covalent, while the longer, weaker bond varies in strength from what one expects for a relatively strong, directional secondary bond to a very weak van

der Waals interaction, which is essentially non-directional. In the symmetric region, $b_1 \approx b_2$, the bond strength can approach that of the covalent bond, for sufficiently small $b_{1,2}$. Thus the empirical data suggest that the covalent, secondary, and three-center bonds form a true *continuum* of interactions. Despite some scatter in the data, one notices a great deal of universality in the b_1 vs. b_2 relation. While the synergic relation between complementary covalent and secondary bonds is expected based on straightforward molecular orbital considerations [1], as just discussed, its apparent near universality is less obvious. This near universality suggests a *law of corresponding states* may apply.

Laws of corresponding states, such as the familiar van der Waals equation of state, [29] often arise on a systematic basis in the context of critical points. If rescaled in terms of the critical temperature, pressure, and density, equations of state for chemically distinct substances will look identical near the critical point so long as those substances belong in the same universality class, [30] as defined by the symmetry and range of the interaction; the detailed form of interaction becomes immaterial because the molecular lengthscale is much shorter than the correlation length. In those common situation when a critical point is a limiting case of a set of discontinuous transitions—as is the case for the liquid-to-vapor transition, for instance—laws of corresponding states are still expected to hold approximately, not too far from the critical point. When it holds, a law of corresponding states offers a systematic way to reduce the complexity of the problem by allowing one to use the simplest possible model from the universality class in question.

A revealing way to view the Landrum-Hoffmann data is to graph the two bond

lengths as functions of the overall trimer length per bond $(b_1+b_2)/2$, see the r.h.s. of Fig. 2.1. The graphs explicitly show an apparent *symmetry breaking* that takes place as the system expands from a high density state, in which $b_1 \approx b_2$, to a state where the central atom chooses to make a strong bond with a specific neighbor, while settling on a weaker interaction with the other neighbor. The antimony and tellurium cases are distinct in that the broken symmetry regime $b_2 \neq b_1$ can coexist with the symmetric regime $b_2 = b_1$ in the latter case, but not in the former. In the context of bulk phase transitions, a macroscopic phase coexistence implies the transition is discontinuous, common example being the liquid-to-solid transition. [29,31] Conversely, the lack of such coexistence implies the transition is continuous, a critical point. Incidentally, the density dependence of the bond lengths for the antimony compounds in Fig. 2.1 parallels that for the transition between the rhombohedral and simple-cubic arsenic. [32] Spatial coexistence of distinct types of bonding can be directly seen in the crystal of Bi_2Te_3, where multicenter, covalent, and secondary bonding patterns form extended layers, see Fig.2.2(a). This can be contrasted with As_2S_3, Fig. 2.2(b), a compound made of covalently bonded double layers that interact relatively weakly via secondary interactions; [9] each atom is surrounded by a perfect Lewis octet.

Here we argue that not only are the two-center covalent bond and secondary interaction intimately related to each other and, in turn, to the multi-center bond, but can be thought of as *originating* from the multi-center bond as a result of a density-driven symmetry-breaking transition. The transition could be either continuous or discontinuous. In the latter case, the discontinuity is weak and so a law of

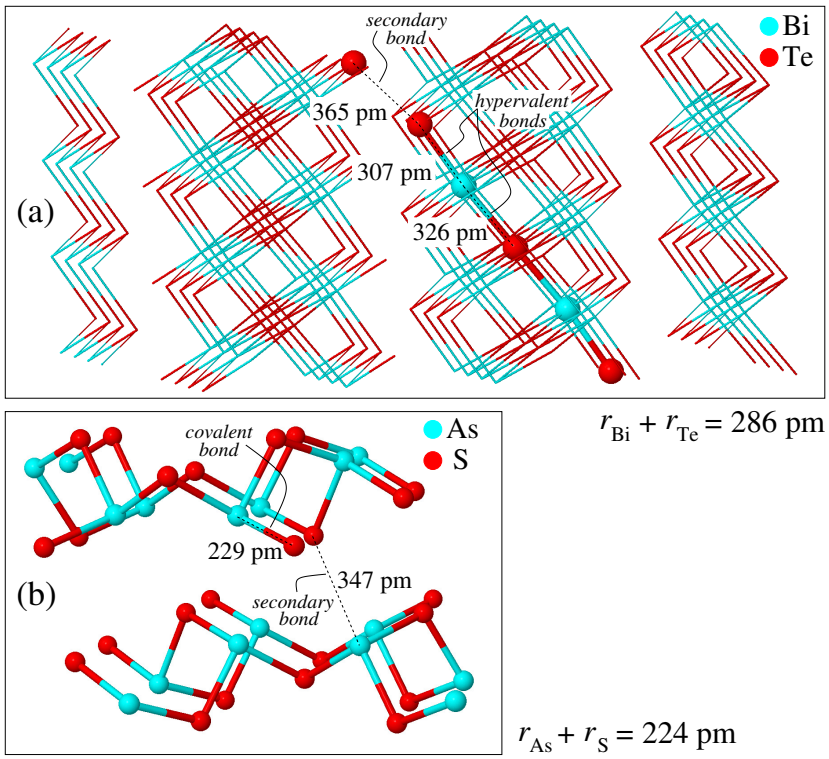

Figure 2.2: **(a)** Structure of Bi_2Te_3 illustrating coexistence of multicenter, covalent and secondary bonding. **(b)** Structure of As_2S_3 illustrating that the bonding is essentially covalent within the double layers. Sums of pertinent covalent radii are provided for the reader's reference.

corresponding states still holds approximately. We further argue that a similar relationship exists between the covalent-secondary set of interaction and the ionic bond, driven by density changes and/or electronegativity variation. We next extend these arguments within the solid state context, where we find that the ionic and metallic bond can be viewed as fully distinct phases on a "phase-diagram" of interactions in that they are separated by one or more discontinuous phase transitions, above a certain threshold density. The multi-center bonding is viewed as a coexistence, or hybrid, of the metallic and ionic bonding. The discontinuity of the transition stems

from poor mutual miscibility of localized and delocalized electrons. Below the aforementioned threshold density, the metallic and ionic bond form a continuous spectrum of interactions. The venerable density-functional theory [5] provides a formal foundation for and, at the same time, a convenient way to think about the phase diagram of chemical interactions: The covalent-secondary sector corresponds to the electrons forming a bond-order wave, while the ionic sector to an on-site charge density wave (CDW). [33] In the metallic sector, the itinerant electrons are subject to the field due to the ionic cores but could be thought of as not forming a CDW in the continuum limit.

In thinking of interactions as sectors on a phase diagram, we borrow the language from the renormalization group (RG) theory of phase transitions, [30, 34, 35] which operates on a space formed by coupling constants and, in general, by Hamiltonians. In the RG language, interactions and phases are interchangeable concepts. For instance, the paramagnetic and polarized states of a ferromagnet are viewed as (attractive) fixed points in a space formed by spin-spin couplings and the magnetic field. In the present framework, the role of the order parameter is played by the CDW type and the degree of electron localization; the description is coarse-grained, in full analogy with the RG framework.

The possibility of making a compound thus can be viewed as a question of coexistence of distinct types of charge density waves. For instance, while the Heusler compounds and half-Heusler compounds are readily synthesized, [36] intermediate stoichiometries are not. In fact, the full- and half-Heusler phases exhibit poor mutual

miscibility. [37] Yet those intermediate stoichiometries formally correspond to structures that interpolate between an insulating and metallic phase that are separated by a discontinuous transition and thus are automatically less stable than the two phases. One can likewise rationalize the variety of bonding preferences and structures in the semi-metallic region of the periodic table. For instance, the present notions provide a general understanding why the structures of di-pnictogen tri-chalcogenides, such as those depicted in Fig. 2.2, show bonding ranging from essentially covalent in lighter elements to multi-center, hypervalent [14] interactions for heavier species. In addition, the latter compounds are organized, structure-wise, into stripes and ribbons despite relatively uniform spatial distribution of the two constituent elements. Here we observe that the latter organization is analogous to lamellar ordering, which is common during phase coexistence. [24] Last but not least, the present results indicate that complications arising from those ambiguous bonding preferences are subject to universal relations in the form of laws of corresponding states. This justifies the use of semi-empirical, meanfield treatments exemplified by density-functional and tight-binding approximations, and even implicit-electron treatments such as the *classical* DFT, Landau-Ginzburg treatments of displacive transitions and multiferroic phenomena. [38, 39]

The present results thus demonstrate inherent relation and, at the same time, distinction between fundamental chemical forces. The article is organized as follows: In Section 3.4, we quantitatively analyse a substantial number of small molecular motifs to elucidate the mechanism of the symmetry breaking that leads to the emergence of the covalent and secondary bond from the multi-center bond, and its interplay with

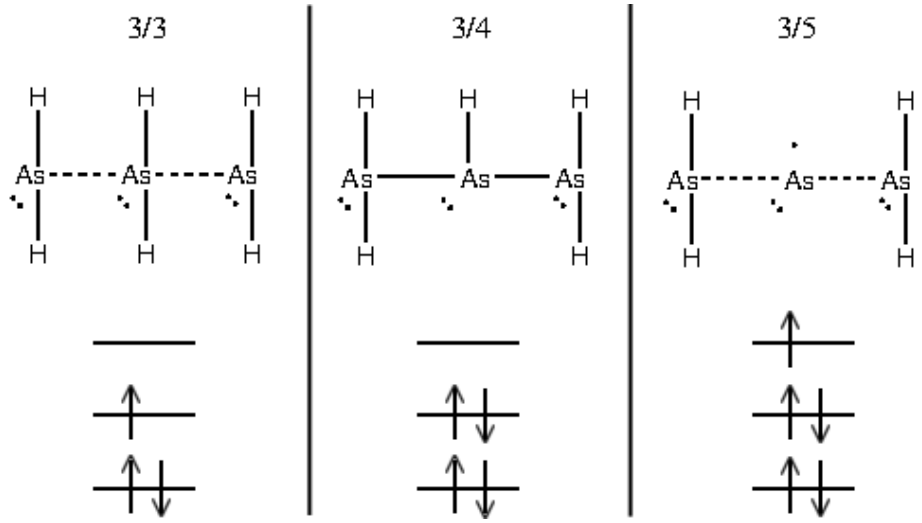

Figure 2.3: Lewis diagrams and the electronic configurations for the three-center $pp\sigma$ bond in the molecule AsH_2-AsH_n-AsH_2 trimer, $n = 0, 1, 2$. The dashed lines for $n = 0$ and $n = 2$ reflect the relative weakness of the $pp\sigma$ bond compared with the four electron configuration, which also happens to obey the Lewis octet rule.

the ionic interaction. In Section 2.4, we extend these arguments to the solid state context and build a phase diagram of interactions. We summarize and discuss the present results in Section 2.5.

2.3 Interplay of covalent, secondary, multi-center, and ionic interactions: Small molecules

To investigate spatial symmetry breaking in small molecules, we analyse a number of $pp\sigma$ bonded trimeric units suitably passivated by hydrogens to achieve a desired number electrons in the $pp\sigma$ bond. The Lewis dot structures and molecular orbital bonding schemes for a three-center $pp\sigma$ bond are shown in Fig. 2.3.

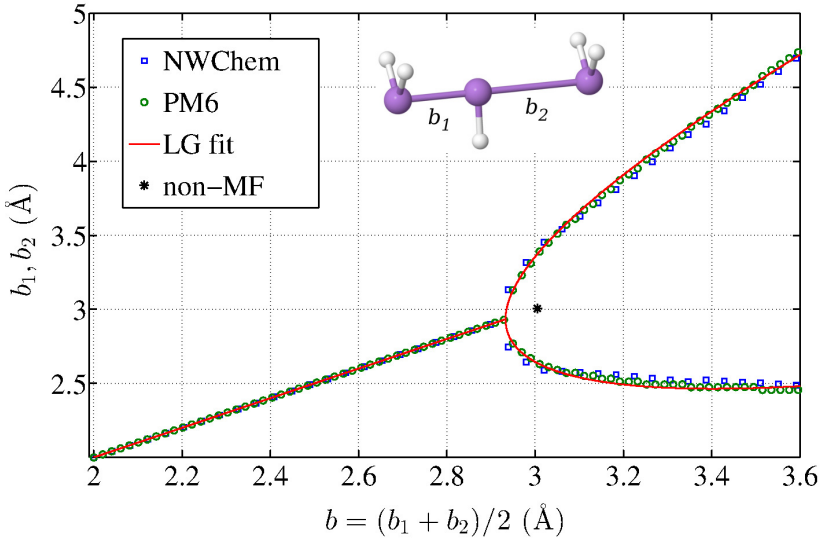

Figure 2.4: The equilibrium As-As bond bond lengths for the 3/4 case as functions of the overall trimer length, per bond, c.f. right top panel of Fig. 2.1. The energies are calculated using MOPAC and NWChem, see text. The arsenic atoms are constrained to lie on a straight line, while the As-H bonds lie in planes perpendicular to that line. The As-H bonds are fixed at length 1.5 Å ; mutual angle 90° for the terminal bonds, see the inset. The molecule has two reflection planes.

We begin from the AsH_2-AsH_n-AsH_2 trimer, $n = 0, 1, 2$. According to the Lewis diagram in Fig. 2.3, this formally corresponds to a three-center bond that contains 5, 4, and 3 electrons, respectively, assuming each arsenic carries a lone pair. Our main focus is on the $n = 1$ case, AsH_2-AsH_1-AsH_2, which corresponds to the classic 3-center/4-electron bond and, at the same time, obeys the Lewis octet rule. Consistent with this notion, it is the only molecule of the three that happens to be stable; the 3 and 5-electron molecules dissociate into a (passivated) dimer and monomer. The two As-As bond lengths, b_1 and b_2 respectively, are equal in the ground state of the 3/4 molecule. If stretched beyond a certain critical length, the molecule will dissociate and thus break the $b_1 = b_2$ symmetry. This is shown in Fig. 3.4, where

we plot b_1 and b_2 as functions of the overall trimer length per bond, $b \equiv (b_1 + b_2)/2$, which is externally imposed. The actual potential energy surface of the molecule, as a function of the As-As bond lengths b_1 and b_2, is provided in the Appendix.

One set of curves in Fig. 3.4 corresponds to the semi-empirical approximation implemented in the package MOPAC with PM6 parametrization. [40] MOPAC treats explicitly only the valence electrons, while using only a single, Slater-type basis function per atomic orbital and neglecting overlap between wave-functions on different centers during the self-consistent solution of the Hartree-Fock (HF) problem. (The corresponding matrix elements of the Hamiltonian are non-zero, of course.) The other set of curves is produced by the more accurate, ab initio approximation as implemented in the package NWChem [41] using the aug-cc-pVTZ-pp basis and a small, ten-electron effective core potential (ECP). MOPAC-optimized geometry compares well the more accurate method, despite the relatively crude level of approximation. There are several motivations behind our use of MOPAC, to be discussed in due time.

The symmetry breaking transition in Fig. 3.4, c.f. Fig. 2.1, is continuous and apparently similar to classic examples of symmetry breaking such as the Curie point or the critical point in liquids. The transition can be formally described using the Landau-Ginzburg expansion of the free energy [30] as a function of an order parameter characterizing the extent of symmetry breaking. In the present context, a convenient order parameter is the displacement $\Delta b \equiv (b_1 - b_2)/2$ of the central arsenic off the midpoint between the terminal arsenics. The corresponding Landau-Ginzburg

expansion then reads:

$$F(\Delta b) = \frac{a_2}{2}(b_c - b)\,(\Delta b)^2 + \frac{a_4}{4}(\Delta b)^4, \tag{2.1}$$

where b_c stands for the critical value of the trimer length b per bond. The equilibrium value of the order parameter is determined by optimizing the free energy (2.1). The quantities a_1 and a_2 are system-dependent parameters. In the symmetry broken region, the displacement of the middle arsenic is thus given by a simple formula:

$$\Delta\tilde{b} = \pm(\tilde{b} - 1)^{1/2}, \tag{2.2}$$

where we have rescaled the control parameter by its critical value: $\tilde{b} \equiv b/b_c$, and the order parameter by an appropriate combination of the critical length b_c and the expansion coefficients a_i: $\Delta\tilde{b} \equiv \Delta b/[a_2 b_c/a_4]^{1/2}$. Eq. (2.2) is, of course, a system-independent, universal relation and thus constitutes a law of corresponding states. When non-meanfield effects are important, the exponent in the r.h.s of Eq. (2.2) may differ from 1/2, however depends only on the universality class of the system. The best fit of the functional form (2.2) to the b_1 vs. b_2 dependences in Fig. 3.4 is shown as the solid red line, in the same figure.

The apparently excellent fit of the bond lengths b_1 and b_2 to the meanfield expression (2.2) does not mean that fluctuations are not unimportant. The location of the bifurcation point in Fig. 3.4 is only a lower bound on the value of the critical length at which the actual symmetry breaking would occur. This is because already zero-point, let alone finite-temperature vibrations within either of the two individual minima on the symmetry-broken energy surface will allow the system to

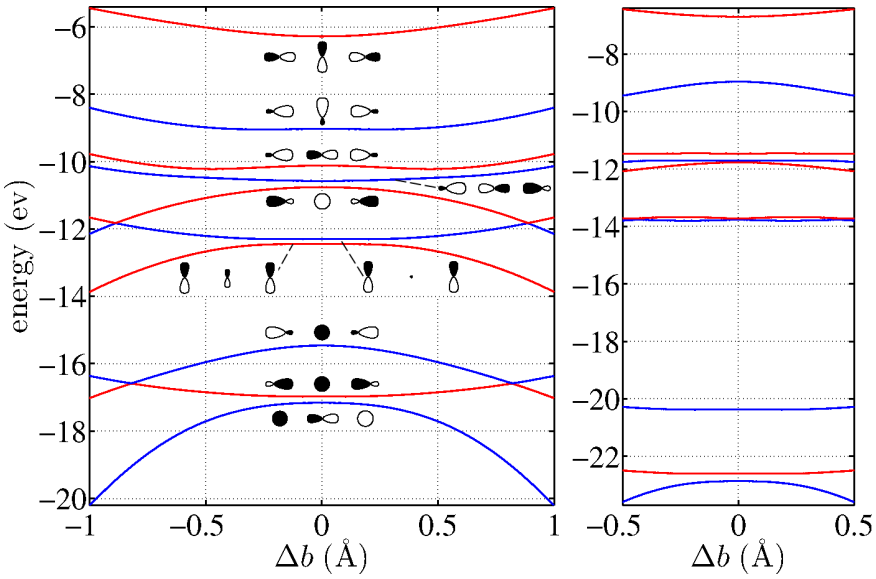

Figure 2.5: Walsh diagrams showing individual MO energies as functions of the displacement Δb of the central arsenic for the 3/4 trimer As_3H_5. The distance $b_1 + b_2$ between the terminal arsenics is 5.98 Å, which is just below the meanfield symmetry breaking point. The left and right panels show MOPAC PM6 data NWChem, respectively; note the difference in the horizontal ranges.

cross the barrier separating the minima, if the latter barrier is sufficiently low. Accordingly, one may assess the fluctuation-induced lowering of the critical point [30] semi-quantitatively, by requiring that those zero-point vibrations do not exceed the half-width of the barrier, see the graphical illustration in the Appendix. The so estimated location of the critical point is shown by the asterisk in Fig. 3.4; it differs meaningfully from its meanfield value.

In the aforementioned examples of the Curie point and continuous vapor-to-liquid transition, the symmetric state is favored by entropic forces, while cohesive interactions favor the symmetry broken state. [7] At the critical point, the two forces mutually compensate each other so that fluctuations of the order parameter incur

zero cost. Likewise, we inquire what competing factors could drive the transition in Fig. 3.4. Symmetry-lowering transitions in small molecules are often associated with Jahn-Teller instabilities. [25,42,43] (The JT instability would have to be second order or higher in this case, because of symmetry.) In contrast, we observe in Fig. 2.5 that the HOMO is actually *stabilized* in the symmetric configuration. At the same time, the molecular terms behave all but generically near the symmetry breaking point. Fig. 2.5 displays the terms for a broad range of the displacement of the central arsenic as calculated using MOPAC PM6 and NWChem; the two calculations produce qualitatively similar results.

In search for alternative explanation, we note that, by construction, MOPAC presents the full energy of the molecule as a sum of a cohesive and repulsive part: The former is obtained by solving the HF problem using the valence electrons, as already mentioned. The latter is parametrized to model the repulsion between the ionic cores. (We have checked that not much promotion of $3d$ electrons takes place at the densities in question, see Appendix.) In Fig. 2.6, we plot the cohesive and repulsive contributions, along with the total energy, in the symmetric and symmetry-broken regime. The cohesive part is increasingly stabilized for larger Δb. This is expected since the energy of the shorter bond depends sensitively on the bond length while the cohesive energy of the longer bond depends on the displacement already relatively weakly. The repulsive part is convex down and is minimized at the origin. At sufficiently high densities, the curvature of the repulsive term exceeds that of the cohesive part, thus stabilizing the symmetric, $b_1 = b_2$ state. The opposite take place in a sufficiently long trimer, thus leading to a bistable potential corresponding to the

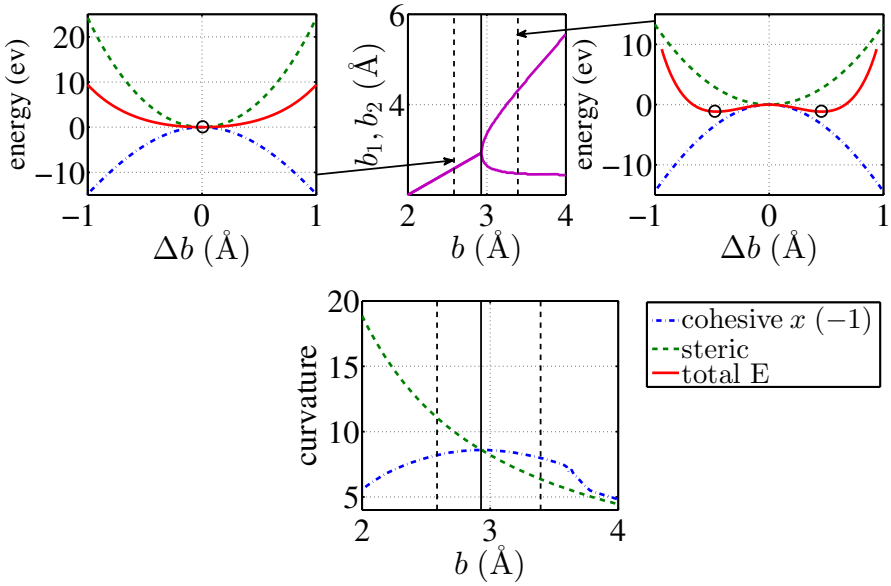

Figure 2.6: **(a)** The dependence of the cohesive and repulsive parts of the MOPAC-inferred energy of the 3/4 trimer As_3H_5 on the location of the middle arsenic, with the green and blue dashed lines respectively, in the symmetric state indicated in panel **(b)**. The solid red line shows the total energy; the circle indicate the location of the stable minima. **(c)** Same as (a), but in a symmetry broken configuration. There are two equivalent minima now. Panel **(d)** displays the dependence of the absolute values of the curvatures of the repulsive and cohesive parts at $\Delta b = 0$, on the trimer length.

emergence of two equivalent symmetry broken states.

We next plot in Fig. 2.7 the contributions of the MOPAC terms that, respectively, stabilize and destabilize the symmetric state, the total cohesive energy, and the very lowest term from Fig. 2.5. The latter term clearly contributes most to the destabilization. We note that of the four terms favoring symmetry breaking, three terms, including the bottom one, stem from *sp*-mixing. Conversely, only one of the *sp*-mixed orbitals stabilizes the symmetric state. This suggests the symmetry breaking is driven to a large extent by *sp*-mixing, consistent with solid state precedents. [44]

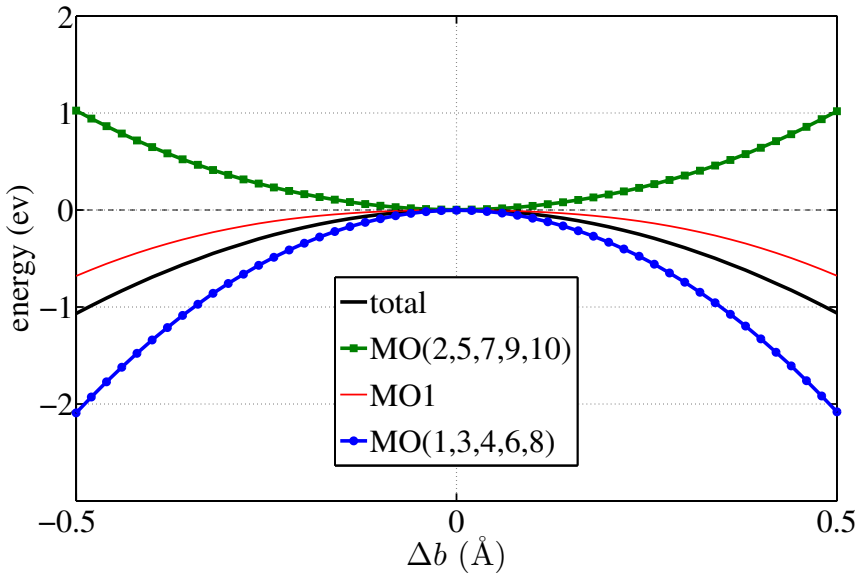

Figure 2.7: The solid black line shows the dependence of the MOPAC-inferred cohesive energy as a function of the location of the middle arsenic for the 3/4 trimer As_3H_5. The sum of the MOPAC terms from Fig. 2.5 that stabilize and destabilize the symmetric state shown in green and blue respectively. The individual contribution of the lowest term is shown in red.

The latter observation may seem in conflict with the expectation that the amount of *sp*-mixing should decrease with inter-atomic separation. This expectation is directly confirmed by the data in Figs. 2.8 and 2.9, where we show the contribution of the s and p atomic orbitals to the bond. We determine the latter contribution by a standard localization procedure, [45–48] which is discussed in great detail in the accompanying article. [49] We observe that upon dilation of the 4-electron trimer, *sp*-mixing largely peters out by the moment the spatial symmetry is broken. This process is even more dramatic for the electron-poor trimer $(AsH_2)_3$, for which the bonding orbitals undergo a symmetry-breaking transition even as the trimer is still spatially symmetric. This, inherently electronic transition has to do with a transfer

of electrons from the $pp\sigma$-bond to the lone pair on the central arsenic. We discuss this topic in great detail elsewhere. [49]

How does one reconcile the significance of *sp*-mixing for symmetry breaking, as apparent from Figs. 2.5 and 2.7, with its decrease at low densities, where the actual symmetry breaking occurs, see Fig. 2.8. To resolve this apparent contradiction we note that although the destabilization of the symmetric state due to *sp*-mixing does decrease with interatomic separation for sufficiently long trimers, the stabilization due to steric repulsion diminishes even faster, see Fig. 2.6(d). This emphasizes a relatively subtle feature of density-driven symmetry breaking: The cohesive and steric interactions both evolve similarly with density, at least as sufficiently low values of the latter. As the inter-nuclear distance decreases, electrons move toward the inter-atomic space because of the cumulative effects of Coulomb attraction to the involved nuclei; this stabilizes the cohesive component. At the same time, the steric repulsion *also* increases with density. The resulting bond enthalpy is therefore a modestly-sized quantity resulting from a delicate balance between two opposing, large quantities. We will observe a similar, but richer pattern in Section 2.4, in the context of density-driven coordination changes in solids.

We next investigate whether our model trimeric units exhibit a universality of the type in Fig. 2.1, using the atom size as the control variable. Fig. 2.10 shows the "bifurcation" plots for three elements from group 15—As, Sb, and Bi—rescaled so as to match the positions of the critical points. In the inset, we show the ratio of the rescaling factor for individual substances to the corresponding ionic and covalent radii; the latter represent traditional ways to evaluate the effective atom size as

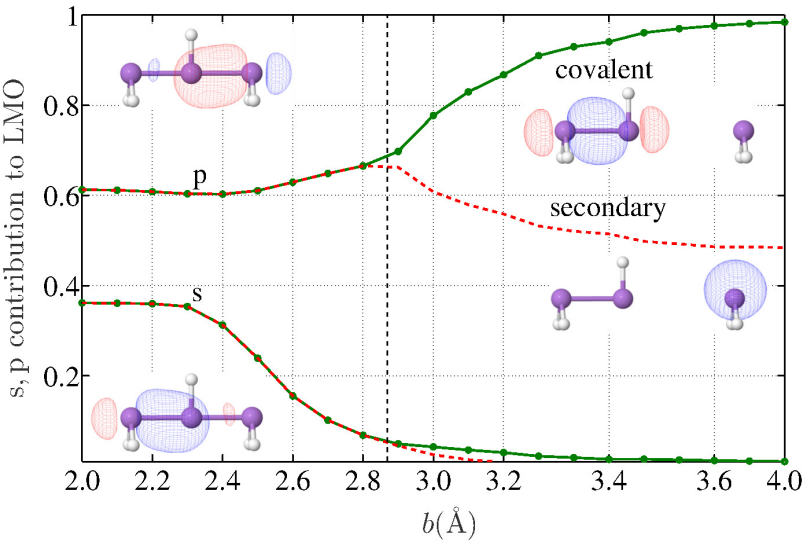

Figure 2.8: The s and p content of the localized molecular orbitals (LMOs), as functions of the trimer length per bond for the 3/4 trimer As_3H_5. The LMOs on the opposite sides of the symmetry breaking are exemplified in the insets.

pertinent for bonding. We observe a fair deal of universality. Still, the critical length of the trimer, which is the characteristic length scale in the problem, is not strictly tied to common measures of the atomic size. In a systematic trend, the departure increases with the atomic mass. These conclusions are consistent with above findings on the *sp*-mixing driving the symmetry breaking and the general notion that the amount of *sp*-mixing tends to decrease as one goes down the group in the periodic table. [14] In addition, the current trend is consonant with Clementi and Raimondi's observation [50] that the separation between the maximum charge density radius of the outermost d shell and valence s and p orbitals anti-correlates with the atomic number. In the present context, this implies that the effective size of the ionic core is greater for heavier atoms, relative to the extent of the frontier atomic orbitals. The resulting enhancement in steric repulsion thus serves to stabilize the symmetric

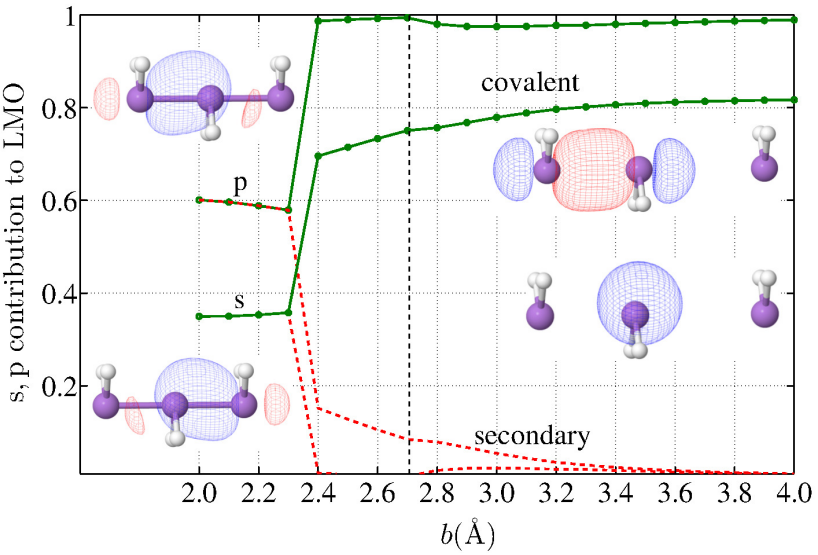

Figure 2.9: Same as Fig. 2.8, but for the 3/3 trimer As_3H_6. The vertical dashed line indicates the length at which the spatial symmetry is broken. Note that localized molecular orbitals exhibit a symmetry breaking while the molecule is still symmetric.

configuration.

Similarly to the preceding discussion, we next study the effects of varying the electron content of the three center bond on the symmetry breaking. This can be accomplished by modifying the number of passivating hydrogens on the AsH_2-AsH_n-AsH_2 trimer, as mentioned in the beginning of the Section. As in Fig. 2.10, the bifurcation graphs follow a universal shape, see Appendix. The critical lengths depend on the population of the $pp\sigma$ bond: $b_c = 2.71$, 2.87, and 2.63 for three, four, and five electron bond, respectively. This is consistent with the view of the middle orbital of the $pp\sigma$ bond, Fig. 2.3 as mildly bonding. [14] We reiterate that the four-electron case satisfies the Lewis octet rule in the symmetric state. This is supported by the bond-population analysis provided in the Appendix. To avoid confusion we note that the electron count cannot be generally regarded as an independent

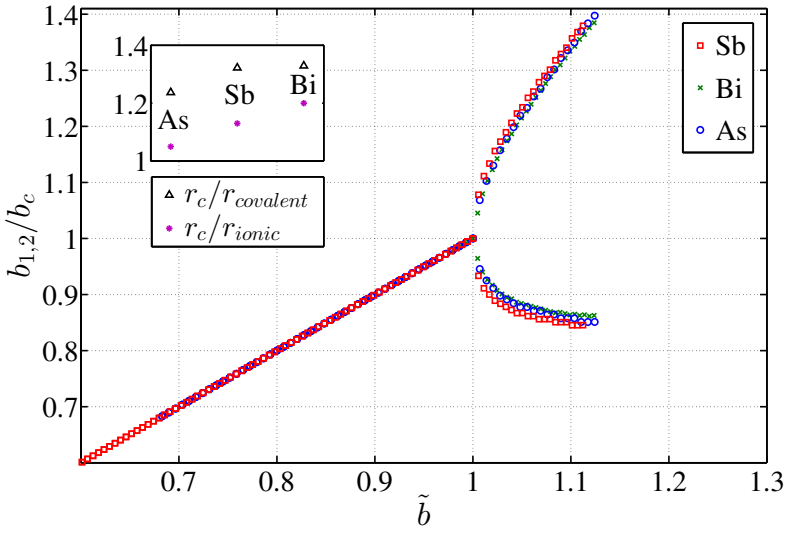

Figure 2.10: The dependences of the bond lengths $b_{1,2}$ for 3/4 trimers XH_2-XH-XH_2 (X = As, Sb, Bi), normalized by the respective critical length b_c, shown as a function of the reduced "per-bond" trimer length $\tilde{b} = (b_1 + b_2)/2b_c$. The inset displays the ratio of the critical length in terms of the corresponding covalent and ionic radii for each element.

control parameter but is determined self-consistently at given values of density and electronegativity variation, as is already clear from Fig. 2.9.

In discussing effects of electronegativity variation, we first recall that ionicity tends to suppress dimerization in extended one-dimensional systems. [51, 52] A similar effect can be seen at the extended Hückel level for a hypothetical linear H_3^- molecule, Chapter 6.4 of Ref. [25]. We have checked that modifying the electronegativity variation along the trimer does not significantly affect the universality of the symmetry breaking, see Fig. 2.11 and Appendix. There, we also demonstrate that the leading effect of introducing additional electronegativity is to shorten the bonds, consistent with the notion that the ionic radius is shorter than the covalent radius. As a result, the critical length for a mixed trimer X-Y-X or Y-X-Y is usually less

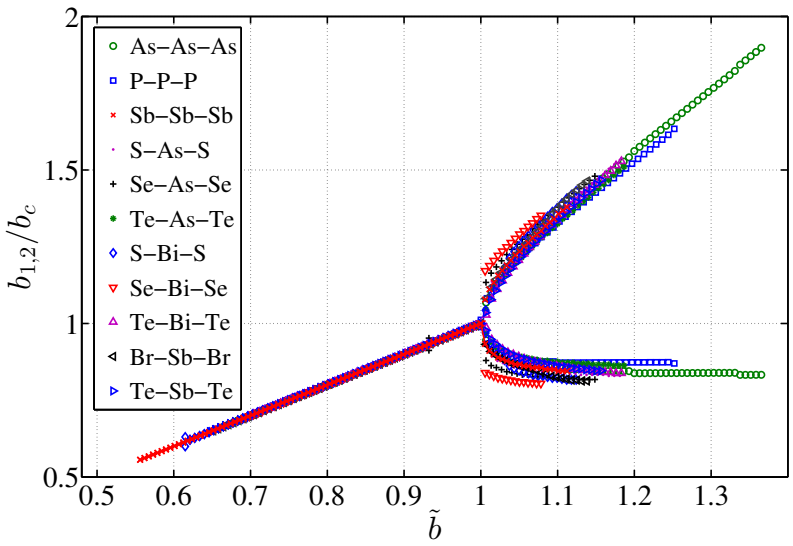

Figure 2.11: A number of bifurcation diagrams for pnictogen and chalcogen containin 3/4 trimers shown in reduced coordinates, as in Fig. 2.10. To maintain the 4 electron count, a chalcogen is passivated with one fewer hydrogen than a pnictogen.

than the average of the critical lengths for the homoatomic trimers X_3 and Y_3. The effect is modestly stronger when the more electronegative element is placed at the terminal positions, consistent with the earlier notion that the three-center bond is already partially ionic because the terminal atoms contribute more electronic density than the central atom to the individual two-center bonds.

The compilation of symmetry breakings for an extensive set of trimers, in Fig. 2.11, juxtaposes effects of varying the atom size, electronegativity, and valence. We again observe that every time continuous symmetry breaking takes place, a law of corresponding states holds already when one rescales all lengtscales by the critical length. If one were to rescale the bond-length difference $(b_1 - b_2)$, the universality would be even more pronounced. The rather extensive compilation in Fig. 2.11 shows that

some of the trimers actually exhibit a *discontinuous* symmetry breaking, c.f. the bottom of Fig. 2.1. In contrast with Fig. 2.1, the density range in which the symmetric and asymmetric molecule coexist is very narrow. Most likely such a discontinuity in a small molecule would be washed away by fluctuations, similarly to how the lowering of the critical point in Fig. 3.4. However in the solid state, the discontinuity may end up being stabilized by the crystal field.

2.4 Hierarchy of chemical interactions: The solid state

We now extend the above ideas to bulk systems. Arguably the simplest example of such a bulk system is a one-dimensional chain of equivalent orbitals, at half-filling. Already at the Hückel level, this model exhibits a rich behavior, if the bonds are allowed to deform, subject to a restoring force from the lattice. Using the creation (annihilation) operator $c^{\dagger}_{n,s}$ ($c_{n,s}$) for an electron on site n with spin s, the energy function can be written as:

$$\mathcal{H} = \sum_{n} \sum_{s=\pm 1/2} \Big[t(x_n, x_{n+1}) \left(c^{\dagger}_{n,s} c_{n+1,s} + c^{\dagger}_{n+1,s} c_{n,s} \right) + (-1)^n \epsilon \, c^{\dagger}_{n,s} c_{n,s} \Big] + \mathcal{H}_{\text{lattice}(\{x_n\})}, \tag{2.3}$$

where $t(x_n, x_{n+1})$ is the hopping matrix element between sites n and $n+1$, $(-1)^n \epsilon$ on-site energy, and $\mathcal{H}_{\text{lattice}}$ accounts for the elastic response of the lattice and the kinetic energy of the nuclei. In the lowest order expansion in bond deformation, $t(x_n, x_{n+1}) = t^{(0)} - \alpha(x_{n+1} - x_n - a)$, $\mathcal{H}_{\text{lattice}=\sum_n k(x_{n+1}-x_n-a)^2/2 + M\dot{x_n}^2/2}$. In the absence

of electronegativity variation, $\epsilon = 0$, Eq. (2.3) gives the venerable Su-Schrieffer-Heeger Hamiltonian for trans-polyacetylene. [53] A non-zero $\epsilon \neq 0$ was introduced by Rice and Mele to study heteropolar polymers. [51, 52]

At half-filling and in the absence of electronegativity variation, $\epsilon = 0$, the system (2.3) held at uniform spacing between nearest sites is a metal. It is, however, Peierls-unstable with respect to dimerization, [25, 53, 54] $x_{n+1} - x_n = \pm(-1)^n \text{const}$, upon which it becomes an insulator. The gap is approximately proportional to the differential $\Delta t \equiv |t(x_n, x_{n+1}) - t(x_n, x_{n-1})|$ in the hopping matrix element between the stronger and weaker bond; the gap is caused by scattering of the electrons near the wavelength corresponding to the unit cell of the distorted lattice, which now contains two atoms. In contrast, when the electronegativity variance is sufficiently large, the dimerization is suppressed while the material can be thought of as an ionic insulator; the gap is largely due to the work needed to transfer an electron from the more electronegative atom to its less electronegative counterpart, as is the case in sodium chloride for instance. As a rule of thumb, the transition from the Peierls-insulating to the ionic-insulating state will take place when the electronegativity variation is comparable to Δt the system would exhibit when $\epsilon = 0$. [51, 52] For a chain of passivated arsenics, this is numerically close to 1-2 eV. Whether the chain from Eq. (2.3) becomes a Peierls or ionic insulator, it develops a charge density wave (CDW). [33] The presence of dimerization implies that the CDW has an off-site component, while non-vanishing electronegativity variation implies the CDW has an on-site component.

The propensity of systems exhibiting substantial electronegativity variation to

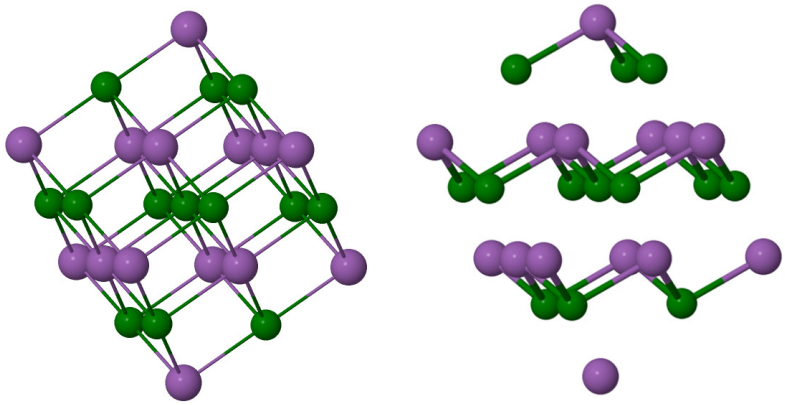

Figure 2.12: The structure of rhombohedral arsenic at normal conditions can be thought of as two face-centered cubic lattices, shown in purple and green, shifted relative to each other along the [111] direction. At sufficiently high pressures, the magnitude of the shift vanishes corresponding to a transition from the rhombohedral to simple-cubic lattice.

be insulators is not specific to a particular coordination pattern and is generic to any number of spatial dimensions; it is characteristic of many oxides and halides, for instance. In contrast, the Peierls instability is specific to one-dimensional systems, except in some idealized situations, such as when *sp* mixing and $pp\pi$ interactions can be neglected, [55–57] see also Refs. [9, 44, 58] Here we take a phenomenological approach and simply use that rhombohedral arsenic becomes simple-cubic given sufficient pressure, [32,59] see Fig. 2.12. Alongside, the material undergoes an insulator-to-metal transition. Thus we sketch, *by hand*, the first phase boundary on our phase diagram of chemical interactions, the control parameters being the mass density and electronegativity variation 2ϵ, see Fig. 2.13. The l.h.s. end of the boundary is fixed for concreteness at 2 eV, a generic value for a semiconducting gap. On the low density, ϵ side, the structure is characterized by a co-existence of (two-center) covalent and secondary bonding, as in the structure of rhombohedral arsenic, Fig. 2.12.

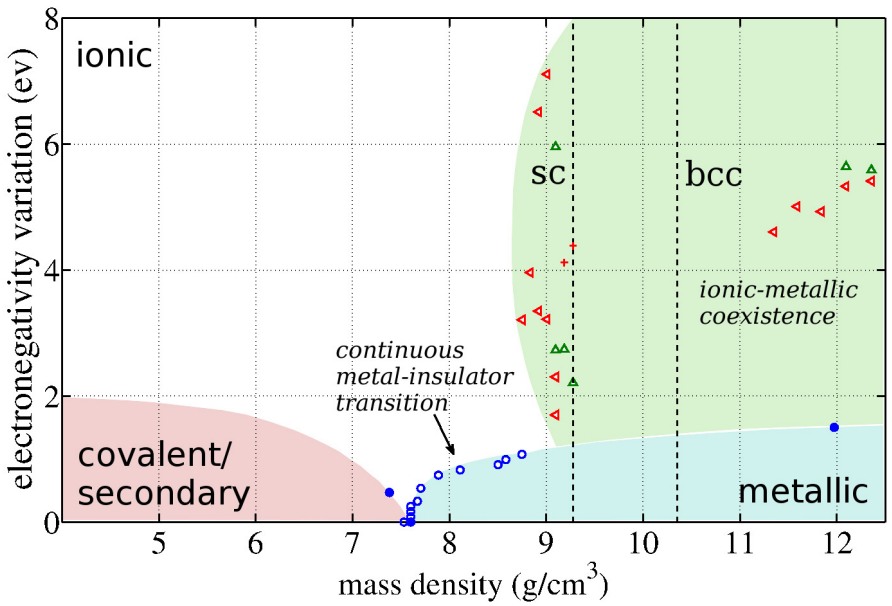

Figure 2.13: Phase diagram of chemical interactions. The abscissa corresponds with the mass density, assuming each atom has the same mass as arsenic. The ordinate gives the absolute value of the electronegativity difference 2ϵ between pseudo-arsenic and pseudo-antimony atoms; the two artificial elements form either the simple-cubic (sc) or body-centered cubic (bcc) structure, by construction; the dashed lines delineate the coexistence of the two phases. The left-bottom corner is occupied by a less-symmetric structure, value of density at ϵ matches that for the transition between rhombohedral and simple-cubic arsenic. See text for explanation of the symbols.

Toward the phase boundary however, the distinction between the two becomes less significant. At the boundary and beyond, the bonding is more uniform. For instance, one the low ϵ end, it could be simple cubic, as in elemental arsenic or phosphorus. On the low density end and for 1:1 stoichiometry, one could have the rock salt or CsCl structure, depending on the ion size ratio. Structures with lower point-symmetries can be envisioned, depending on the stoichiometry.

To extend the phase diagram in Fig. 2.13 to broader ranges in density and electronegativity variation, we will employ the following, unabashedly artificial device,

as afforded by MOPAC: Imagine the rock salt structure, in which the anionic sites are occupied by arsenic, and cationic sites by antimony. Now increase the on-site energies for arsenic by ϵ upward so that new value is $E'_{\mathrm{As}=E_{\mathrm{As}+\epsilon}}$ for each orbital. At the same time, move all the antimony orbitals so that they are ϵ below the unperturbed *arsenic* orbitals in energy: $E'_{\mathrm{Sb}=E_{\mathrm{As}-\epsilon}}$. Next, adjust the orbital exponents on the pseudo-antimony atoms so that the spatial dependences of Sb-As and Sb-Sb inter-orbital matrix elements fit maximally that of the corresponding As-As matrix elements. The resulting fit is good, but not perfect (see Appendix), because of distinct angular dependences of the (valence) orbitals on As and Sb, which correspond to the principal quantum number $n = 4$ and $n = 5$ respectively. Lastly, make the Sb-Sb, Sb-As, and As-As ionic core repulsions identical while reparametrizing then so that the density at which our hypothetical rock salt structure exhibits two transitions: the rhombohedral-to-simple cubic (rh-to-sc) and sc-to-bcc—both match their experimental values for elemental arsenic at $\epsilon = 0$. The need for this re-parametrization is easy to understand since MOPAC's default parameters are optimized for conventional pressures but do not necessarily account for the deformation of the ionic core at high pressures; further detail can be found in the Appendix. We reiterate that even at $\epsilon = 0$, our pseudo arsenic and antimony are not strictly equivalent, because of the aforementioned difference in the angular dependence of the valence wavefunctions.

Now, to move vertically on the phase diagram one varies the quantity ϵ; the quantity 2ϵ is thus the externally imposed portion of the electronegativity differential between the cationic and anionic sites. The latter is the ordinate in Fig. 2.13 by construction. The horizontal axis corresponds with the mass density; the particle

mass is set equal to that of arsenic for concreteness.

From here on, we limit ourselves to the area *outside* the covalent-secondary sector, the latter shown in beige. One should expect a variety of structural transitions involving coordination changes as one moves about on the diagram. We will limit ourselves to just one such transition, viz., 'simple cubic'-to-'body centered cubic' (sc-to-bcc), which is known to occur in elemental arsenic. [59] The latter transition is convenient for modeling pressure-induced coordination changes in that all bonds in the nearest coordination shell are equivalent in both structures, while the coordination itself changes meaningfully during the transition, viz., between 6 and 8. Away from the transition, we fix the structure to be rock-salt and cesium-chloride on the low and high density sides of the phase boundary, respectively; we vary only the density, not structure within individual phases. The (zero-temperature) transition is detected in the standard fashion, by computing the formation enthalpies of the two phases, as functions of volume, and finding the common-tangent to the two curves, [7] see Appendix. This procedure amounts to mutually equating the pressures and chemical potentials of the two phases at zero temperature, aside from any error due to possible differences in the zero-point vibrational energies of the two structures. Because the transition is discontinuous in volume, there is actually a pair of phase boundaries, see Fig. 2.13, the two enclosing the phase-coexistence region. [60] We observe that the transition density is not sensitive to the value of the electronegativity variation. This lack of sensitivity likely indicates a limitation of our pseudo-pnictogen device. Indeed, an ionic crystal with stoichiometry 1:1 and comparable sizes of the cation and anion is expected to have the CsCl structure at ordinary densities. The rock salt

structure would require negative pressure or sufficient mismatch in the ion sizes.

Nonwithstanding its limitations, our artificial procedure allows one to monitor, even if qualitatively, charge redistribution in response to changes in density, electronegativity variation, and coordination. To quantify the spatial distribution of frontier electrons, we directly compute the (average) excess charge $\Delta\rho$ on the more electronegative element relative to the less electronegative element. The amount of charge on an atom is determined by adding the diagonal entries of the density matrix pertaining to the s, p, and d orbital on that atom. The charge differential $\Delta\rho$ gives the strength of the on-site charge density wave. Near the horizontal axis on the diagram, $\epsilon = 0$, $\Delta\rho$ is small, which we associate with metallic bonding in the absence of a bond-order wave. Conversely, at large values of ϵ, the quantity $\Delta\rho$ is large, implying ionic bonding. Because the quantity ϵ couples linearly to the electron density, as in Eq. (2.3), the following statement holds:

$$\Delta\rho = -\frac{\partial E}{\partial \epsilon}, \tag{2.4}$$

where E is the exact energy of the system per atom. (This can be shown explicitly using Eq. (11.16) of Ref. [61].)

We next prepare our pseudo-pnictogen sample for distinct values of the density and electronegativity variation, by performing ϵ sweeps from $2\epsilon = 0$ to 8 eV, while keeping the density fixed. The sample size is 64 atoms for the sc structure, 54 atoms for the bcc structure; the finite size effects are treated according to a standard procedure. [62] We observe that below a certain threshold density, the energy and wavefunction of the system depend smoothly on the value of epsilon. Above

that threshold density, the dependence is more complicated, the sample transitions between distinct energy terms, see Fig. 2.14(a). Each term crossing is accompanied by a discrete change in charge distribution, see Fig. 2.14(b). Because of such crossings, the wavefunction and energy show a hysteretic behavior during ϵ sweeps (see Appendix). Both ϵ increments and the convergence tolerance for the SC HF procedure are finite, of course. The locations of the corresponding term-crossings can be detected; some are indicated on the phase diagram in Fig. 2.13.

The occurrence of the multiple terms and term crossings is expected. Already small molecules exhibit many-particle excited states; distinct terms generally correspond to distinct values of local polarization, as is the case here. Here we observe a rather special situation that term crossings at the *ground state* energy begin to occur only above a certain mass density. Below that threshold density, there is no sharp distinction between states characterized by relatively low and high local polarization, the latter reflected in the value of the charge differential $\Delta\rho$. In contrast, the two states in high-density samples correspond to different terms and, as such, may be regarded as distinct *phases* corresponding to distinct degrees of electron localization. This is brought home by introducing the Legendre transform of the energy, $E^{(\mathrm{inh})}(\Delta\rho)$, which can be treated naturally as a function of $\Delta\rho$:

$$E^{(\mathrm{inh})}(\Delta\rho) = E[\epsilon(\Delta\rho)] + \epsilon(\Delta\rho)\,\Delta\rho, \tag{2.5}$$

where

$$\epsilon(\Delta\rho) = \frac{\partial E^{(\mathrm{inh})}(\Delta\rho)}{\partial\Delta\rho}. \tag{2.6}$$

The label "inh" signifies that the thermodynamic potential $E^{(\mathrm{inh})}(\Delta\rho)$ is inherently

a functional of the electronic density distribution. The existence of such a functional is guaranteed by the Hohenberg-Kohn theorem. [5] In such a density-based approach [7], one can unambiguously determine the field necessary to achieve a specific strength of the CDW if desired, via Eq. (4.14). The thermodynamic potentials $E^{(\mathrm{inh})}(\Delta\rho)$ and $E(\epsilon)$ are analogous to the Helmholtz and grand-canonical free energy, respectively. [63]

Fig. 2.15(a) displays the term crossing from Fig. 2.14 in terms of the inherent energy $E^{(\mathrm{inh})(\Delta\rho)}$, at mass density 9.01 g/cm^3. The latter figure explicitly illustrates a discontinuous transition between two states, where the quantity ϵ_0 gives the slope of the common tangent to the two terms. Particularly illuminating is the graph of the quantity $\widetilde{E}^{(\mathrm{inh})}(\Delta\rho) \equiv E^{(\mathrm{inh})}(\Delta\rho) - \epsilon_0\,\Delta\rho$, where ϵ_0 is a constant, not a function of $\Delta\rho$; see Fig. 2.15(b). When the conditions for equilibrium for any pair of states are met, the corresponding two minima have the same depth. Note that the term crossing in Fig. 2.15 is only possible because there are more than one orbital per site. Otherwise, the variable $\Delta\rho$ would specify the charge distribution uniquely, which would then imply that to the same density distribution, there correspond more than one energy functionals, a physical impossibility. [5] We have checked that the individual contents of the s, p, and d orbitals corresponding to the two terms in Fig. 2.15 do exhibit discontinuities at the term crossing.

The l.h.s. and r.h.s. minima in Fig. 2.15(b) correspond to states with a lesser and greater degree of electron localization. The presence of a barrier separating those states can be traced to a very familiar phenomenon, viz., the lack of mutual miscibility of oil and water. Indeed, states characterized by distinct degrees

of electron localization with also exhibit distinct polarizabilities, hence the analogy. The hysteretic region on the phase diagram formally corresponds to a *coexistence* of two phases. The coexistence region exhibits an electronic pattern that interpolates between those typical of metallic and ionic bonding, the latter formally corresponding to maximally extended and localized bonding orbitals. Thus we identify the ionic/metallic coexistence region with the intermediate case of the *multi-center* bond, see also Section 2.5.

We emphasize that although we have treated local electronegativity as a continuous variable, in practice the choice of ϵ is limited to that afforded by specific chemical elements. The presence of discontinuous transitions of the kind shown in Fig. 2.15 presents an additional complication: Even if realizable chemically in principle, the electronegativity variation ϵ_0 may not be achievable in an actual compound since the resulting charge density wave with a spatially uniform strength is unstable toward phase separation. In the best case scenario, the compound will be a collection of stripes whose CDW strength alternates between $\Delta\rho_1$ and $\Delta\rho_2$. In the worst case, the compound will not form altogether. Conversely, no such complications arise at sufficiently low mass densities.

The present calculations thus imply that depending on the density, a transition between states with distinct magnitudes of the CDW can be generally either continuous or discontinuous. This means, in particular, that that the metal-insulator transition can be either continuous or discontinuous. (Note we are not considering effects of disorder. [28, 64]) The possibility of a continuous localization transition in electronic systems is in contrast with classical liquids made of rigid particles, which

always transition from the uniform liquid into a solid discontinuously. [7,65–67] This contrasting behaviors may come about for the following reason: Classical particles are the sole source of mutual confinement; the resulting bounding potential emerges self-consistently. In contrast, the electrons in solids are already subject to the field of largely stationary nuclei. Thus the field already lowers the full translational symmetry that would be characteristic of a free electron gas, the precise extent of symmetry-breaking determining whether electric conductance vanishes. The presence of this symmetry lowering may enable further localization to be continuous. Incidentally, note that the transition in Figs. 2.14 and 2.15 is only weakly discontinuous; its analog in an actual material may not be easily distinguished from a continuous transition or a soft crossover.

Outside the coexistence region, the ionic and metallic bonding may be viewed as extremes of a continuum of interactions, since there is no sharp boundary. Still, there may be some demarcation between the interactions, in the form of a Fisher-Widom-like line. [68] To test for this possibility, we compute the so called electron localization function (ELF) [69, 70] outside the co-existence region. The ELF is determined by the curvature of the spherically averaged conditional pair probability for the electrons. By construction, the ELF varies between zero and one, [71] the two extremes corresponding to perfect localization and a uniform electron gas respectively. Surfaces of constant ELF=1/2 may be thought of as separating metallic from ionic regions. [71] The metallic regime sets in when the metallic regions percolate the space, see Fig. 2.16.

To estimate the mass density when such percolation takes place, a higher level

approximation is desirable. We have computed the wave functions for rock salt structures made of actual pnictogens: As, SbAs, BiAs and BiP, using the plane wave pseudo-potential method (PSPW) method in NWChem, [41] and PBE96 exchange-correlation potential. A 64 atom repeat unit was used. Note that AsP, BiAs and SbAs solids have been reported experimentally. [72] Because the phase diagram is constructed with two arsenics in mind, we must readjust our results to account for the difference in the atomic size and mass of the diatomic compounds from elemental arsenic. We used the critical sizes from Fig. 2.10 as the rescaling factor for the length. The so obtained points for the metal-insulator transition more of less fall onto one line, which extends from the rh-to-sc transition at $\epsilon = 0$ to the coexistence region between the metallic and ionic bond.

In an alternative way to demarcate regions of predominantly metallic and ionic bonding, outside the coexistence region, we have tested the stability of our pseudo-pnictogen rock salt structure with respect to deformation toward the rhombohedral structure, Fig. 2.12, see details in Appendix. This instability line is seen to lie close to the Fisher-Widom line. This suggests a deep connection between the structural instability and propensity for electron localization (or lack thereof) in symmetric structures. The latter suggestion, in turn, is consistent with our recent findings on localization in small molecular fragments. [49]

In parallel with Section 3.4, we now address the interplay of cohesive and repulsive interactions in density-driven transitions accompanied by coordination changes. The two interactions often move in the same direction: Both the electron density in the inter-atomic space and the repulsion between the ionic cores tend to increase

with density. A qualitative, Le Chatelier-like criterion can be stated for whether a change in coordination is driven primarily by steric repulsion or cohesive interactions. First note that the interatomic distance r can either decrease or increase upon a discontinuous volume change. For instance, a simple formula interpolates the relation between the specific volume v and coordination number n for the diamond, simple cubic, and bcc lattice: $r \approx [0.16vn]^{1/3}$, $(n \leq 8)$. Now, consider a pressure-driven transition with $\Delta v < 0$ and $\Delta n > 0$. If the distance r *increases*, then the increase in the coordination was to counteract the effects of steric repulsion; hence the latter can be cited as the dominant factor in the coordination increase, while the reverse transition can be thought of as driven by cohesive interactions. For instance, for a pressure-driven sc-to-bcc transition, $n_{\rm bcc}/n_{\rm sc} = 4/3$. For such a transition to be driven by cohesive forces, the volume decrease would have to be 25%; we are not aware of such large density changes for phase transitions in condensed phases. In contrast, for the bcc-to-fcc transition, $r_{\rm fcc}/r_{\rm bcc} \approx (1.09\, v_{\rm fcc}/v_{\rm bcc})^{1/3}$, and so already a 10% change in volume would imply cohesive interactions are important. An elegant discussion of pertinent electronic processes can be found in Ref. [73]

The above ideas help to resolve a seeming contradiction: [74] On the one hand, there is an empirical correspondence rule stating that lighter elements under high pressures tend to form structures typical of elements down the group at normal pressures. [74, 75] At the same time, heavier elements tend to exhibit less *sp*-mixing and higher coordination, [14] the di-pnictogen tri-chalcogenide representing a good example. [9] On the other hand, we have seen that the amount of *sp*-mixing should increase with density. This seeming contradiction may be resolved in the following

way: The *sp*-mixing should indeed increase with density for a fixed or mildly deforming structure. Eventually, however, a density-driven structural transition causes a coordination increase that leads to a longer bond and lesser amount of *sp*-mixing. It is this kind of transition that ultimately results in a decreased amount of *sp*-mixing with a sufficient increase in mass density. The increased coordination on the one hand, and the decreased amount of bond directionality as caused by *sp*-mixing on the other hand, are hallmarks of the metallic interactions. Thus we identify the $\rho \to \infty$, $\epsilon \to 0$ limit with metallic interactions and delocalized electrons. On the other hand, for any value of density, one may always choose a large enough electronegativity difference to force the valence electrons to localize on the more electronegative atoms. Thus we identify the $\epsilon \to \infty$ limit with the ionic bond and conclude that the coexistence region widens, in terms of ϵ, with density. The above reasoning does not straightforwardly apply when coordination, too, changes with density, especially when some bonds become shorter and others longer, as in Fig. 2.1. At least in the case of rhombohedral arsenic, it is still possible to argue, see the Appendix, that the amount of *sp*-mixing decreases with density.

2.5 Discussion

The present work views the canonical chemical interactions as underlying distinct thermodynamic phases. Consequently, the interactions can be viewed as distinct sectors on a phase diagram. We have argued that in the most minimal description, such a phase diagram is in the space formed by two variables, particle density

and local electronegativity variation. The conventional, two-center covalent bond and closed-shell interactions can be thought of as mutually-complementary, intrinsic counterparts that occupy the very same sector on the phase diagram of chemical interactions. The intrinsic connection between the covalent bond and closed shell interaction is that the two are symmetry broken versions of the multi-center bond. In turn, the multi-center bond can be thought of as a coexistence, hybrid between the metallic and ionic bond.

The metallic and ionic bond thus emerge as the two most fundamental interactions that become entirely distinct in the high density limit. The distinction can be understood qualitatively as poor mutual miscibility of delocalized and localized electrons. The former can be thought of as an electron fluid that can flow despite the partial breaking of the translational symmetry due to the nuclei. In insulators, the translation symmetry breaking is complete. Phase separation in electronic systems and associated striped phases has been reported by Schmalian and Wolynes, [24] who have suggested such separation is pertinent to metal ammonia solutions and high T_c superconductors. The present model analysis shows the distinction between the metallic and ionic interactions decreases as the density is lowered, until the two become two opposite limits of a *continuum* of interactions. At even lower densities, the number of electrons in the inter-atomic space becomes insufficient to support the multicenter bond; [49] the latter thus breaks into the covalent bond and the closed-shell interactions, provided the electronegativity variation is not too large. The resulting charge-density wave can be thought of as a bond-order wave.

The interatomic spacing in condensed matter is a natural lengthscale in bonded

systems; it is, in turn, largely determined by the Bohr radius. Structures characterized by *supra*-atomic lengths can be often thought of as made of small "building blocks" that are perturbed only weakly when the solid is assembled; this is the case with many oxides and halides, for instance. Complex inorganic solids made of subunits that are individually stable can have unit cells that contain as many as tens of thousands of atoms. [76, 77] Alternative types of ordering are possible—even if on a modest length scale—where the type of bonding within the building blocks will depend on whether the blocks are standalone or bonded together, as in Fig. 2.2(a). This suggests that there is an emergent length scale in condensed phases that is not directly tied to the atomic scale. In the present picture, such supra atomic length scales are widths of interfaces that arise when distinct interactions coexist spatially. The simplest formalism to describe such a coexistence is via the Landau-Ginzburg free energy functional: [78–80]

$$F = \int dV \left[\frac{\kappa}{2} (\nabla \phi)^2 + \mathcal{V}(\phi) \right], \tag{2.7}$$

where $\kappa > 0$ is a phenomenological coefficient reflecting the free energy penalty for spatial inhomogeneity in the order parameter ϕ. The bulk free energy density $\mathcal{V}(\phi)$ has two or more minima corresponding to coexisting phases, such as that in Fig. 2.15.

Sufficiently far from the critical point, the meanfield description embodied in the functional (2.7) becomes quantitative; the interface width $l_{\rm intf}$ scales roughly as $(\kappa/g^{\ddagger})^{1/2}$, where $g^{\ddagger}$ is the height of the barrier in the bulk energy $\mathcal{V}(\phi)$ that separates the corresponding pair of phases. The interface tension coefficient is of the order $(\kappa g^{\ddagger})^{1/2}$. At the critical point, which formally corresponds to the $g^{\ddagger} \to 0$ limit, the meanfield approximation is only qualitative, however it still correctly predicts that

the interface width diverges, while its tension vanishes. The correlation width also diverges at the critical point and so does the susceptibility, [30] implying a structural instability, such as that at the simple cubic-to-rhombohedral transition in elemental arsenic. It is thus likely that the length scale associated with the coexistence will always remain finite. Consequently, the hybrid of two distinct types of bond is the multi-center bond. The latter bond is directional, even if its progenitors—such as the ionic and metallic bond—are not. The directionality comes about already because of the stiffness of the interface; the presence of a surface breaks the isotropy of space. This is consistent with the notion of the multi-center bond being a hybrid interaction and, hence, with the much more intuitive explanation of bond directionality via hybridization of atomic orbitals.

The interface width decreases with the separation from the critical point; once it becomes less that the interparticle-spacing, there are at least two alternative possibilities: At low densities (or for lighter elements), the multi-center bond is replaced by a coexistence of the two-center covalent bond and secondary interactions, as in Fig. 2.2(b). The Bi_2Te_3 structure in Fig. 2.2(a) corresponds to intermediate densities; here the multicenter bond is still present and forms an interface between covalent/secondary regions. Exclusively covalent bonding is also possible for particular electron counts, as in the diamond structure. (Note the C-C bond length in diamond is still longer than that in graphite.) At higher densities, metallic and ionic interactions become well-defined individually, but could also spatially coexist as in layered compounds where current is purveyed within select layers.

One thus arrives at the notions of the familiar two-center bond and bond directionality—intrinsically atomistic concepts—starting from a *coarse-grained* picture, such as that described by the (classical) density functional in Eq. (2.7). Such a coarse-grained view is far from new; it underlies the venerable density-functional theory, [5, 81] of course. Here, we find that some results of *classical* density functional treatments are transferable to electrons, such as poor miscibility of localized and delocalized particles. Furthermore, the idea of coarse-graining is central to the renormalization group (RG) theory of phase transitions. Coarse-graining transformations can be thought of as movement in the space defined by coupling constants. [30] Distinct phases come about as attractive fixed points for such transformations. The present results suggest the ionic, metallic, and covalent/secondary interactions are such attractive fixed points, the latter essentially corresponding with the corners of the venerable Arkel-Ketelaar triangle. [18–21]

Laws of corresponding states arise when the system is close to a critical point, where the RG flows of the coupling constants are not sensitive to system-specific detail other than the symmetry and range of interactions because the correlation length now greatly exceeds molecular lengthscales. Long wavelength patterns that may arise as a consequence of such instabilities are difficult to predict using ab initio methods, because the size of the repeat unit, if any, of the distorted structure is not a priori known. An example of such complex distortions, of recent note, is hybrid organic-lead halide perovskites. [82] It is quite possible that the multiplicity of mutual orientations of the the corner-sharing octahedrons in those compounds scales exponentially with the sample size thus limiting the utility of brute force, ab

initio approaches. A hybrid strategy may seem more profitable, in which one uses such ab initio methods to infer the parameters for a coarse-grained description in the form of a free-energy functional, such as those that have been used to study displacive transitions and multiferroic behavior. [38, 39] (Examples of such inference for simple liquids and spin systems can be found in Ref. [7]) The resulting functional can be tested, in principle, for the multiplicity of states. [83–86] Conversely, textbook approximations to canonical bonding schemes should work close to attractive fixed points. Near phase boundaries—not too close to critical points, if any—one should expect local ordering on modest length scales.

Of course the present, coarse-grained view of the chemical interaction cannot replace detailed quantum-chemical analyses for the stability of known compounds. Rather, we believe the present findings complement those detailed analysis and, in particular, may provide an additional avenue for predicting novel compounds. For instance, they may help one to predict whether specific ingredients will bind to form a stable or metastable solid, as opposed to segregating into unwanted products. Indeed, insofar as localized electrons are tied to regions with significant electronegativity variation—and vice versa for the delocalized electrons—the mutual miscibility of the corresponding moieties is tied to that of the respective electronic subsystems. The latter mutual miscibility seems a natural variable for machine-learning algorithms that have been used for predicting the existence and properties of compounds. [87–89] The present results also suggest that multiferroic materials and any other solids prone to structural instabilities should be relatively close to the critical points and phase boundaries on the phase diagram in Fig. 2.13. Note that while achieving

uniformly high densities in the bulk may require substantial compression, locally-dense environment can be created using chemistry even at normal conditions, for instance, by substituting elements by their heavier neighbors down the group.

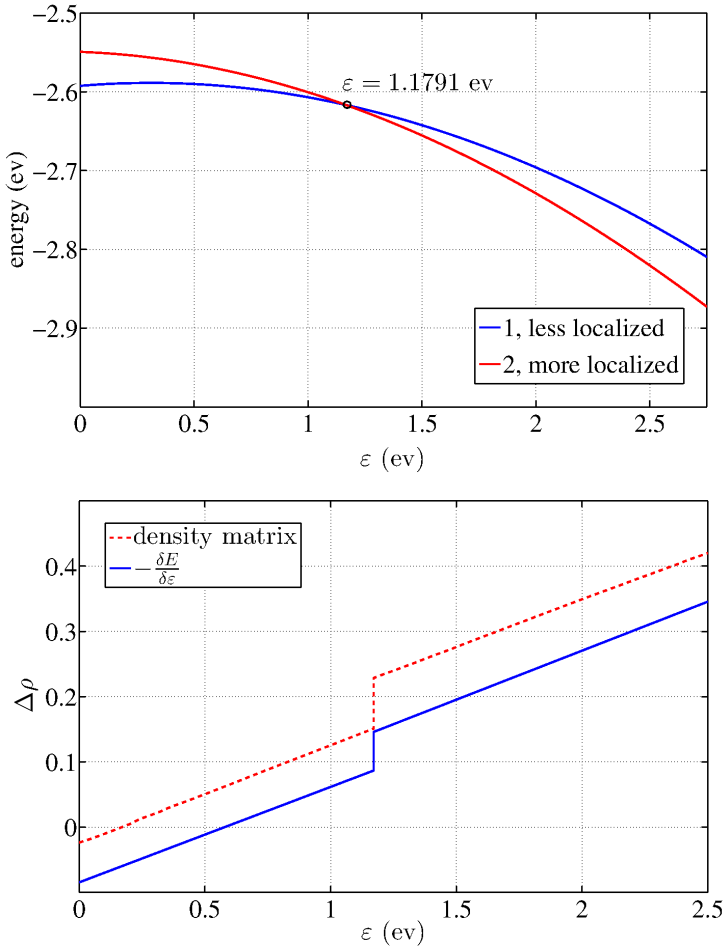

Figure 2.14: **(a)** A specific instance of term-crossing for the ground state of the pseudo-pnictogen compound from Fig. 2.13. **(b)** The corresponding dependence of the electron density differential $\Delta\rho$ as determined directly using MOPAC-computed density matrix and by numerically differentiating the $E(\epsilon)$ curves from panel (a). The differentiation was performed using the best parabolic fit to the $E(\epsilon)$ curves. Although numerically similar, the two curves are not identical because MOPAC does not solve the Schrödinger equation exactly. In both panels, the horizontal axis ε represents the difference in electronegativity between the two atom types in the solid. In panel (b) the differential quantity $\Delta\rho$ on the vertical axis is derived from the dimensionless electron (probability) density

.

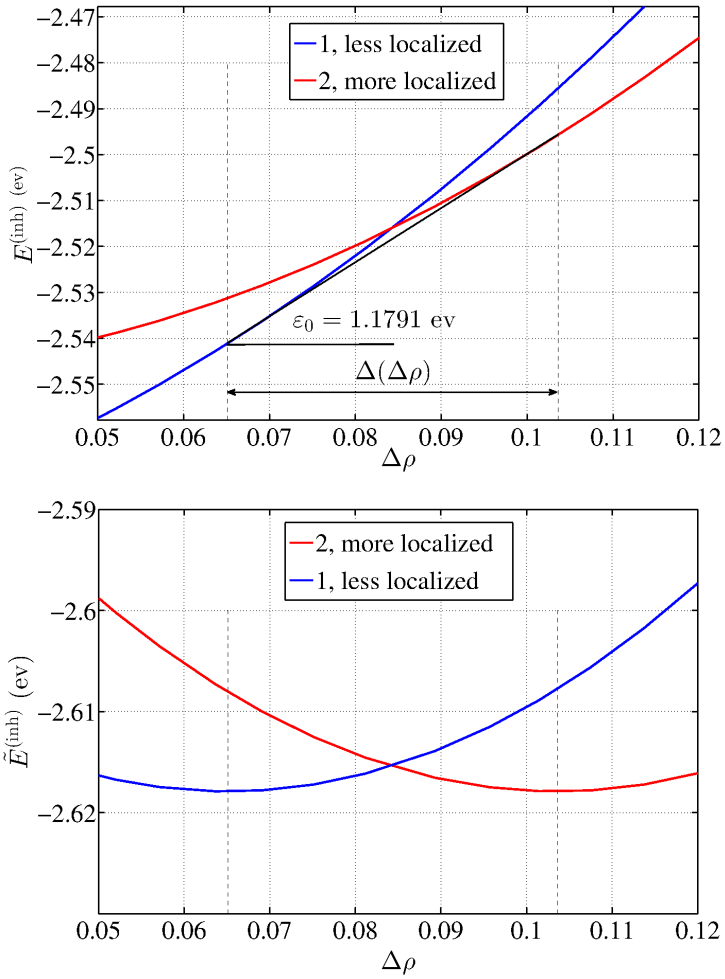

Figure 2.15: **(a)** The inherent electronic energy from Eq. (2.5) as a function of the electron density differential $\Delta\rho$, corresponding to Fig. 2.14. **(b)** The modified energy $\widetilde{E}^{(\mathrm{inh})}(\Delta\rho) \equiv E^{(\mathrm{inh})}(\Delta\rho) - \epsilon_0\,\Delta\rho$ whose minima correspond to the equilibrium values of $\Delta\rho$ when the externally imposed electronegativity variation is equal to ϵ_0.

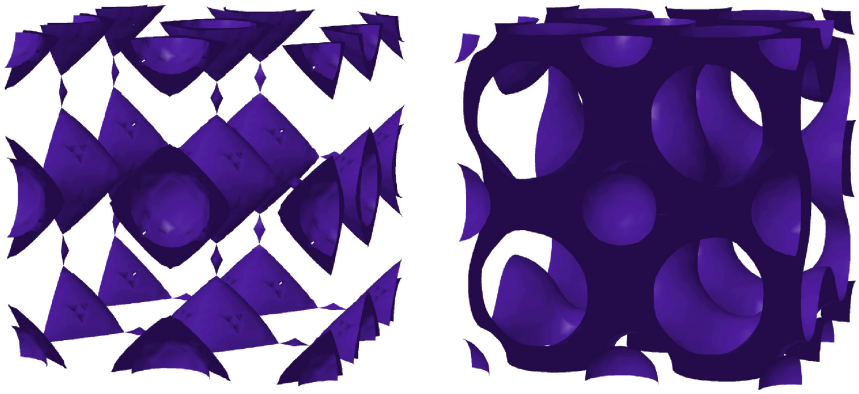

Figure 2.16: *Left*: The ELF=1/2 surface at the onset of metallicity. *Right*: The ELF=1/2 surface in the metallic regime. In both panels, the metallic and ionic regions are shown as filled and empty region, respectively. The cavities correspond to the ionic cores.

Chapter 3

Bond assignment as a symmetry breaking

3.1 Overview

We report cases of the apparent bond order and participation number—as determined by a standard quantitative procedure—changing in an abrupt, sigmodal manner upon a modest distortion of the molecule. The corresponding localized molecular orbitals undergo a symmetry breaking through the transition, while the electronic wavefunctions change only gradually. Except within narrow transition zones, the bond order is shown to be robust with regard to bond distortion. We thus argue that the venerable concept of the chemical bond is well defined, even though the bond assignment may depend sensitively on the stereochemistry; the robustness can be traced to symmetry changes of the localized wavefunctions of bonding electrons

being intrinsically discrete. We use several specific examples, molecular and solid-state, to argue that stable or metastable configurations can be viewed as resonances of localized two-center bonds, be the actual bonding orbitals multi-center or not; the bond pattern generally has a lower symmetry than that of the underlying molecule or solid. Conversely, the lack of covering of the molecule by localized two-center bonds reveals structural instabilities without the need to geometrically optimize the molecule, thus suggesting a high-througput, automated procedure for screening candidate compounds and structures with regard to stability.

3.2 Motivation

Chemical bond is an umbrella term for a set of approximations used to predict structures and stability for small molecules and macroscopic solids alike; it is also a quintessential teaching tool. Even when the number of cohesively interacting atoms is infinite—as in a solid—it is often possible to view the corresponding, apparently muliti-center bond as a combination of simple, *two*-center bonds. For instance in rhombohedral arsenic, each atom can be thought of as making three single bonds with its nearest neighbors, while its lone pair interacts relatively weakly with lone pairs on closeby atoms; each atom satisfies the Lewis octet rule [9, 21]. Apparent departures from the concept of a two-center bond are common and can be found already in the form of a three-center, four-electron bond, a classic bonding model for the I_3^- molecule. [15, 16] While the latter molecule is technically hypervalent, it is not difficult to devise a three-center/four-electron bonding configuration that obeys

perfectly the Lewis octet rule, such as the trimeric, near linear motif AsH_2-AsH-AsH_2. As such, the latter molecule conforms with traditional notions of two-center bonding. The assignment of a chemical bond with regard to its order, the number of centers it involves, and its character (covalent, ionic, secondary, etc.) is non-unique and approximation-dependent. Under such circumstances, one may resort to empirical criteria such as the bond directionality [1] or the stability or reactivity of the molecule in question; see the insightful discussion in Ref. [90].

The present study focuses on two specific sources of ambiguity in assigning the bond order. On the one hand, the value of the bond order reflects the number of electrons mediating the cohesive interaction; the molecular orbital (MO) theory, for instance, defines it as the electron-pair count of the bonding molecular orbitals in access of the anti-bonding orbitals. The so-defined bond order, by construction, is integer or half-integer valued and should be robust with respect to modest variations in the bond length, such as those due to vibrations. Yet the identification of bonding vs. non-bonding vs. antibonding orbitals is generally ambiguous. [90] There are other recipes to assign the bond order, such as the *localized molecular orbital* [45–47, 91, 92] analysis that we will employ in the following, in which the bond order is a function of the molecular orbitals. As such it is expected be a priori a smooth function of the nuclear coordinates. This seems to contradict the expectation that the bond order should remain approximatly constant within a substantial range of nuclear coordinates while changing in an abrupt manner when, for instance, the bond is broken. From a purely empirical viewpoint, a potential lack of robustness of the concept of the bond order is suggested, for instance, by the systematic study

of near-linear trimeric motifs—halcogen-pnictogen-halcogen and halcogen-chalcogen-halcogen—in thousands of compounds by Landrum and Hoffmann. [1] When the trimer is sufficiently short, the two bonds are equal in length; the overall bonding may be argued to be three-center. [93] Above a certain critical length, the spatial symmetry becomes broken in that one bond is shorter than the other. For sufficiently long trimers, the short bond can be empirically associated with the covalent and the longer with a closed-shell, secondary interaction. Thus, the change in the bonding character, from three-center to covalent-secondary, is directly related to the spatial symmetry breaking. The relation can be argued to be mutually causative in that the presence or absence of symmetry is decided self-consistently. [94]

Here we report that even when the above spatial symmetry breaking is prevented, density changes will still drive a special transition accompanied by a symmetry breaking that is inherently *electronic* in character. The transition consists in an abrupt change of the apparent bond order and in the number of bonding electrons, despite very modest changes in bond lengths and molecular orbitals. At the same time, the symmetry of the effective wave functions for the bonding electrons changes during the transition; the symmetry is lowered on the higher density side of the transition. Aside from this transition, however, the bond order and related quantities—all being anthropocentric measures of bonding!—are indeed found to be robust with respect to bond deformation. These notions may be restated in the following form: The redistribution of charge during density changes takes place in a graduate fashion and is indeed expected, because of the additive effects of the fields due to the nuclei; the electrons can be sourced from or sequestered to other bonds and/or lone pairs.

Despite this gradual nature of charge transfer, we find that the bond order stays nearly constant when the atoms move. When the bond order changes, it does so in an abrupt fashion, thus justifying the conventional use of traditional bonding concepts. According to the present results, the apparently sigmoidal fashion in which the bond order changes can be traced to the following fact: When symmetry changes, it must do so in a discrete fashion. We reiterate that the symmetry in question is that of the localized molecular orbitals (LMOs), which generally are different from the canonical molecular orbitals. The LMOs are effective, localized wavefunctions for bonding electrons.

Further, we observe that on the high density side of the transition, the LMOs tend to become two-center and fully cover equivalent bonds; the LMOs themselves may not be equivalent. On the lower density side, we find that the LMOs either becomes multi-center or remain two-center while covering only a portion of equivalent bonds. Given this lack of bonding electrons, one must then choose to which pairs of (nearby) atoms one must assign bonds. The ambiguity in two-center bond assignment or lack of coverage by localized two-center bonds, we argue, may signal structural instabilities and other interesting phenomena. Such is the case, for instance, with the cyclo-butadiene (but not benzene!), where the ambiguity reflects a second-order Jahn-Teller instability. [25] Here we find that for a given solution of the electronic problem, finding the effective, localized wavefunctions for bonding electrons is unambiguous in that distinct solutions are equivalent. Finally, note that while identifying instabilities, the localized-bond assignment does not generally predict the final geometry following the distortion.

The article is organized as follows: Section 3.3 reviews several basic notions of the LMO formalism, which sets the stage for a symmetry-based analysis, in Section 3.4, of bonding in hydrogen-passivated trimers AsH_2-AsH-AsH_2 and AsH_2-AsH_2-AsH_2. The latter correspond with a three center, four and three electron bond respectively, at appropriate lengths. In Section 3.5, we demonstrate a variety of symmetry breakings for bonding orbitals and the intrinsic ambiguity of assigning bonds in larger bonding configurations, namely cyclic molecules $(AsH_2)_n$ and elemental arsenic. Section 4.5 summarises the present findings and discusses how they could be used to speed up the prediction of new compounds and structures.

3.3 Bonding from the viewpoint of localized molecular orbitals

We will characterize bonding using the localized molecular orbitals (LMO) formalism. Originally inspired by symmetry adapted orbitals in relatively symmetric molecules, the localized molecular orbitals can be assigned for arbitrary geometries: Given a set of *occupied* molecular orbitals ψ_i, one transforms to an alternative set of orthonormal orbitals χ_j such that a certain quantity reflecting the self-repulsion within individual new orbitals is maximized. [45–47, 91] Specifically, here we adhere to the Edmiston and Ruedenberg approach [46], whereby one maximizes the quantity $D_\chi \equiv \sum_j \int d^3\boldsymbol{r}_1 d^3\boldsymbol{r}_2 |\chi_j(\boldsymbol{r}_1)|^2 V(r_{12}) |\chi_j(\boldsymbol{r}_2)|^2$ or, equivalently, minimizes the mutual repulsion among distinct orbitals in the form of the quantity: $\sum_{j<k} \int d^3\boldsymbol{r}_1 d^3\boldsymbol{r}_2 |\chi_j(\boldsymbol{r}_1)|^2 V(r_{12}) |\chi_k(\boldsymbol{r}_2)|^2$. Here, $V(r_{12})$ stands for a purely repulsive

potential energy function. The LMOs are generally not eigenfunctions of an effective one-particle hamiltonian, such as that arising in the Hatree-Fock approximation. Instead, they represent an attempt by an interpreter to redistribute the electrons among orthonormal, maximally localized orbitals, each of which thus binds together the smallest number of atoms. The latter number serves as a lower bound on the number of centers in a bond; the bound is not unique because it depends on the specific choice of the test function $V(r_{12})$, which is made according to one's convenience and computational means. For instance, $V(r_{12}) = r_{12}^{-1}$ implies localization with respect to (non-screened) Coulomb repulsion. A more computationally convenient choice is $V(r_{12}) = \delta(\boldsymbol{r}_{12})$, which simply yields $D_\chi = \sum_j \int d^3\boldsymbol{r}|\chi_j(\boldsymbol{r})|^4$.

The above procedure is significantly simplified when the one-electron energy function is diagonalized while neglecting the overlap between distinct atomic orbitals, as is the case for certain semi-empirical approximations. [91] Hereby, one can present the integral $\int d^3\boldsymbol{r}|\chi_j(\boldsymbol{r})|^4$ as a sum over distinct atoms: $\sum_A \int_A d^3\boldsymbol{r}|\chi_j(\boldsymbol{r})|^4$, where the integrations are over regions occupied by distinct atoms. Each such integration yields a quantity that scales inversely proportionally with the atom's volume. Insofar as we are interested in the partitioning of the electrons between atoms, irrespective of the extent of the atomic orbitals, the above sum can be profitably replaced by a (dimensionless) expression, viz.:

$$\int d^3\boldsymbol{r}|\chi_n(\boldsymbol{r})|^4 = \sum_A \int_A d^3\boldsymbol{r}|\chi_n(\boldsymbol{r})|^4 \rightarrow \tag{3.1}$$

$$n_j \equiv \sum_A \left(\sum_{\lambda_A} C^2_{\lambda_A j} \right)^2, \tag{3.2}$$

where we have expanded the localized orbital $\chi_j(\boldsymbol{r})$ in terms of the atomic orbitals

ϕ_{λ_A}:

$$\chi_j(\boldsymbol{r}) = \sum_A \sum_{\lambda_A} C_{\lambda_A j} \phi_{\lambda_A} \tag{3.3}$$

and the index λ_A labels the atomic orbitals on atom A. As already mentioned, $\int dV \phi_\lambda \phi_\mu = \delta_{\lambda\mu}$, implying $\sum_A \sum_{\lambda_A} C^2_{\lambda_A n} = 1$. The quantity n_j clearly provides the participation number of distinct centers to the localized orbital j, and is appropriately called the *bond-center number*. [91] For a lone pair, one immediately gets $n = 1$, for an occupied two-center bond corresponding to the MO (and LMO) $\chi = \psi = \alpha\phi_1 + \beta\phi_2$, $(\alpha^2 + \beta^2 = 1)$ the bond center number, $n = [\alpha^{-4} + (1-\alpha^2)^{-2}]^{-1}$, is maximized at 2 for a covalent bond, $\alpha = 1/\sqrt{2}$, and is minimized at the lone pair value 1 for a purely ionic bond, $\alpha = 0, 1$. For a linear trimer with two equivalent bonds and one orbital per center, one may use the Hückel energy function:

$$\widehat{H} = -\begin{pmatrix} 0 & \beta & 0 \\ \beta & 0 & \beta \\ 0 & \beta & 0 \end{pmatrix}. \tag{3.4}$$

The corresponding MO's are shown graphically on the l.h.s. of Fig. 3.1. The lowest-energy MO is $\psi_1 = \phi_1/2 + \phi_2/\sqrt{2} + \phi_3/2$ and the (formally) non-bonding MO is $\psi_2 = (\phi_1 - \phi_3)/\sqrt{2}$. If only the *ground* state MO contributes to bonding, one gets $n = 8/3$. This value is less than three, in reflection of the non-uniform distribution of charge among the three centers, viz., 1/4, 1/2, and 1/4 respectively. For comparison, the bond-center number for a tree-center bond with three equivalent centers, $\chi = \psi = (\phi_1 + \phi_2 + \phi_3)\sqrt{3}$ exactly equals 3. The partial ionic character of the three-center bond for a linear trimer made of otherwise equivalent atoms was noted a while ago by Musher. [17] In the case when MO2 is actually bonding, there are two LMOs.

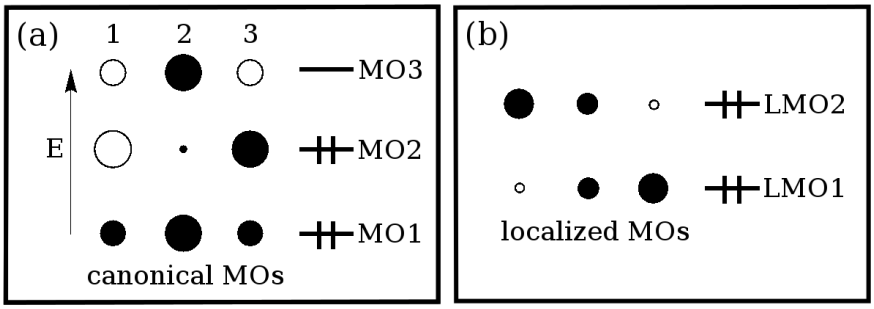

Figure 3.1: **(a)** Graphical representation of the eigenvectors of the three-orbital Hückel energy function (3.4). **(b)** The localized molecular orbitals (LMOs) corresponding with panel (a). Note that the two orbitals have the same energy, $(E_1 + E_2)/2$.

Direct computation shows $\chi_{1,2} = (\psi_1 \pm \psi_2)/\sqrt{2}$, the two shown graphically on the r.h.s of Fig. 3.1. The two LMOs are equivalent in that they are mirror images of each other and each can be associated with a one-electron energy $(E_1+E_2)/2$. (Generally, to the j-th LMO $\chi_i = \sum_l c_{jl}\psi_l$, one may associate an energy $E_j = \sum_l c_{jl}^2 E_l$, where the summations are over the occupied MOs.) The bond number for each of the two LMOs is $n_{1,2} = 32/19$, which is just short of 2. This (modest) deficit is, again, due to the non-uniform distribution of charge among the three centers. Still, insofar as the bond-center numbers for the two LMOs are numerically close to 2, the 3 center/4 electron bond can be thought of as two adjacent two-center bonds.

A useful pattern emerges from the above trimer example already at the Hückel level: If a molecule has a mirror symmetry plane and has two bonding molecular orbitals of opposite parity, the two resulting LMOs are necessarily mirror images of each other. (This pattern does not necessarily hold when the number of MOs exceeds two, whether that number is even or odd.) If only one LMO is present, on the other hand, it must be either odd or even with respect to reflection in the symmetry plane.

As a measure of the bond order for a two-center bond connecting atoms A and B, one may evaluate the number of electrons shared by these according to: [95]

$$B_{AB} \equiv \sum_{\lambda_A, \lambda_B} P^2_{\lambda_A \lambda_B}, \tag{3.5}$$

where $P_{\lambda\mu}$ is the density matrix:

$$P_{\lambda\mu} \equiv 2 \sum_i \widetilde{C}_{\lambda i} \widetilde{C}_{\mu i}, \tag{3.6}$$

the summation being over the occupied MOs, and the $\widetilde{C}$s are the expansion coefficients for the MOs in terms of the atomic orbitals:

$$\psi_i(\boldsymbol{r}) = \sum_A \sum_{\lambda_A} \widetilde{C}_{\lambda_A i} \phi_{\lambda_A}. \tag{3.7}$$

The quantity in Eq. (3.5) is often called the "Wiberg bond index." [95] For a lone pair, $B = 0$ automatically. For a two-center bond, $\psi = \alpha\phi_1 + \beta\phi_2$, $B_{AB} = 4\alpha^2(1 - \alpha^2)$; it varies between 0 and 1, the two extremes corresponding to a purely ionic and covalent bond, respectively. For the trimer from Eq. (3.4), the bond orders are $B_{12} = B_{12} = 1/2$, and $B_{13} = 1/4$, whether the number of the bonding MO's is one or two. We thus conclude that the bond order defined in Eq. (3.5) reflects, to some extent, the deviation of the bonding in Fig. 3.1 from a collection of two-center bonds, since $1/2 + 1/2 + 1/4 = 1.25 > 1$.

To gain additional insight, one may quantify the bonding conribution of an individual LMO, j, by evaluating the expectation value of the density matrix for the orbital, see "Localization Theory" in the online MOPAC Manual [96]

$$\widetilde{B}_{jj} \equiv \left\langle \chi_j | \widehat{P} | \chi_j \right\rangle = 2 \sum_{\lambda\mu} C_{\lambda j} C_{\mu j} P_{\lambda\mu}, \tag{3.8}$$

where in the sum above, terms pertaining to the same atom are excluded. The bonding contribution for a lone pair is automtically 0. For a two-center bond $\chi = \psi = \alpha\phi_1 + \beta\phi_2$, $\widetilde{B} = 8\alpha^2(1-\alpha^2)$, which is simply the Wiberg bond index times two. Likewise, the trimer from Eq. (3.4) in the one-LMO arrangement yields $\widetilde{B} = 2.5$, The two-LMO arrangement leads to $\widetilde{B}_{11} = \widetilde{B}_{22} = 1.25$, so that the total bond contribution is, again, 2.5. Thus based on the bond index and bond contribution analysis, the bond order for the Hückel trimer is not sensitive to whether MO2 is regarded as bonding on non-bonding. We shall see that the two analyses give different results in more complicated situations.

3.4 Symmetry breaking in the bond assignments in small molecules with directed interactions

This Section focuses on hydrogen-passivated trimers AsH_2-AsH-AsH_2 and AsH_2-AsH_2-AsH_2. Both are held together by a 3-center, $pp\sigma$ bond, see Fig. 3.2. Provided each arsenic carries a lone pair, the 3-center bond has four and three electrons for the former and latter molecule, respectively; we will refer to those as the 3/4 and 3/3 case for brevity. The actual populations of the lone pairs and the $pp\sigma$ bond, if any, depend on the As-As bond length, as we will see shortly. The 3/4 molecule satisfies the Lewis quartet rule, while the 3/3 counterpart is technically hypervalent.

We will study configurations of these molecules other than the ground state. The motivations are multifold. On the one hand, small trimeric motifs that contain

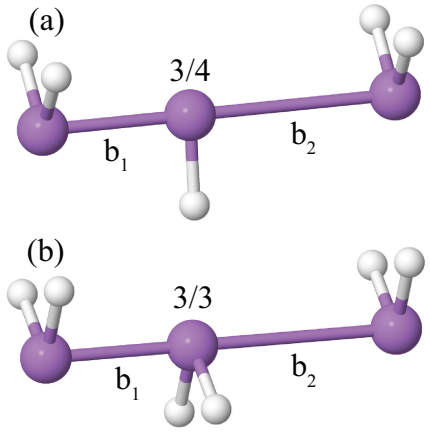

Figure 3.2: The trimers AsH_2-AsH-AsH_2 (panel (a)) and AsH_2-AsH_2-AsH_2 (panel (b)), corresponding to 3-center/4-electron and 3-center/3-electron $pp\sigma$ bond. In all figures below except Figs. 3.3, 3.4, and 3.9, $b_1 = b_2$.

semimetals exhibit a remarkably broad, continuous range of bonding behaviors—from weak seconary to true covalent—when incorporated in a solid matrix, [1] as mentioned in the Introduction. Small motifs isoelectronic with those arsenic trimers serve as building blocks for a variety of chalcogenide alloys that exhibit distorted octahedral coordination and a complex diversity of structures even for chemically similar stoichiometries. [9] For instance, chalcogens exhibit from 2 to 6 nearest neighbors in di-pnictogen tri-chalcogenides, the number positively correlated with atomic mass. [4] Finally, a linear arsenic trimer is a minimal molecular model for the puzzling midgap states observed in amorphous chalcogenides. [8, 10]

The energy of the 3/4 molecule is shown in Fig. 3.3 as a function of the distance between the terminal arsenics and the location of the middle arsenic. All three arsenics are forced to be on one straight line; the restriction to be elaborated on later. We observe that in the ground state, the As-As bonds are equal in length.

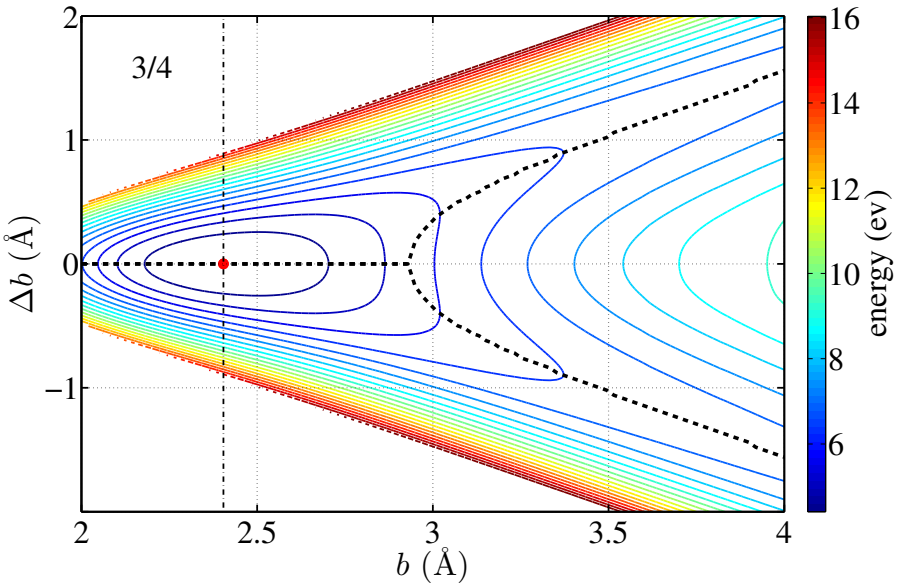

Figure 3.3: The contour plot of the potential energy of the 3/4 trimer, Fig. 3.2(a), as a function of the trimer length per bond $b \equiv (b_1 + b_2)/2$ and the distance of the center arsenic from the midpoint between the terminal arsenics, $\Delta b \equiv (b_1 - b_2)/2$. The stable, symmetric state is marked by the filled red circle, the corresponding equilibrium trimer length is indicated by a thin vertical dashed line. The dashed, bifurcating graph shows the minimum energy at fixed value of b.

Upon stretching the trimer, this symmety must be broken, since the middle arsenic must choose a neighbor: A bond, no matter how weak, is better than no bond. By construction the lengths of the shorter and longer bonds are denoted as b_1 and b_2. The symmetry breaking is seen directly in the fork-like shape of the "trough" on the potential surface in Fig. 3.3; the (bifurcating) bottom is shown with the solid line. The calculations are performed using the PM6 parametrization of the semi-empirical package MOPAC [40, 95, 97, 98] and have been validated using the ab initio package NWChem. [41]

The dependences of the lengths of the short and long bonds on the total trimer

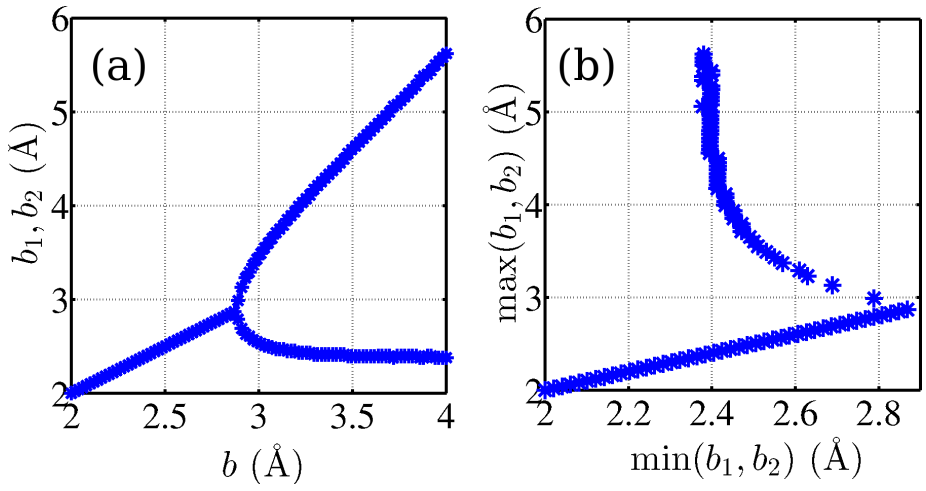

Figure 3.4: The eqilibrium values of the As-As bond lengths for a fixed value of the overal trimer length, according to the dashed line on Fig. 3.3; **(a)** as functions of the trimer length per bond, **(b)** plotted parametrically, for the longer bond vs. the shorter bond.

length $(b_1 + b_2)$ are shown in Fig. 3.4(a). The latter dependence can be also plotted parametrically, b_1 vs. b_2, as in Fig. 3.4(b). The latter graph may be compared with the Landrum-Hoffman scatter plots for a large number of trimeric units. [1]

As already mentioned, one may associate the symmetry breaking with regard to the bond *strength* between neighboring arsenics with the spatial symmetry breaking $b_2 \neq b_1$, at least for sufficiently large values of $|b_2 - b_1|$. This phenomenon is discussed in great detail elsewhere. [94] Here, in contrast, we *prevent* the breaking of the $b_1 \leftrightarrow b_2$ symmetry by imposing an artificial constraint $b_1 = b_2$ for *all* values of the trimer length. At the same time, we constrain the hydrogens so that the molecule has two symmetry planes, one containing the 3-center bond and the other—call it plane R—perpendicular to the bond and containing the middle arsenic. Each MO must be either even or odd with respect to the reflection in plane R.

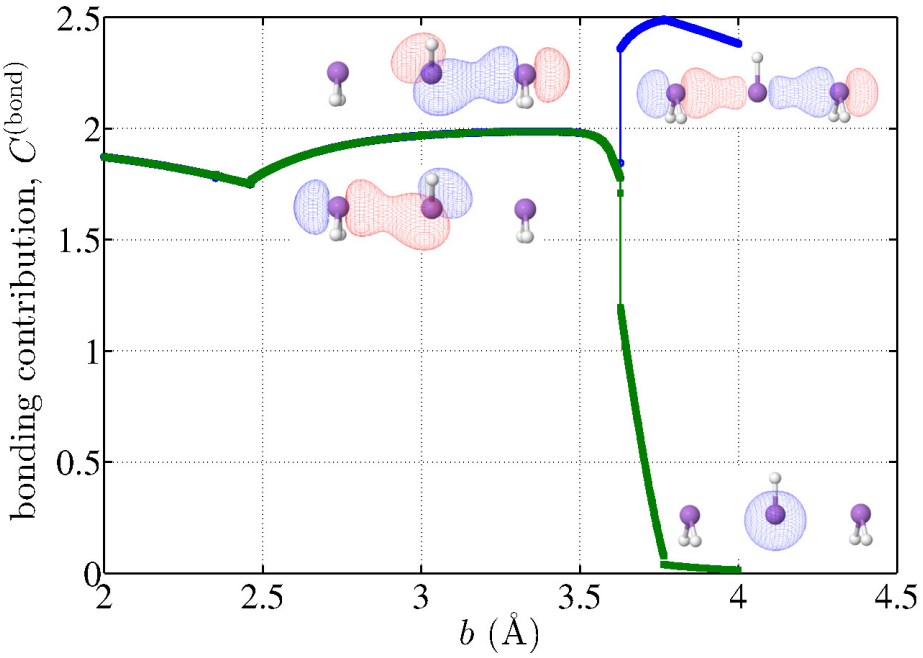

Figure 3.5: The bonding contribution of the LMOs as functions of the As-As bond length $b = b_1 = b_2$, for the 3/4 case.

We find that within a remarkably broad range of the inter-arsenic distance the bond characteristics are essentially the same as those in the ground state of the trimer. First off, we identify the localized molecular orbitals (LMOs) that are associated with the As-As-As subsystem, as opposed to the As-H bonds. There are two such LMOs. Their bond contributions, Eq. (3.8), are shown in Fig. 3.5 as functions of the trimer-length. In that same figure, we display the corresponding localized molecular orbitals. The corresponding bond-center number (3.1) and Wiberg bond index (3.5) are shown in Fig. 3.6(a) and (b) respectively.

The bond order eventually changes, at sufficiently low densities, and does so in a very abrupt fashion, especially the bond contribution, which transitions within a mere 0.04 Å. The transition in the bond type is apparently accompanied by a symmetry

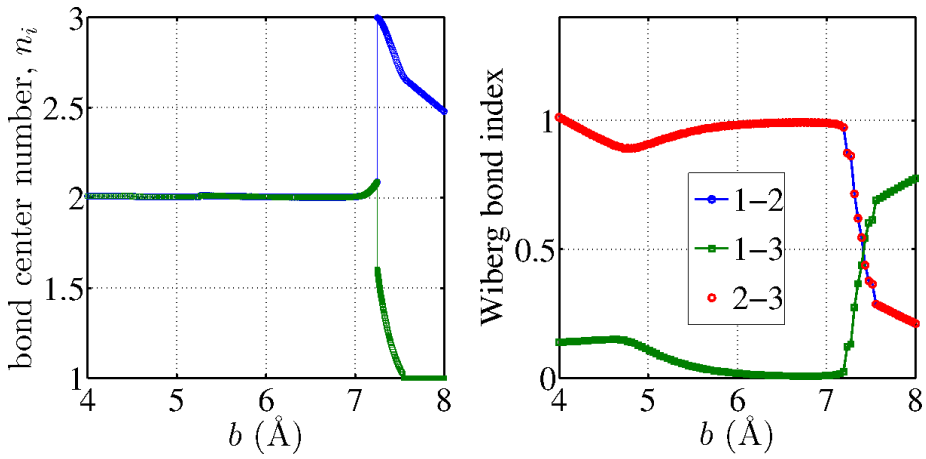

Figure 3.6: We display, as functions of the As-As bond length $b = b_1 = b_2$: **(a)**, the bond center number for the LMOs from Fig. 3.5; **(b)**, the Wiber bond index. Note the latter is computed using the density matrix and does not rely on the localization procedure.

change in the LMO; the symmetry change is strictly discrete, of course. On the high density side, the LMOs are mirror images of each other and amount to the same bond contribution. On the low density side, both LMOs are even functions with regard to the reflection in plane R. One LMO stretches over the three centers, consistent with its bond-center number and the bond contribution, while the other LMO is essentially a lone pair. It may seem questionable to interpret the two apparent As-As bonds as actual bonds just on the high-density side of the transition. After all, the bond length, ~ 3.6 Å, is about 50% longer than its equilibrium value and, in fact, is more appropriate for a closed-shell, secondary interaction. [9] Note, however, the interaction is *not* closed-shell, since the formally antibonding orbital in the $pp\sigma$ bond, see Fig. 3.1(a), is vacant. The effect of the large bond length is that the cohesive interaction is weak despite formally conforming to the conventional definition of a bond. In any event, we have confirmed the symmetry breaking transition using a

higher end approximation, see Appendix for details.

We first test for the (remote) possibility that *canonical* molecular orbitals experience abrupt changes, which, in turn, cause similarly abrupt changes in the localized molecular orbitals. Already a small molecule such as the AsH_2-AsH-AsH_2 has very many molecular orbitals. Specifically, at the MOPAC level, each arsenic has three orbitals per atoms ($4s$, p, and d) and each hydrogen has one, that make a meaningful contribution to the MOs. Plotting such a large number of molecular terms, as functions of density, is hardly illuminating. Instead, we make two scatter plots, Fig. 3.7(a) and (b), in which we show the *change* in the expansion coefficients C and $\widetilde{C}$ from Eqs. (3.3) and (3.7) across the transition vs. their arithmetic average. The two sampling points are indicated in Fig. 3.5. According to these scatter plots, the changes in the MO expansion coefficients $\widetilde{C}$ are gradual; these changes are commensurate with the magnitude of the change in the bond length. In contrast, the coefficients C of the LMO expansion change dramatically. One can thus rule out the possibility that the rapid change in the bond assignment is caused by an electronic transition such as term-crossing, consistent with the results of direct inspection of the molecular terms.

Because the MO coefficients change only very little accross the transition, we must look at their evolution within a relatively broad range of density changes, to determine the underlying cause of the symmetry-breaking transition. Consistent with the simple discussion in Section 3.3 and the expectation based on the apparent changes in the LMO during the transition, we conclude that the eventual appearance of a fully symmetric, three-center LMO, upon dilation, stems from a sequestration of

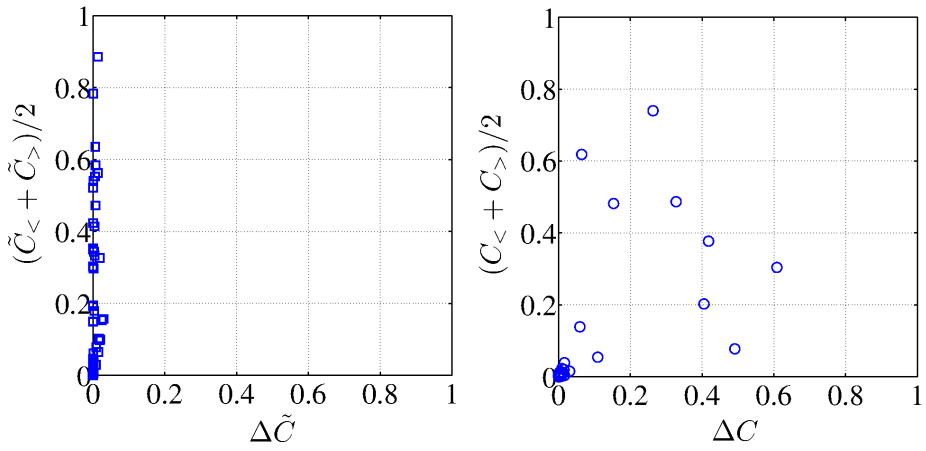

Figure 3.7: Scatter plots of the changes in the expansion coefficients of the MOs, **(a)**, and LMOs, **(b)**, upon the symmetry breaking transition in Fig. 3.5, vs. their average values.

the electons from the $pp\sigma$ bond to the lone pair on the central arsenic, see Fig. 3.8. Physically, this occurs because the Coulomb energy within the inter-atomic space decreases with inter-atomic separation.

These conclusions are supported by analysis of the 3/3 case AsH_2-AsH_2-AsH_2, which is of interest in its own right. The analysis is graphically summarized in Figs. 3.9-3.11. These calculations have been performed at the restricted open-shell Hartree-Fock (ROHF) level. In contrast with the 3/4 case, the 3/3 molecule is only metastable and readily decays into a dimer AsH_2-AsH_2 (which does obey the octet rule) and a monomer AsH_2. The reason is that the $pp\sigma$ bond is one electron short (even though the overall bond is hypervalent). Nevertheless, the molecule is symmetric in its metastable minimum, where it exhibits the bond length and LMO characteristics similar to those of the 3/4 trimer near its ground state. One must be mindful that the metastable minimum could disappear at a higher level of

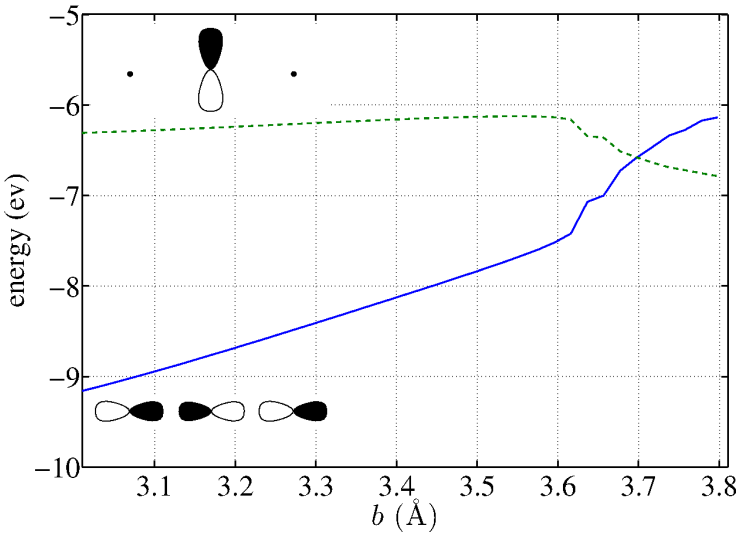

Figure 3.8: The energies of the MOs responsible for the $pp\sigma$ bond and the lone pair on the central arsenic, as functions of the As-As bond length $b = b_1 = b_2$, for the 3/4 case.

approximation. In addition, the present, MOPAC-based LMO analysis of the 3/3 case has the limitation that only the *filled* orbitals are used for constructing the LMOs. Aside from these potential limitations, we observe that bringing the nuclei together induces sufficient amount of electron transfer from the lone pair on the central arsenic to fill the $pp\sigma$ bond, as is witnessed by the formation of two two-center LMOs. The resulting cohesive interaction is still weaker than in the 3/4 case in that it amounts only to a *meta*stable minimum. Interestingly, the Wiberg bond index exhibits no singularity at the transition thus revealing a significant distinction between localization-based techniques for indentifying bonds and direct analyses of the density matrix. Incidentally, we note that the relatively mild dependence of the bond index on the nuclear coordinates, both in Figs. 3.11(b) and 3.11(b), indicates that the insensitivity of the LMO-based quantities to bond deformation is not an

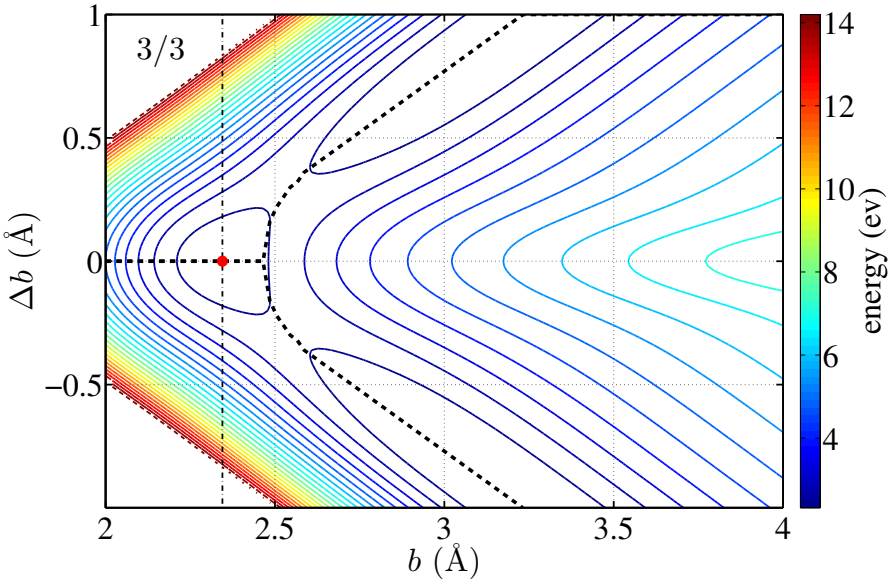

Figure 3.9: The contour plot of the potential energy of the 3/3 trimer, Fig. 3.2(a), as a function of the trimer length per bond $b \equiv (b_1 + b_2)/2$ and the distance of the center arsenic from the midpoint between the terminal arsenics, $\Delta b \equiv (b_1 - b_2)/2$. The metastable symmetric configuration is marked by the filled red circle. The dashed, bifurcating graph shows the minimum energy at fixed value of b.

artifact of neglecting overlap between atomic orbitals on distinct centers.

In both 3/4 and 3/3 case, we observe that a stable (or metastable) three center bond is signalled by the presence of two *two*-center LMOs. One may formulate this in the form of a general rule: In a stable (or metastable) molecule, the bonding LMOs should be two-center and cover each bond. Conversely, when the molecule is not fully covered by two-center LMOs, the molecule is subject to a structural instability. This is true even if the molecule is fully covered by LMOs so long as the latter localized orbitals span three or more centers. One may benefit from further illustration of these notions by considering the familiar example of the benzene molecule, see Fig. 3.12. Here we observe that of the 18 available valence electrons, 12 fill the σ bonded

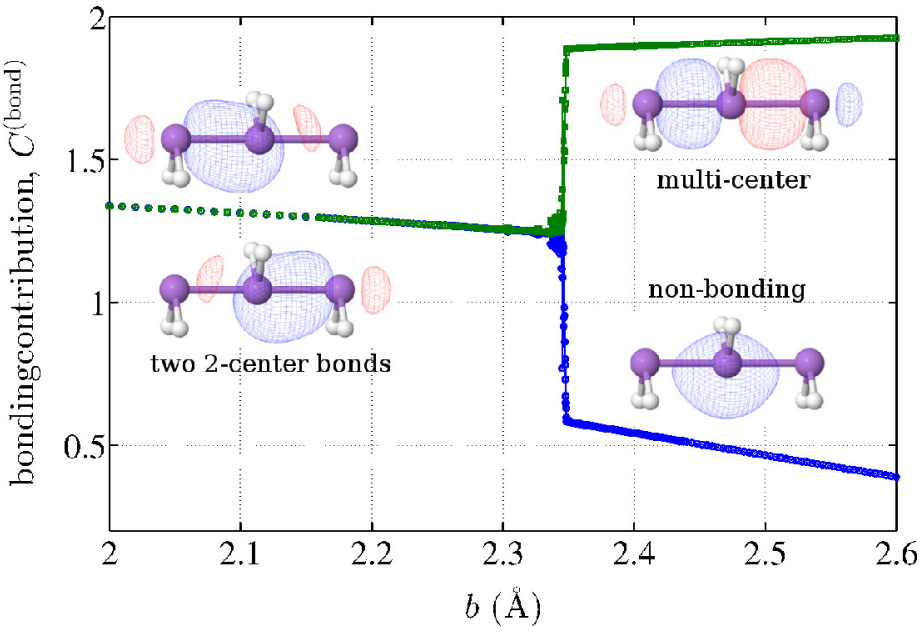

Figure 3.10: The bonding contribution of the LMOs as functions of the As-As bond length $b = b_1 = b_2$, for the 3/3 molecule.

network, leading to a formation of 6 two-center LMOs. The remaining six electrons amount to three non-two-center LMO, which by themselves imply an instability. The instability is second order Jahn-Teller, and a finite-size analog of the Peierls instability. [25,42] The benzene molecule can be thought of as a superposition of the bonding situations on the opposite sides of the transition shown in Fig. 3.5. The amount of instability stemming from the non-bonding LMOs is however unsufficient to break the spatial symmetry, consistent with more sophisticated analyses; [25] benzene thus retains the six-fold, not three-fold symmetry in its ground state.

We finish the Section by briefly discussing the low-density side of the transition in the trimer. Formally, the delocalization of the LMO—so as to span nearly three centers—can be traced to the relatively small amount of charge contained within the

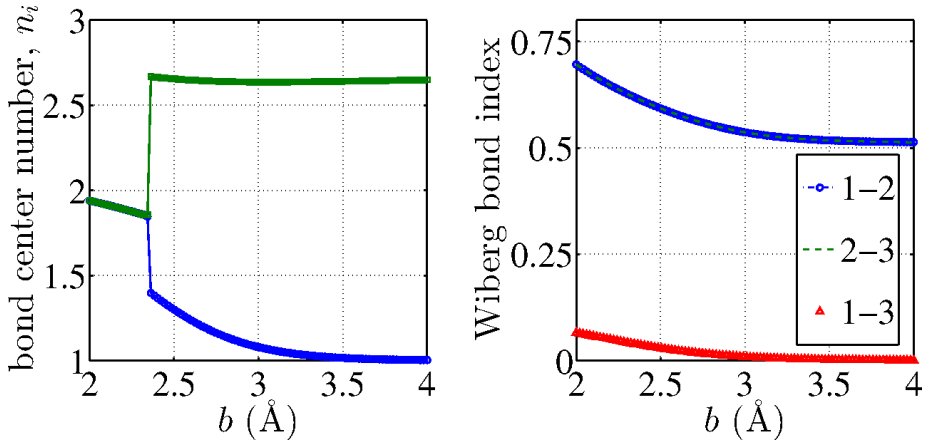

Figure 3.11: We display, as functions of the As-As bond length $b = b_1 = b_2$: **(a)**, the bond center number for the LMOs from Fig. 3.10; **(b)**, the Wiber bond index. Note the latter is computed using the density matrix and does not rely on the localization procedure.

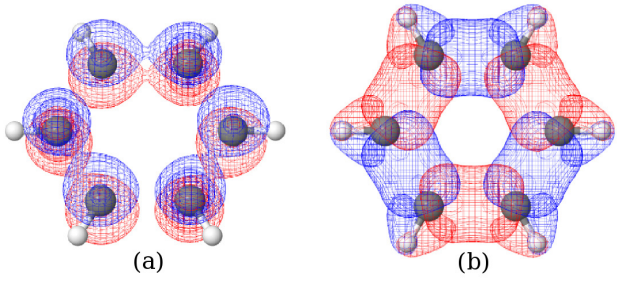

Figure 3.12: The localized molecular orbitals for the ground state of benzene.

interatomic space

3.5 Bond assignment in a solid

We begin discussion of bonding in a solid by noting that the 3/4 trimer is unique in that it is the only case, in which the n-center, $(n+1)$ electron bond is actually stable. This can be understood by using the 2-center rule from the Section 3.4. By that rule,

an n-center, $(n+1)$ electron bond is stable if there are enough electrons to fill $(n-1)$ LMOs, i.e., $n+1 = 2(n-1)$. (This is assuming there is no electron transfer from lone pairs, and other sub-bands as in the benzene example above.) The equation is solved only by $n = 3$, while the σ system becomes electron deficient for any molecule longer than 3 centers. In the $n \to \infty$ limit, one obtains one electron per bond; a $(AsH_2)_n$ chain will dimerize, if let go, [9] owing to a Peierls instability. [25, 53, 54] As in the above discussion, we prevent this spatial symmetry breaking from occuring. When bonding electrons are in deficit, either multi-center LMOs arise, or the LMOs remain two-center, but no longer cover the molecule.

To test for these possibilities, we analyze two artificial, ring-like molecules $(AsH_2)_n$, $n = 20, 24$. These specific ring lengths are chosen using the following logic. The number of AsH_2 monomers is even to prevent the midgap state [8, 10] and is sufficiently large to minimize effects of *sp*-mixing and the finite curvature of the chain. Making the chain circular prevents symmetry lowering associated with having open ends. Finally, using specific values 20 and 24 allows one to test for effects of changing the order of rotational symmetry. Incidentally, the hydrogens will be fixed to maintain the symmetry; whatever symmetry breaking that may take place in the LMOs thus would not stem from symmetry breaking at the MO level, but, rather, from localization of the orbitals.

As in the trimer case, we observe that at sufficiently high densities, the LMOs are two-center and cover every bond, see Fig. 3.13. In distinction from the trimer and benzene, the LMOs are not strictly equivalent, even if similar in shape and other characteristics. There are two distinct types of LMOs that alternate along the

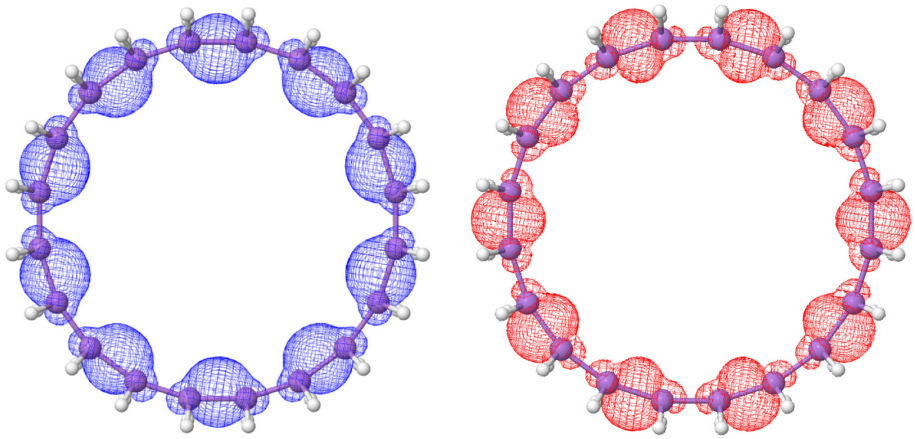

Figure 3.13: The localized molecular orbitals on the $(AsH_2)_{20}$ ring molecule shown for clarity as two sets. Within each set, the orbitals are equivalent. The density is apprently sufficiently high so that each two-center $pp\sigma$ bond is filled; $b = 2.48\mathring{A}$, bond index = 1.97.

chain, implying the localized orbitals form a pattern that is of lower symmetry than the underlying molecule, D_{10} and D_{20} respectively. It is clear from Fig. 3.13 that this symmetry lowering helps decrease the Coulomb repulsion between neighboring LMOs. Now, upon sufficient dilation, the lone pairs on the arsenics become populated, while the $pp\sigma$ system is only half-filled. The resulting LMOs are two-center, in contrast with the trimer, and fill every *other* bond. Not only does the resulting alternation pattern have a ten-fold symmetry, which is lower the the twenty-fold symmetry of the molecule, it also turns out to break the *chiral* symmetry, see Fig. 3.14. Finally note that according to Figs. 3.13 and 3.14, the solution to the localization procedure is not unique (two and four distinct solutions respectively), however the distinct solutions are physically equivalent.

The ground state of the ring is clearly a set of weakly interacting dimers, implying the D_{20}-symmetric molecule is unstable. Still, the ring has a metastable

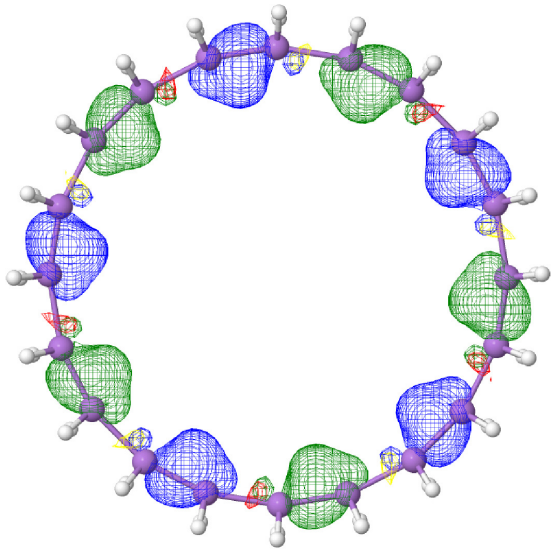

Figure 3.14: The localized molecular orbitals on the $(AsH_2)_{20}$ at a lower density. The bond length $b = 2.57$, bond index $= 1.98$.

D_{20}-symmetric minimum at sufficiently high densities, as can be directly seen by computing the energy as a function of the degree of the dimerization. This finding supports the two-center rule suggested in Section 3.4.

As a final example of quasi-one dimensional systems, we present the LMOs of a 24-member ring, approximately at half-filling of the $pp\sigma$ band. When the hydrogens are fixed so that the molecule is D_{24}-symmetric, the LMOs form a pattern with a lower, D_{12} symmetry, see Fig. 3.15(a); the pattern preserves the chiral symmetry, in contrast with the 20-member ring in Fig. 3.14. If, however, the hydrogens are allowed to relax, one recovers a yet lower symmetry, D_2 pattern, Fig. 3.15(b), which does break the chiral symmetry *locally*. Note the hydrogens adopt an alternation pattern.

The interesting linear and ring molecule examples share a common electron count,

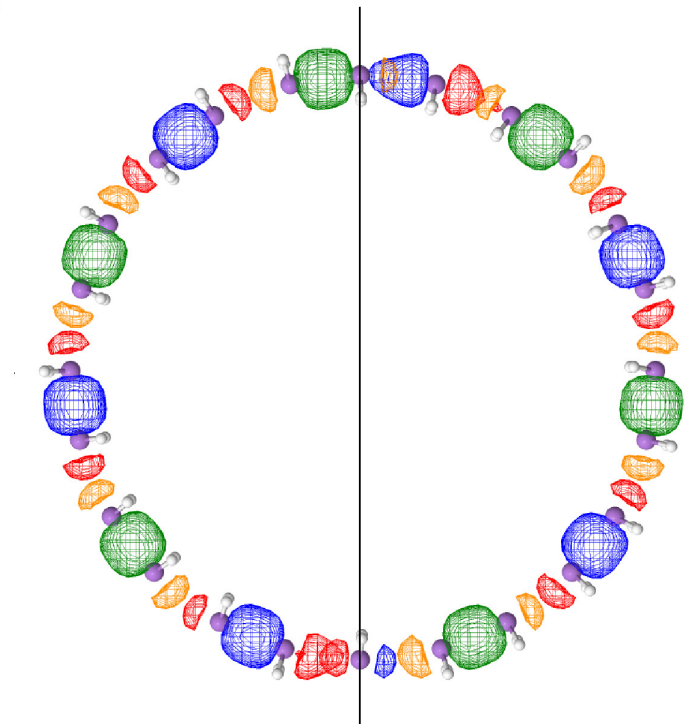

Figure 3.15: The LMOs for the 24-member ring $(AsH_2)_{24}$. $b = 3.46\mathring{A}$, bond index = 1.98

a single p σ bond orbital per center. An arsenic solid can also be included in this group if we think of it as composed of intersecting linear chains. Although there are three p orbitals on each center, $pp\sigma$ bonds along each direction make use of a single orbital per atom. By compressing a symmetric cubic lattice we expect to modify the $pp\sigma$ electron count through promotion out of the 4s lone pair states. At sufficiently high density, chains along one or more directions could have uniform two-center bond assignments, then as density is reduced only a fraction of these localized bond orbitals will retain their two-center bond order. Symmetry breaks as the system chooses where to place the two-center bonds, and how to align the strong/weak orientation of the remaining multi-center orbitals. For simplicity we restrict our examination

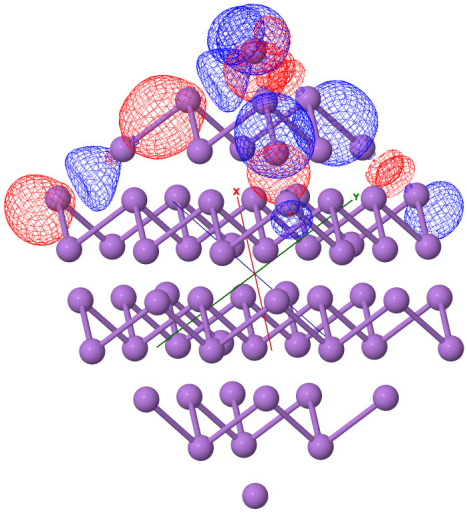

Figure 3.16: 64 atom cubic arsenic sample at reduced density showing single chains of localized orbitals along each axis to illustrate how bond assignments in the lattice form a pattern suggestive of rhombohedral geometry

of solids to low densities where symmetry is broken. Reducing density on a simple cubic arsenic solid results in a fully dimerized two-center bond pattern along all three axes, often described as a 3D Peierls distortion [57]. Out of the total set localized bond orbitals we show a single chain along each axis so that two-center bond and multicenter orientations are clearly visible. The lattice structure has been edited to show links between sites only where a two-center bond is located. The graphic result in Fig. 3.16 bears strong resemblance to the rhombohedral structure of arsenic. The easiest way to relate the system of alternating dimerized chains to the notional rhombohedral structure we have drawn is to take the chains along each axis one layer at at time like Fig. 3.17. Here a clear pattern of alternating two-center/weak bonds is visible, by systematically deleting the connections corresponding with weak bonds you end up with a system of double layers $\perp$ to the [111] direction.

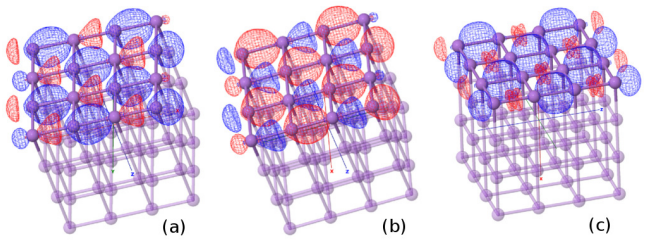

Figure 3.17: 64 atom cubic arsenic sample at reduced density showing plane layers of localized bonding orbitals. Frames (a) and (b) show X and Y plane 3 center bond layers respectively. 2-center Z plane shown in (c).

Fig. 3.16 (c) shows a single Z-plane layer worth of two-center bond assignments in a 64 atom cubic arsenic solid. In this cubic solid example with essentially a three electron per atom valence count at the density shown, the two-center bonds play a different role when it comes to multiplicity of bonding arrangements compared to their molecular cousins. The staggered alternation pattern of two-center bonds illustrated by the single layer in Fig. 3.16 support the formation of the double layers perpendicular to the [111] direction visible in Fig. 3.16. Once symmmetry is broken and two-center bond assignment is established, double layers are essential to the localized solution that minimizes the overlap between distinct orbitals. There is no entropy associated with these bond assignments, they are effectively a constraint associated with the localized solution. Two degrees of freedom are constrained by these double layer planes, that leaves the potential for multiplicity along the remaining free direction.

A perfect alternation pattern in this direction leads to the previously discussed localized electron density picture resembling rhombohedral arsenic, but arsenic also has a metastable black phosphorus phase, so we might expect a bond arrangement

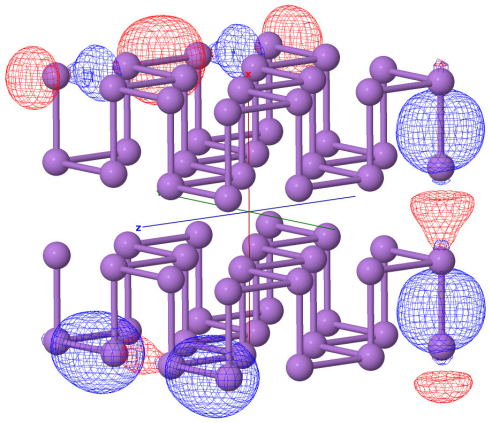

Figure 3.18: simple cubic lattice with bond connections edited to match metastable black phosphorus structure, a single example of chain localized bond pattern shown for each axis is shown for clarity

representative of this structure to coexist with that shown in Fig. 3.16. If rather than alternating, the bond patterns along the free direction (in this case X) have the identical registration shown in Fig. 3.18 the overall localized bond pattern looks similar to the geometry of black phosphorus.

These two broken symmetries only represent two states, for any significant amount of degeneracy, each individual chain should be free to choose it's own registration, as the difference between what we have called the rhombohedral and black phosphorus configurations is just a shift by one cubic lattice spacing. This type of freedom would give multiplicity that scales with the number of X oriented chains (surface area). Like it's crystalline geometry counterpart our black phosphorus bond pattern is metastable compared to the rhombohedral pattern, it's much easier to shift a single X oriented chain here than it is to disturb the rhombohedral configuration. In Fig. 3.19 we show a single shifted X oriented chain, the fact this single odd chain

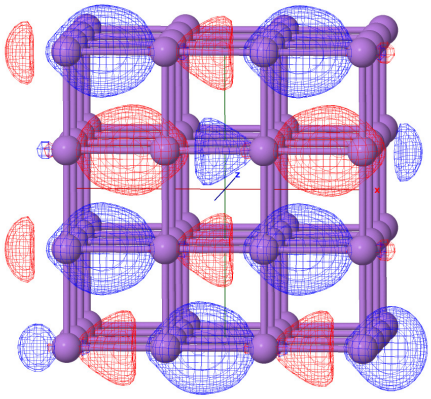

Figure 3.19: a single plane layer of X oriented chains showing the coexistence of a single odd configuration amongst what was formerly a uniformly aligned set forming the black phosphorus type bond pattern.

coexists with the remaining black phosphorus aligned chains suggests that some amount of disruption of the double layer is tolerable. It's unlikely that all possible combinations of X chain registration are tolerable localization-wise, but even half of the combinations represents significant degeneracy in a solid.

3.6 Discussion

This work exploits a formal similarity between making/breaking a chemical bond and discontinuous phase transitions. That bonding strength should change in a rapid, sigmoidal fashion can be ultimately traced to the discrete nature of electric charge. In contrast, there seem to be a *variety* of reasons for a phase transition to be first order. A prominent example is density-driven liquid-to-solid transitions, [7] during which particles become localized around fixed positions in space thus breaking the translational invariance of the particle density distribution. The symmetry breaking

is somewhat less dramatic for periodic solids, which maintain symmetry with respect to a subset of translations and point symmetries.

Similarly, here we find that there are symmetry changes that can take place in a molecule and solid alike when charge is redistributed among bonds. Of course, such charge redistribution is expected when the spatial symmetry of the molecule is broken as in Fig. 3.4: Because of the Coulomb attraction between electrons and nuclei, the former tend to preferentially occupy space between closer spaced nuclei. However, when such spatial symmetry breaking is avoided, charge redistribution becomes subtler. At any value of the density, the molecular orbitals retain the symmetry of the molecule itself. We have seen that it is *effective* wave-functions of the bonding electrons that undergo symmetry change, the latter being density-driven. These effective wave-functions are found through a well-known localization procedure, which itself, interestingly, originates in early attempts to single out bonding electrons based on the symmetry of the molecule. In essence, the localization technique consistst of finding a set of orthonormal wavefunctions that exhibit least mutual repulsion. The so determined localized molecular orbitals (LMOs) that are represented prominently in the inter-atomic space are regarded as bonding; their symmetry is generally lower than that of the molecule. We find that in a stable or metastable state, each putative two-center bond should be populated by a two-center localized orbital. Conversely, incomplete coverage of the putative two-center bonds by two-center LMOs implies a structural instability: If let geometrically optimize, the putative molecule will dissociate. Somewhat surprisingly, we find that the presence of a *three*-center LMO implies that the corresponding three-center bond is too weak to hold the molecule

together. The explanation is that the three-center LMO arises together with a *lone pair*, the two orbitals being low-density relics of two two-center LMOs. The electrons comprising the lone pair no longer participate in the bond.

The expansion coefficients of canonical molecular orbitals, in terms of the atomic orbitals, change gradually with bond deformation. In contrast, the expansion coeffients for the localized orbitals and the bond participation are found to change in an aproximately discrete fashion while staying near stationary between changes. As such, the localization formalism can be used to assign bonds unambiguously within broad ranges of inter-atomic separation. This robustness of the LMO analysis is probably due to the success of the localization technique in keeping the LMOs apart even relatively high densities, both nuclear and electronic. Once the localization "fails," it does so in a discrete, phase-transition like fashion. Needless to say, the accompanying symmetry change of the LMOs is something that is intrinsically discrete. We have found that the symmetries of the LMOs are lower than those of the underlying molecule, but not necessarily much lower. Furthermore, the alternative sets of LMOs are found to be physically equivalent. It is interesting whether the localization procedure could be truly ambiguous, see the Burdett comment in the Introduction. The continuum, classical treatment of Coulombic systems, due to Schmalian and Wolynes, [84] suggests that the answer is yes; the resulting bonds could organize into a multitude of alternative, disordered stripe patterns. This is a subject of future studies.

Both the symmetry and the *shape* of the LMOs change when the character of the bond change. These shape changes afford one a great deal of physical insight. For

instance, the breaking of a three-center/four-electron bond can be directly traced to electron transfer from the three-center bond to a lone pair on one of the atoms, as already mentioned. Detecting the transfer using the localized orbitals is far more convenient than with the canonical MOs, because, again, the localized wavefunction switches in a discrete fashion.

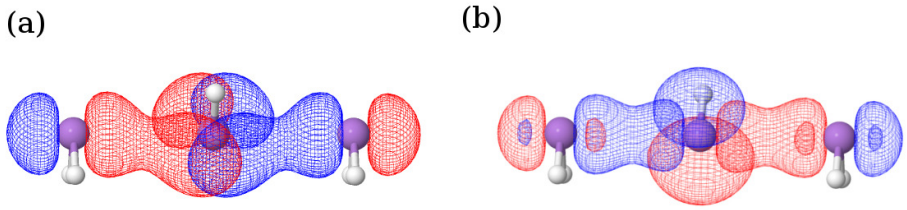

Figure 3.20: LMO linear combinations at high density (a) and low density (b).

To summarize, the discrete nature of the chemical bond can be ultimately traced to symmetry considerations, even if the molecule in question does not show any obvious symmetries. The symmetry changes are of two types: One is the localization of the effective wavefunctions of the bonding electrons, which is analogous to density-driven particle localization during liquid-to-solid transition. For molecules possessing point symmetries, individual localized orbitals may no longer possess those symmetries, but their linear combintations still may, see Fig. 3.20. Furthermore, the LMO analysis appears to be capable of identifying putative bonds even in geometries that are very far from the stable geometry. This suggests a way to efficiently screen very large quantities of candidate compounds for stability and possible isomers. In this procedure, a computer first generates a variety of structures, subject only to steric

constraints. In the next step, a computationally efficient, semi-empirical approximation is used to obtain the molecular orbitals, after which the localized molecular orbitals are generated. (Both functionalities are already implemented in MOPAC, for instance.) If the two-center LMOs happen to cover inter-atomic spaces within a sufficiently large fraction of nearest neighbors, the candidate compound and structure are rated as a high probability target. Such targets are then subjected to more sophisticated, computationally intense screening. The candidate compounds may be generated subject to preset constraints of interest in specific applications, such as the design of a docking site for a given ligand.

Chapter 4

Degenerate charge density waves: miscibility of localized and metallic states

4.1 Overview

We use a tight-binding approximation to show that miscibility or lack thereof is tied to the degree of mismatch between the charge-density-wave (CDW) patterns in the species involved, the mismatch being in the degree of electron localization and symmetry. We further show that the chemical moieties in contact can be treated analogously to two distinct phases of the same molecular species and build the corresponding density functional; the solvation penalty can thus be viewed as the interface tension between distinct thermodynamic phases. The present microscopic

picture yields self-consistently that when the phase with more localized electrons is sufficiently less polarizable than the other phase, the two phases are separated by a discontinuous transition and thus mix poorly, similarly to oil and water. We argue that the metal-insulator transition is usually discontinuous, by analogy with the liquid-to-solid transition; there are however exceptions when the underlying lattice possesses a special symmetry. This symmetry-based mechanism complements the exciton-condensation mechanism discussed earlier by Mott and others.

4.2 Motivation

Consider the following basic notions: On the one hand, metallic and insulating phases are associated with delocalized and localized electrons, the former and latter corresponding, respectively, to differing degrees of translational symmetry breaking. Whenever the metal-to-insulator transition is discontinuous, an interface between the two phases should incur a free energy cost with an explicit electronic contribution. On the other hand, the liquid-to-solid transition in classical liquids *also* corresponds with a lowering of translational symmetry. The transition is always discontinuous; [7] the interface between the coexisting phases automatically incurs free energy cost; the electrons enter only implicitly, through the classical force fields.

Here we attempt to treat on the same footing the coexistence of delocalized and localized electrons—which must be generally described quantum-mechanically—and the analogous coexistence in classical systems. Both can be described in the language

of charge-density waves (CDWs), the formal difference between quantum and classical cases being that the density-matrix for the latter is strictly diagonal. Quantum-mechanical effects at interfaces can be addressed already using simple tight-binding models. Moreover, the energy cost or gain at the interface, *per unit area*, can be quantified using one-dimensional tight-binding models. The latter turn out be a continuum description of another common phenomenon involving interfacial phenomena, namely, solvation. A very important yet traditionally undertaught topic, solvation of modestly-sized molecules and ions has been extensively modelled using hybrid quantum-mechanical/classical methodologies. [99–101] Here we argue that solvation can be described in simple terms and is of much more general nature that might be inferred from the seminal Born theory of charge solvation in polarizable medium. [60] This is analogous to how the molecular orbital theory demonstrates the quantum-mechanical nature of bonding irrespective of the detailed nature of the physical forces. We find, in Section 4.3, that the degree of mutual miscibility can be traced to the degree of similarity between the charge density waves in the bulk of the substances brought to contact.

Expressed originally in terms of molecular fields, the above notions can be profitably recast in terms of their conjugate variables, along the lines of the venerable density functional theory. [5, 102] Coulomb interactions and polarization can be straightforwardly incorporated at a meanfield level thus allowing one to address the metal-insulator transition using the Landau-Ginzburg functional. Hereby a natural connection emerges with the known phenomenon of poor miscibility of substances with distinct polarizabilities, such as oil and water. Also in Section 4.4, we observe

that the density functional theory affords one a symmetry-based perspective on the metal-insulator transition (MIT). The latter is argued to be discontinuous, unless the insulator is a periodic crystal whose lattice has the special property of consisting of two equivalent, mutually-complementary lattices. In the latter case, the transition may still be continuous, despite the preemptive formation of exciton pairs argued a long time ago by Mott to always render the MIT discontinuous. We observe that in contrast with the classical DFT, which makes do with the density as its order parameter, its quantum mechanical counterpart requires in the least a two-component order parameter.

4.3 A simple quantum mechanical model of solvation

Consider the following Hückel energy function for a one-dimensional N-membered chain, one orbital per site:

$$\begin{aligned} \mathcal{H}(N,t,t_0,\varepsilon) &= \sum_{n}^{N} \sum_{s=\pm 1/2} \Big[-t_{n,n+1} \left(c_{n,s}^{\dagger} c_{n+1,s} + c_{n+1,s}^{\dagger} c_{n,s} \right) \\ &+ (-1)^n \varepsilon \, c_{n,s}^{\dagger} c_{n,s} \Big] , \end{aligned} \tag{4.1}$$

where $c_{n,s}^{\dagger}$ ($c_{n,s}$) creates (annihilates) an electron on site n with spin s,

$$t_{n,n+1} \equiv \bar{t} + (-1)^n t, \quad |t| \leq \bar{t} \tag{4.2}$$

is the hopping matrix element between sites n and $n+1$, and $(-1)^n \varepsilon$ the on-site energy. By construction, the system is at half-filling. Note that non-zero values of

ε and t result in a charge-density wave (CDW) with a repeat unit containing two sites. A non-vanishing ε corresponds to charge alternation between sites proper, while non-zero t will cause charge alternation between the *inter*-site spaces. To distinguish between the two, we will sometimes use notation the "on-site" and "off-site" CDW, respectively. The off-site wave is often called the "bond-order" wave (BOW). We remind the reader that one-dimensional systems at half-filling are intrinsically unstable toward dimerization and, consequently, becoming insulators [53, 54] unless the electronegativity variation ε exceeds a certain threshold value comparable to $\bar{t}$, [51, 52] in which case the chain becomes an ionic insulator.

We will denote the ground state energy corresponding to the Hamiltonian (4.1) as $E(N, t, \bar{t}, \varepsilon)$. We shall also consider compound systems, in which *two* chains with generally distinct values of the parameters t, ε, and N are joined. In such cases, the ground state energy will be denoted as $E(N_1, t_1, \bar{t}_1, \varepsilon_1; N_2, t_2, \bar{t}_2, \varepsilon_2)$, where the two sets of variables pertain to sub-chains 1 and 2. In all cases, we assume periodic boundary conditions. The energy cost or stabilization that results from creating such a compound system:

$$\begin{aligned} E^{(\mathrm{s})} &\equiv E(N_1, t_1, \bar{t}_1, \varepsilon_1; N_2, t_2, \bar{t}_2, \varepsilon_2) \\ &- \Big[E(N_1 + N_2, t_1, \bar{t}_1, \varepsilon_1) \frac{N_1}{N_1 + N_2} \\ &\quad + E(N_1 + N_2, t_2, \bar{t}_2, \varepsilon_2) \frac{N_2}{N_1 + N_2} \Big] \end{aligned} \tag{4.3}$$

yields the (double of) energy cost of bringing the two bulk systems in contact, per unit area. The label "s" refers to "solvation." To appreciate that the above expression does, in fact, reflects the interface energy *per unit area*, imagine a simple cubic lattice

where each vertex hosts p_x, p_y, and p_z orbitals and no other orbitals, and ignore the $pp\pi$ interactions. (This is the lowest- order approximation for the electronic structure of rhombohedral arsenic and black phosphorus. [9]) Clearly the energy of the system is simply the sum of the energies of the individual chains, each of which is $pp\sigma$ bonded. Thus the energy cost of a "defect" in the form of an extended, contiguous surface comprised of relatively local defects on individual chains will scale with the surface area. Let us now add other types of orbitals and $pp\pi$ interactions. The chains are no longer independent, and so the magnitude of the energy cost of the interface will generally change. Nevertheless, the cost will still scale with the surface area as long as the interface has a finite width, something we shall return to in due time.

There are standard methods to obtain spectra of such compound one-dimensional systems in an essentially analytical fashion, [103, 104] however as a practical matter, it will be more efficient to diagonalize such Hamiltonians numerically, which also gives one direct access to useful quantities such as the density matrix.

To set the stage, we bring in contact an insulator $\varepsilon_1 = 1$, $\bar{t}_1 = 1$, $t_1 = 0$ and a metal $\varepsilon_2 = 0$, $\bar{t}_2 = 1$, $t_2 = 0$. The spectrum is shown in Fig. 4.1. The compound spectrum reproduces the spectra of the constituent sub-systems where the latter do not spectrally overlap, but otherwise "interpolates" between the two. The reason for this is particularly obvious in the continuum limit. Where the spectra of the sub-parts overlap, the solution can be thought of as a wave that propagates through the whole sample while undergoing refraction at the boundary. In non-overlapping spectral regions, on the other hand, solutions can be thought of as standing waves within the conducting part of the sample; the wave is attenuated exponentially fast

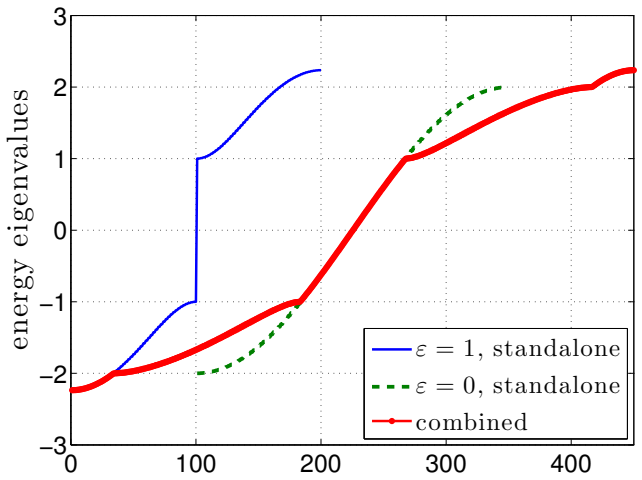

Figure 4.1: The spectrum of an on-site CDW insulator ($\varepsilon_1 = 1$, $\bar{t}_1 = 1$, $t_1 = 0$, $N_1 = 200$) in contact with a metal ($\varepsilon_2 = 0$, $\bar{t}_2 = 1$, $t_2 = 0$, $N_2 = 250$) is shown in red line with a symbol. The spectra of the standalone components are placed on the graph so as to ease comparison with the spectrum of the combined system. The horizontal axis shows site number along the $N = N_1 + N_2$ member chain.

within the insulator.

We next show the cost $E^{(\mathrm{s})}$ of bringing together an ionic insulator and a metal, $\bar{t}_1 = \bar{t}_2 = 1$, $t_1 = t_2 = 0$, $\varepsilon_2 = 0$, as a function of the quantity ε_1, the latter determining the degree of the ionicity of the insulator, see Fig. 4.2. The cost is positive and is seen to increase monotonically with ε_1. Likewise, bringing in contact an insulator with bond-order wave and a metal, $\bar{t}_1 = \bar{t}_2 = 1$, $t_2 = 0$, $\varepsilon_1 = \varepsilon_2 = 0$ always costs energy, which increases with the magnitude of the gap, as is seen in Fig. 4.3, where we plot $E^{(\mathrm{s})}$ as a function of t_1. In contrast, bringing together two metals results in *stabilization*, see Fig. 4.3.

It is straightforward to see that the solvation energy tends to a fixed number in the $N_1, N_2 \to \infty$ limit. That is, the solvation is indeed an interfacial effect.

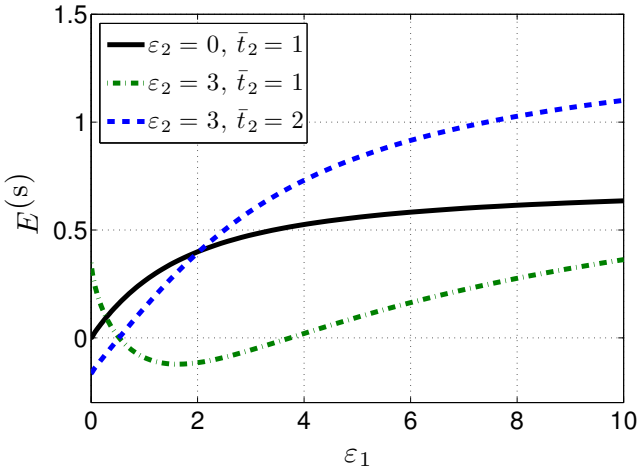

Figure 4.2: The "solvation" energy from Eq. (4.3) as a function of ε_1, $N_1 = 100$, $N_2 = 102$. In all cases, $\bar{t}_1 = 1$, $t_1 = t_2 = 0$.

To appreciate the latter notion, we graph in Fig. 4.4 the spatial dependence of the diagonal $P_{\alpha\alpha}$ and the first off-diagonal $P_{\alpha,\alpha+1}$ element of density matrix:

$$P_{\alpha\beta} = \sum_{s=\pm 1/2} \left\langle c^{\dagger}_{\alpha,s} c_{\beta,s} \right\rangle = 2 \sum_{k,\,\mathrm{occ}} \psi_{k\alpha} \psi^{*}_{k\beta}, \tag{4.4}$$

where $\psi_{k\beta}$ are the expansion coefficients of the normalized k-th solution of the Schrödinger equation corresponding to Eq. (4.1); the sites are labeled with Greek letters. The summation is over the occupied states. The charge wave is clearly visible on the ionic side of the interface. The wave decays—though does not fully vanish—in the bulk of the metallic part, which is witnessed by a small, but non-vanishing alternation of the density matrix entries in the metal. The (weak) charge-density wave in the metal results from the electronic wavefunctions comprising the CDW in the insulator that "spill" into the metal; the transmission coefficient of the interface may be small but it is non-zero. One thus expects that in 3D, the charge density wave will decay into the metal inversely proportionally with the distance squared

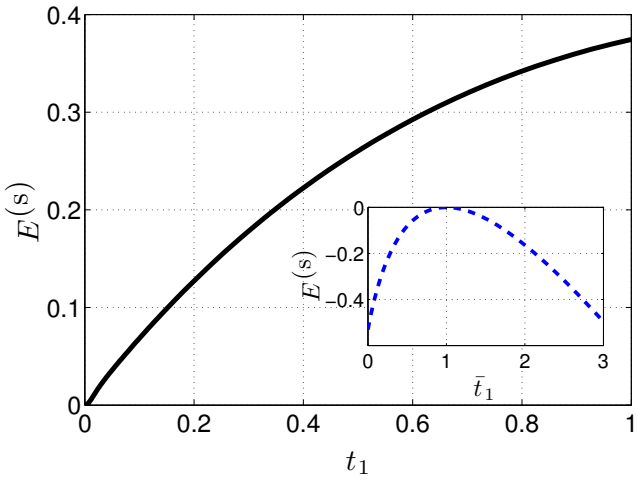

Figure 4.3: The "solvation" energy from Eq. (4.3) for two bond-order insulators, as a function of t_1. Here, $\varepsilon_1 = \varepsilon_2 = 0$, $t_1 = t_2 = 1$, $t_2 = 0$. *Inset*: The stabilization due to bringing two metals in contact, as a function of $\bar{t}_1$. Here, $\varepsilon_1 = \varepsilon_2 = t_1 = t_2 = 0$, $\bar{t}_2 = 1$. $N_1 = 100$, $N_2 = 102$.

from the interface, as would the intensity of any wave in 3D. Now, the rapid onset of the CDW on the insulating side of the interface is readily explained by the rapid decay of the metallic wavefunction as it attempts to tunnel through the insulating gap.

To flesh out the above notions on the penetration of the CDW into the metal more explicitly, we note that the Hamiltonian (4.1) can be broken up, in a standard fashion, into a set of $N/2$ non-interacting two-state systems. Each such system operates on two plane waves, each at wavevector k, spanning the odd- and even-numbered sites, respectively: [25]

$$|\psi_k^{\rm odd}\rangle = (2/N)^{1/2} \sum_n |\psi_{2n+1}\rangle e^{ika\,(2n+1)} \tag{4.5}$$

$$|\psi_k^{\rm even}\rangle = (2/N)^{1/2} \sum_n |\psi_{2n}\rangle e^{ika\,2n}. \tag{4.6}$$

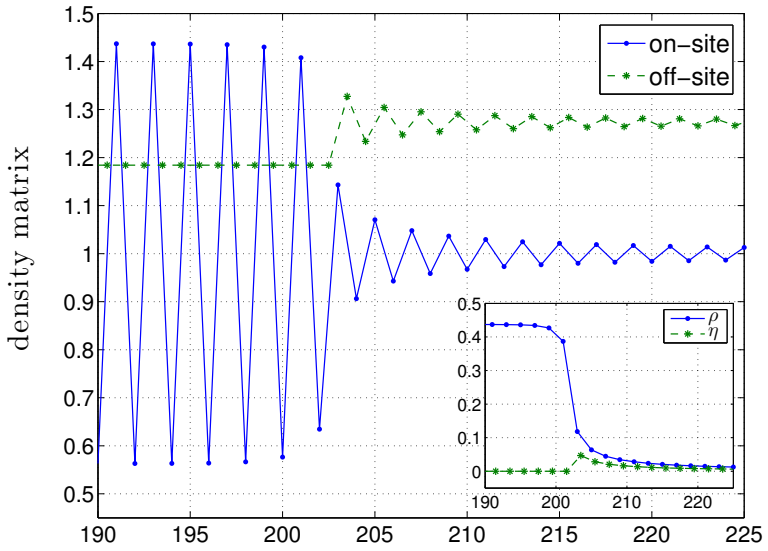

Figure 4.4: The on-site, P_{ii}, and off-site, $(P_{i,i+1}+P_{i+1,i})$, entries of the density matrix near an interface for the compound system $N_1 = 202$, $N_2 = 200$, $\varepsilon_1 = 0.5$, $\varepsilon_2 = 0$, $\bar{t}_1 = \bar{t}_2 = 1$, $t_1 = t_2 = 0$. *Inset*: The corresponding order parameters from Eq. (4.10) and (4.19). The horizontal axis shows site number for the $N = N_1 + N_2$ member chain. The vertical axis shows dimensionless, on-site electron density values.

The kets $|\psi_n\rangle$ stand for the basis set of the matrix H_{mn} defining the tight-binding Hamiltonian from Eq. (4.1): $\mathcal{H}(N, t, t_0, \varepsilon) \equiv \sum_{mn,s} H_{mn} c^\dagger_{m,s} c_{n,s}$. The two-level system, for each value of k, is defined by the matrix:

$$\left(\begin{array}{c|c} -\varepsilon & -2\bar{t}\cos ka + 2it\sin ka \\ \hline -2\bar{t}\cos ka - 2it\sin ka & \varepsilon \end{array}\right), \tag{4.7}$$

where a is the lattice spacing. The resulting spectrum is:

$$E_k = \mp[\varepsilon^2 + 4t^2 + 4(\bar{t}^{\,2} - t^2)\cos^2 ka]^{1/2}. \tag{4.8}$$

It is doubly degenerate: $E_k = E_{-k}$.

The relative weights of the waves (4.5) and (4.6) in the one-particle eigenfunctions depend on the detailed values of the parameters ε, $\bar{t}$, and t. Non-equal weights result

in a perfect alternation pattern in the on-site charge; in the extreme limit $\varepsilon \to \infty$, the kets in Eqs. (4.5) and (4.6) become eigenfunctions of H_{mn} while the bonding becomes purely ionic. Thus the charge density wave in Fig. 4.4 can be thought of as resulting from a disparity in the contribution of planes waves (4.5) and (4.6) to the overall charge distribution. Alternatively, one may work in the basis set formed by equally-weighted combinations of the waves (4.5) and (4.6), viz., $(\psi_k^{\text{even}} \pm \psi_k^{\text{odd}})/\sqrt{2}$. The two correspond with the valence and conduction band orbitals of the non-dimerized chain, $t = \varepsilon = 0$, as is easily seen from Eq. (4.7). Because of the aforementioned degeneracy $E_k = E_{-k}$, and the equivalence of points k and $k + \pi/a$, one can think of the Hamiltonian (4.7) as mixing left- and right-movers, the reference state being $k = \pi/2a$. [53] To summarize, the presence of a (weak) CDW on the metal side stems from non-equal weights of either waves (4.5) and (4.6) or right- and left-movers, or a combination thereof. The lack of scaling of the interface energy with the system size can be formally traced to the lack of dependence of the transmission coefficient of the interface on the overall system size, for sufficiently large values of the latter.

An additional way to look at the apparent mismatch between the charge-density patterns between the insulator and metal—which will also prove useful later on—is to consider the overlap between the full, multi-particle solutions of the Hamiltonian (4.1) for distinct values of the on-site energies and/or hopping matrix elements. Although generally a difficult problem, computation-wise, [105] it becomes relatively straightforward in the present setup because any two one-particle eigenfunctions of the Hamiltonian (4.1) could have a non-zero overlap only if they correspond to the same wave-vector k, whether the parameters of the Hamiltonian are different or

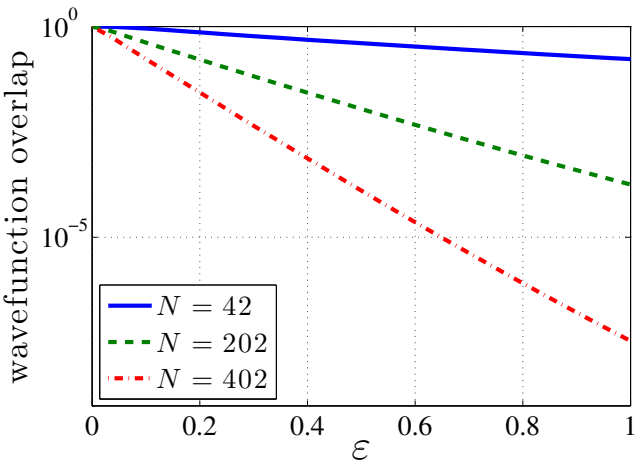

Figure 4.5: The dimensionless overlap between two wave-functions, from Eq. (4.9) for three systems: $N = 22+20$, $102+100$, and $202+200$, as a function of $\varepsilon = \varepsilon_1 = \varepsilon_2$. In the reference system, $\varepsilon = 0$. For both (compound) systems, $\bar{t}_1 = \bar{t}_2 = 1$, $t_1 = 0$, $t_2 = 0.01$. ε and t are dimensionless energy quantities from the tight-binding model in Eq. 4.1

not. This reduces the computation of the overlap between the two *many*-particle wave-functions—both of which are Slater determinants composed of one-particle functions—to the product of the overlaps of the individual one-particle wavefunctions that correspond to the very same value of k, over the occupied states. And so, the magnitude of the overlap is given by

$$|\left\langle \Psi^I | \Psi^{II} \right\rangle| = \prod_{k,\,\mathrm{occ}} |\left\langle \psi_k^I | \psi_k^{II} \right\rangle|. \tag{4.9}$$

To reduce the ambiguity as much as possible, we will compare the ground state solutions for Hamiltonians that differ by the value of only one parameter. Further, we will introduce some spatial inhomogeneity in the parameters so as to remove the $E_k = E_{-k}$ degeneracy mentioned above. In Fig. 4.5, we show the dependence of the overlap from Eq. (4.9) on the electronegativity variation of system I, ε^I, for the following two systems: $\bar{t}^I = \bar{t}^{II} = 1$, $\varepsilon^{II} = 1$. The quantity t is set at a small value

0.01 in one half of each sample. The overlap is unity for two identical systems, of course, but decreases with the difference $|\varepsilon^I - \varepsilon^{II}|$. Most importantly, the overlap decreases *exponentially* fast with the system size. This is expected since each factor in the product in Eq. (4.9) is less than one when $|\varepsilon^I - \varepsilon^{II}| > 0$, at least for not too large value of the latter quantity. Making the system, say, twice larger essentially amounts to making the number of factors in Eq. (4.9) twice greater where each new factor approximately duplicates an existing factor. This is because the quantity $|\left\langle \psi_k^I | \psi_k^{II} \right\rangle|$ is a smooth function of k in the $N \to \infty$ limit. Thus in this limit, making the system bigger by a factor of M results in raising the expression on the r.h.s of Eq. (4.9) to power M. Consequently, $|\left\langle \Psi^I | \Psi^{II} \right\rangle| \propto e^{-\text{const} \times N}$ at most.

Note that the wavefunction overlap may vanish identically because of symmetry. For instance, switching the sign of ε and t at the same time results in the HOMO and LUMO switching their identity, as can be seen by plugging $k = \pm\pi/2a$ into Eq. (4.7). Since the HOMO and LUMO of the same system are automatically orthogonal, the overlap between the HOMOs of two systems differing only by the sign of ε and, at the same time, the sign of t, will be identically zero. Thus the overlap of the corresponding multi-particle wavefunctions will vanish. With this in mind, we note that the situation reflected in Fig. 4.5 is the worst-case scenario in the sense that it gives an upper bound for the multi-particle wavefunction overlap. Finally note that interfaces separating states with distinct symmetries may host special surface states at energies forbidden in the bulk; these states contribute to the surface penalty and are the subject of Chapter 5.

The actual quantity pertinent to assessing the penetration of a charge density wave into a metallic substrate is the matrix element $\left\langle \Psi^{\rm ins}|\mathcal{H}^{\rm metal}|\Psi^{\rm metal}\right\rangle = \sum_n E_n|\left\langle \Psi_n^{\rm ins}|\Psi^{\rm metal}\right\rangle|^2$, where the summation is over the eigen-states of the metal, E_n being the corresponding energy eigen-values. The latter expression reduces to the overlap between the ground-state multiparticle wavefunctions only when the hybridization between the insulator's wavefunction and the excited states of the metal is negligible, which is generally not the case. Still, qualitatively, one concludes that the stabilization, if any, due to bringing together two systems will be the greater the more "similar" the ground state wavefunctions and, hence, the charge density patterns. For instance, it $\bar{t}_2 > \bar{t}_1$, one expects that the greatest stabilization will be achieved when $\varepsilon_2 > \varepsilon_1 > 0$ or $\varepsilon_2 < \varepsilon_1 < 0$. This is borne out by data in Fig. 4.2. One corollary of the above results is that bringing together two metals with identical lattices will likely result in stabilization, see Fig. 4.3, unless there is a substantial disparity in the atom size. Thus, two metals with identical lattices and similar atomic sizes and make-ups of the frontier orbitals will readily alloy.

4.4 Miscibility and the metal-insulator transition

We have formally considered the magnitude of the charge wave as a function of the electronegativity ε. Alternatively, one could consider the charge distribution as the independent variables, where one would have to self-consistently determine the local values of ε necessary to achieve a desired charge distribution pattern. The two descriptions are often equivalent, but may have their distinct advantages depending

on the context. Here, we will profit from switching to the charge-density based description. For concreteness, we first focus on the on-site wave, as opposed to the bond-order wave, and set $t = 0$ until further notice. For a spatially-homogeneous ε—which implies a perfectly alternating electronegativity pattern—an appropriate order parameter is the charge difference between the odd- and even-numbered sites, per site:

$$\rho \equiv \frac{1}{2}(P_{2n+1,2n+1} - P_{2n,2n}). \tag{4.10}$$

Clearly,

$$\rho = -\frac{\partial E}{\partial \varepsilon}, \tag{4.11}$$

where E is the energy per site. For the non-interacting model from Section 4.3, the energy per site is equal to

$$E_0 = \frac{2}{N} \sum_{k,\mathrm{occ}} E_k, \tag{4.12}$$

where E_k is the energy eigen-value from Eq. (4.8) and the factor of 2 comes from the summation over the spin states, as in Eq. (4.4). In addition to Eq. (4.11), the charge differential ρ can be computed directly as $\rho = N^{-1} \sum_\alpha (P_{2\alpha+1,2\alpha+1} - P_{2\alpha,2\alpha})$, where P is the density matrix from Eq. (4.4).

Both quantities E and ρ in Eq. (4.11) are formally functions of ε. Insofar as there is one-to-one correspondence between ρ and ε, one can perform a Legendre transform according to:

$$E^{\mathrm{inh}}(\rho) = E + \varepsilon\rho, \tag{4.13}$$

where all quantities on the right are now regarded formally as functions of ρ and, of course:

$$\varepsilon = \frac{\partial E^{\mathrm{inh}}(\rho)}{\partial \rho}. \tag{4.14}$$

The label "inh" is aimed to emphasize that the quantity $\partial E^{\mathrm{inh}}(\rho)$ gives the inherent energy of the electrons as a function of the electronic density distribution, in the *absence* of electronegativity variation. The existence of the inherent energy $E^{\mathrm{inh}}(\rho)$ is guaranteed by the venerable Hohenberg-Kohn theorem. [5] In the charge-density based formalism, the actual value of ρ is found by matching the derivative of $E^{\mathrm{inh}}(\rho)$ with respect to ρ with the externally imposed value of ε.

The Legendre transformation above is entirely analogous to how one can describe a harmonic oscillator $E^{\mathrm{inh}(x)} = \kappa x^2/2$, κ being the force-constant, by using either the coordinate x or, instead, in terms of the oscillator's response to a force f. The energy in the presence of the force, as a function of the force, is given by $E(f) = \min_x(\kappa x^2/2 - fx) = -f^2/2\kappa$. The equilibrium value of the displacement is $x = -\partial E/\partial f = f/\kappa$, c.f. Eq. (4.11), while the corresponding force is given by $f = \partial E^{\mathrm{inh}}/\partial x = \kappa x$, c.f. Eq. (4.14). Finally, $E^{\mathrm{inh}} = E + fx$, c.f. Eq. (4.13). In a more substantive way, the quantities $E^{\mathrm{inh}}(\rho)$ and $E(\varepsilon)$ are analogous to the Helmholtz free energy $A(V)$ and Gibbs free energy $G(p)$ as functions of the volume V and pressure p, respectively. A closer yet analogy of the functions $E^{\mathrm{inh}(\rho)}$ and $E(\varepsilon)$ is with the Helmholtz free energy per unit volume $a(n)$ and the grand-canonical potential [29, 106] per unit volume: $\omega(\mu) = a - \mu n$, where n and μ are the concentration and chemical potential respectively. The latter thermodynamic potential naturally arises in classical-DFT treatments of liquid mixtures, see Section

II of Ref. [63] for a detailed discussion. The quantity $\omega(\mu)$ is equal to the negative pressure. Likewise, the energy E and electronegativity variation ε can be regarded as the negative (osmotic) pressure, times specific volume, and the effective chemical potential pertaining to charge-density waves.

Now, the function $E^{\mathrm{inh}}(\rho)$ presents a convenient way to model emergence of the site-based charge wave. In the absence of externally— chemically or otherwise— imposed electronegativity variation, the equilibrium value of ρ is determined by the position of the stable minima in $E^{\mathrm{inh}}(\rho)$, since $0 = \varepsilon = \partial E^{\mathrm{inh}}(\rho)/\partial\rho$. No spontaneous CDW, $\rho \neq 0$, could arise in the non-interacting system from Section 4.3, which is formally reflected by the function

$$E^{\mathrm{inh}_0}(\rho) \equiv [E_0 + \varepsilon(-\partial E_0/\partial\varepsilon)](\rho), \tag{4.15}$$

having its sole minimum at $\rho = 0$, see curve 1 in Fig. 4.6(a). The lack of spontaneous CDW is consistent with the obvious fact that in the absence of external potential, the Schrödinger equation is solved by a plane wave. The one-dimensional $E_0^{\mathrm{inh}}(\rho)$ is qualitatively similar to its counterpart in higher spatial dimensions except near the origin. The latter are strictly stable at small ρ: ${E_0}^{\mathrm{inh}}(\rho) \propto \bar{t}\rho^2$, while the curvature of the former vanishes (at the Born-Oppenheimer level [107]): $E_0^{\mathrm{inh}}(\rho) \propto \bar{t}\rho^2(-\ln^{-1}|\rho|)$ owing to the Van Hove singularity at $|k| = \pi/2a$. The ensuing lack of stability is, of course, just another way to see why one-dimensional metals could not exist.

The functional $E_0^{\mathrm{inh}}(\rho)$ bears obvious qualitative similarities with the classical mixing free energy of an ideal binary mixture $F_{\mathrm{mix}}(\rho) = k_B T[(1-\rho)\ln(1-\rho) + (1+\rho)\ln(1+\rho) - 2\ln 2]/2$, [7, 60] where $\rho = \pm 1$ correspond to the two pure components.

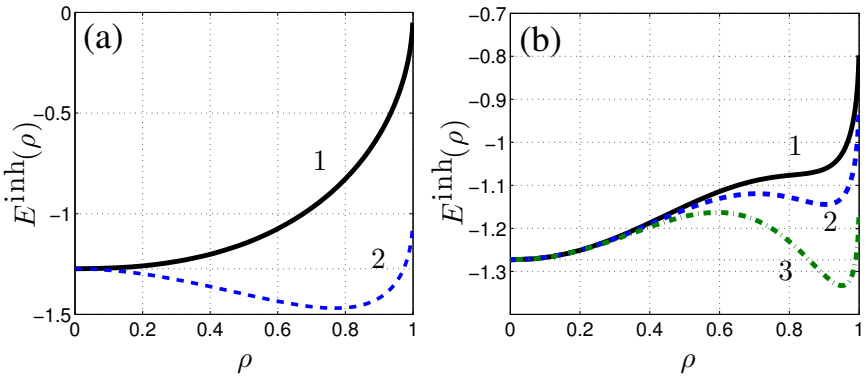

Figure 4.6: **(a)** The inherent energy corresponding to Eq. (4.1). $\bar{t} = 1$, $t = 0$. Curves 1 and 2 correspond to the bare case and that with an added interaction $A\rho^2/2$, $A = -2$. **(b)** The inherent energy corresponding to Eq. (4.1), $\bar{t} = 1$, $t = 0$, with an added interaction $A\rho^2/2 + C\rho^4/4$, $A = 0.5$. Curves 1, 2, and 3 correspond to $C = -4$, -4.5, and -5.5, respectively. Dimensionless ρ values are represented by the horizontal axis.

Most significantly, the slope of both $F_{\rm mix}(\rho)$ and $E_0^{\rm inh}(\rho)$ diverges near $|\rho| = 1$ as $\ln(1-|\rho|)$ and $(1-|\rho|)^{-1/2}$ respectively. In other words, complete localization, $|\rho| = 1$, is even harder to achieve in the quantum case. The distinct $|\rho| \to 1$ asymptotics will lead to detailed effects but do not, by themselves, modify the qualitative picture of mixing between phases characterized by distinct values of ρ, since the main action occurs at values of ρ that are well short of the extremes ± 1; this is witnessed by Fig. 4.6.

Because the second derivative $\partial^2 E_0^{\rm inh}(\rho)/\partial\rho^2$ is positive throughout (except at an isolated point, $\rho = 0$, in 1D), there are no two distinct values ρ at which the first derivatives $\partial E_0^{\rm inh}(\rho)/\partial\rho$ are equal. As a result, the non-interacting model cannot exhibit a coexistence between two phases characterized by distinct CDWs. Let us now add to the bare energy function from Section 4.3 an interaction term, which can

be always presented as a function of the electronic density:

$$E^{\text{inh}}(\rho) = E^{\text{inh}_0}(\rho) + V_{\text{intr}}(\rho). \tag{4.16}$$

To set the stage, we first account, in a meanfield fashion, for a two-body interaction that arises from Coulomb stabilization when local excess of positive and negative charge due to the CDW forms, by employing $V_{\text{intr}}(\rho) = A\rho^2/2$, $A < 0$. This can be viewed equivalently either as a Coulomb attraction between nearby electron and hole-rich regions or as electron-electron (hole-hole) repulsion on an individual site. There are two meanfield aspects to this approximation: On the one hand, it does not explicitly account for density-density correlations since it decouples them [108] according to $\langle c_i^\dagger c_i c_j^\dagger c_j\rangle \to \langle c_i^\dagger c_i\rangle\langle c_j^\dagger c_j\rangle$. On the other hand, one should generally account for interactions within a *range* of wavelengths, not just the dominant wavelength, [109] $2a$ in this case. Now, for a sufficiently large and negative value of $A < A_0$, the function E^{inh} will become bi-stable implying that that the symmetry must be broken and that the system must choose one of the two minima corresponding to opposite signs of $\rho \propto \pm(A_0 - A)^{1/2}$. [30] Since the magnitude of such a spontaneously formed CDW depends continuously on the parameters of the interaction, we observe that at the two-body level, Coulomb interactions may lead at most to a *continuous* transition between the metallic and insulating state, the two characterized by $\rho = 0$ and $\rho \neq 0$ respectively. These notions are graphically summarized in Fig. 4.6(a).

A distinct situation arises when we include higher order interaction effects already at the four-body level:

$$V_{\text{intr}} = \frac{A}{2}\rho^2 + \frac{C}{4}\rho^4. \tag{4.17}$$

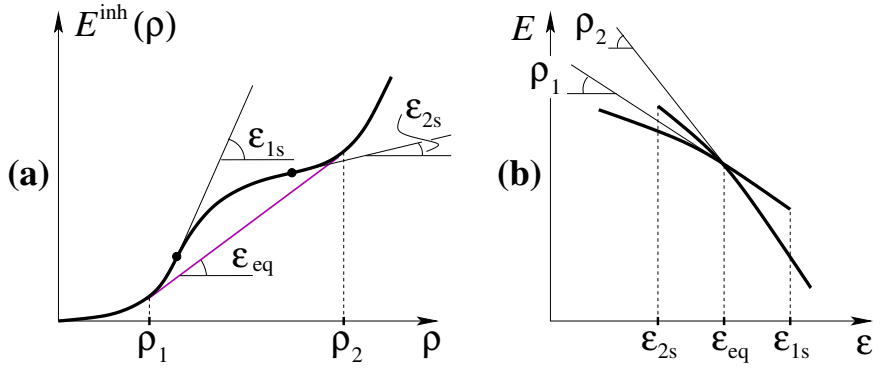

Figure 4.7: The presence of a non-concave portion in the inherent energy $E^{\rm inh}(\rho)$, c.f. curve 1 from Fig. 4.6(b), corresponds with the presence of two terms in the energy proper, as a function of the electronegativity variance ε. The slopes ε_{1s} and ε_{12s} at the inflection points of the $E^{\rm inh}(\rho)$ curve correspond with the term ends for the energy $E(\varepsilon)$. The term-crossing becomes genuine in the thermodynamic limit, according to Fig. 4.5.

For sufficiently large and negative values of C, the energy function $E^{\rm inh}$ develops a non-concave portion, where $\partial^2 E^{\rm inh}(\rho)/\partial\rho^2 < 0$; this is shown by curve 1 in Fig. 4.6(b). In a standard fashion, this non-concave portion separates two phases that correspond to distinct, non-zero magnitudes of the CDW and, hence, to distinct, non-vanishing degrees of charge localization. Both phases correspond to insulators, see Fig. 4.7(a), the more insulating phase corresponding to a higher degree of localization. To appreciate the latter notion we recall that the insulating gap is determined by the slope of the bare part of the inherent energy $\varepsilon_0 = \partial E^{\rm inh0}/\partial\rho$, which must be used in Eq. (4.8). By Eqs. (4.14) and (4.16),

The energy proper $E(\varepsilon)$ that corresponds to the inherent energy $E^{\rm inh}(\rho)$ from Fig. 4.7(a) is not difficult to determine, by Eqs. (4.11)-(4.14); see the sketch in

Fig. 4.7(b). Although the inherent energy, Fig. 4.7(a), is a perfectly smooth function of ρ, the actual energy, as a function of the electronegativity variation, is given by the lower of the two intersecting terms and thus exhibits a discontinuity in slope. (To avoid confusion, we note the Legendre transform from Eq. (4.13) must be performed separately for individual terms, each of which is a single-valued, monotonically decreasing function of ε.) We have seen in the preceding Section that the term-crossing in Fig. 4.7(b) is not genuine in that the overlap between the respective wavefunctions disappears only in the thermodynamic limit. Incidentally, one may ask whether there could be a non-smooth $E^{\mathrm{inh}(\rho)}$, say, in the form of two intersecting terms. Such situation is expressly forbidden by the Hohenberg-Kohn theorem [5] because it would amount to having the same density distribution for two distinct values of ε, by virtue of Eq. (4.14). We thus conclude that using the density as a single variable is permissible for arbitrarily degenerate configurations, whereas in a field-based formalism, a separate set of molecular fields is needed for each distinct state.

A negative coefficient C in Eq. (4.17) formally implies that the material's polarizability [110] *decreases* with the magnitude of the charge-density wave and, hence, the degree of charge localization. This is, of course, expected on physical grounds; the magnitude of the effect will be system-dependent. Importantly, this notion allows one to connect the present formalism with the well known phenomenon of poor miscibility of substances with differing degrees of polarizability such as oil and water. Indeed, the present discussion implies that the question of mutual miscibility of two distinct substances can be analyzed as a coexistence of two distinct phases of the very *same* substance, the distinction between the phases being different degrees of

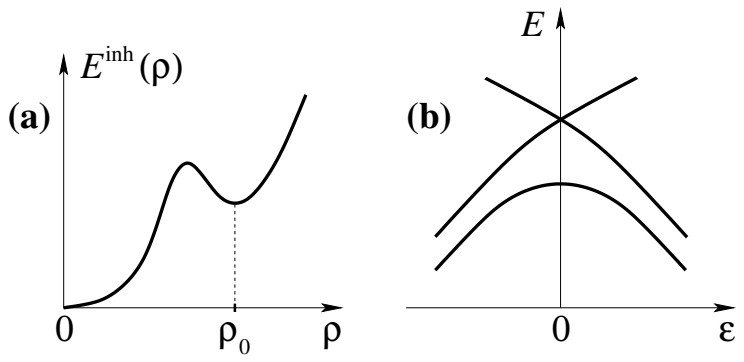

Figure 4.8: **(a)** A metastable minimum in $E^{\rm inh}(\rho)$ is thermodynamically significant when it corresponds to a bulk-degenerate configuration. When $E_{\rm inh}(-\rho)$ is defined for both signs of ρ and $E_{\rm inh}(-\rho) = E_{\rm inh}(\rho)$ (the $\rho < 0$ portion not shown), such a metastable minimum corresponds to a genuine, symmetry-related term-crossing for the actual energy.

charge localization and, at the same time, polarizability. For the type of intrinsic energy shown in Fig. 4.7, the difference between the magnitude of CDW is chemically built-in in that the chemical moieties comprising the two phases have distinct electronegativities.

In the absence of such built-in electronegativity variation, however, the system from Fig. 4.7 will remain in the metallic state. By further decreasing the polarizability of the insulating state, one can make the latter metastable, see curve 2 in Fig. 4.6(b), and Fig. 4.8(c). We immediately observe that the system must have a doubly degenerate excited state at $\varepsilon = 0$, see Fig. 4.8(b). The term-crossing at $\varepsilon = 0$ is genuine for symmetry reasons explained in Section 4.3. Because the minimum is metastable, the system from Fig. 4.8 will not undergo a metal to insulator transition except when the minimum is appropriately degenerate, see reference [111].

Given a sufficiently strong dependence of the electronic polarizability on the degree of charge localization the metastable minimum from Fig. 4.8(a) can be made as deep or deeper than the minimum at $\rho = 0$, see curve 3 in Fig. 4.6(b). Under such circumstances, a charge density wave will form spontaneously even in the absence of chemically built-in variation in electronegativity. As in the preceding case, this is an instance of a metal-insulator transition. Note the $E_0^{\rm inh}(\rho) \propto \bar{t}\rho^2$ trend, $\rho \to 0$, is consistent with the greater stability of broad-band materials metals with respect to the metal-to-insulator transition. [42] The present discussion is consonant with the much earlier discussion on the discontinuity of the metal-insulator transition by Mott and many others. [6, 112] In the latter picture, the metallic state arises as a result of the closure of an indirect gap. For a sufficiently small gap, however, it could be energetically favorable for electrons and holes to be excited to the conduction and valence band, respectively, as long as the two quasiparticles can form an exciton with a sufficiently large binding energy. Such excitons would further condense into droplets. As a result, the material remains insulating even though the one particle gap is zero. Upon the eventual transition to the metal state, the two bands overlap by an already finite extent and so the number of charge carriers becomes immediately finite thus implying the insulator-to-metal transition is discontinuous. In the present description, the coefficients A and C reflect, respectively, the extent of stabilization due to exciton formation and their further aggregation. Indeed, the concentration of excitons should scale quadratically with the excess local charge ρ. In turn, the exciton-exciton interaction should scale quadratically with the concentration of the excitons and, hence, quartically with ρ. We thus suggest that in contrast with Mott's

own conclusions, his exciton scenario could lead to either continuous or discontinuous transition, depending on the polarizability difference between the metal and insulator. Still, the above notions suggest a more general mechanism for the discontinuity of the metal-insulator transition, as we discuss next.

In what follows, we will take a more general view of Hamiltonian (4.1)—plus whatever interaction-related additions as in Eq. (4.17)—in which the sites may or may not correspond to atomic orbitals. The invariance of the Hamiltonian (4.1) with respect to the sign reversal of the electronegativity variation ε or the hopping matrix variation t comes about because flipping the signs of ε and t either separately or at the same time is equivalent to renumbering the sites. (Note reversing the order of sites may be necessary.) Similar symmetry can be realized in a number of common periodic 3D lattices. For instance, the rock salt structure consists of two equivalent, interdispersed fcc lattices. Flipping the sign of ε amounts to swapping the anionic and cationic sites and thus results in an equivalent lattice. Likewise, the cesium chloride structure consists of two equivalent, interdispersed simple-cubic lattices. Yet another example is provided by the zincblende lattice, which consists of two equivalent fcc structures shifted relative to each other so that the vertices of the combined lattice coincide with those of the diamond lattice. All of the aforementioned lattices belong to the cubic system. Clearly, stretching the unit cell in any direction or tilting the principal axes will not modify the basic symmetry with respect to interchanging the more and less electronegative sites.

A distinct type of two equivalent, mutually-complimentary CDWs in the form of *stripes* is provided by bond-order waves found in rhombohedral arsenic and black

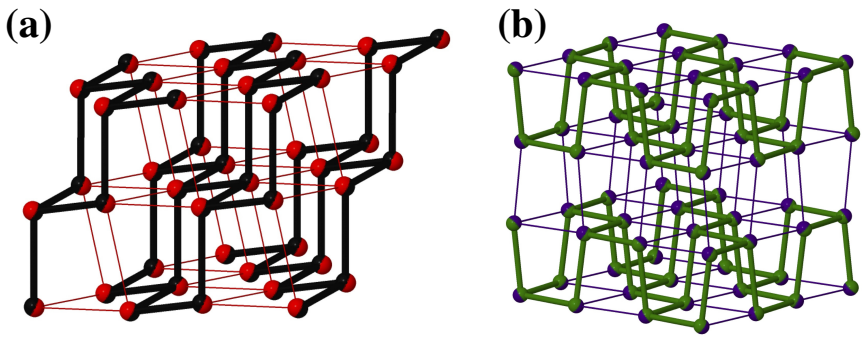

Figure 4.9: . **(a)** The structures of rhombohedral arsenic, **(a)**, and black phosphorus **(b)**. Two alternative, mutually complementary ways to connect the atoms are shown with thick solid and thin dashed lines, respectively. We have reduced the distortion away from the simple-cubic lattice, compared with the actual structures, for clarity.

phosphorus. Both structures can be thought of as obtained as a result of the following procedure, see Fig. 4.9: Take a simple-cubic structure; assign links and gaps between nearest neighbors so that the link and gap patterns are self-complimentary; and deform the structure so that the linked sites are covalently bonded. According to the computational study by Silas et al. [32], the rhombohedral-to-simple cubic transition in arsenic is indeed continuous.

Although of practical significance, charge density waves made of equivalent, mutually-complimentary lattices or structures constitute only a vanishing subset of all possible periodic, let alone aperiodic patterns. Thus the $\rho \leftrightarrow (-\rho)$ symmetry of the energy is not generally present, thus leading to a non-vanishing coefficient at the third-order in the free energy expansion, as in:

$$V_{\rm intr} = \frac{A}{2}\rho^2 + \frac{B}{3}\rho^3 + \frac{C}{4}\rho^4, \tag{4.18}$$

where $C > 0$. This circumstance has enabled Landau [65] to argue that the liquid-to-crystal transition is generally discontinuous, see also Ref. [7] The free energy

(4.18) could, in principle, produce a continuous transition in one isolated point on the (A, B) phase diagram, viz. $A = B = 0$, to which there corresponds a unique point in the pressure-temperature phase diagram. Brazovsky [66] later emphasized that the symmetry is broken for finite-k modes while the instability for small B's is driven by the quadratic term $A\rho^2/2$, which depends only on the absolute value of k. This makes near critical fluctuations essentially one-dimensional; hence the critical point would be pushed down to $T = 0$. Alexander and McTague [113] later noticed that a non-zero cubic term particularly stabilizes the bcc structure. Locally dense structures made of monodisperse spheres are also favored by the cubic term. However, the corresponding Voronoi cell is the regular dodecahedron and does not tile space, thus highlighting the potential importance of *aperiodic* density waves. [7]

To see qualitatively why the cubic term should be generally non-zero consider the close-packed, hexagonal lattice in 2D, as shown by the blue lines and spheres Fig. 4.10. If the corresponding density profile is ρ, the complimentary, $-\rho$, lattice is the triangular lattice, as shown by the red lines and spheres in Fig. 4.10. It is easy to see that the latter lattice is 33% less dense than the hexagonal lattice when the spheres touch. This volume difference would be less for 3D structures; still, it much exceeds that between a liquid and the corresponding solid, for instance. Thus $E^{\text{inh}}(\rho) \neq E^{\text{inh}}(-\rho)$. The first order term is ρ is zero because it has to do with the total particle number, which is fixed. The next odd-order term is cubic and, thus, must be responsible for the lack of inversion symmetry. Physically, this term arises because a repulsive core implies the presence of three-body contacts, see also Fig. 2.5 of Ref. [114] The resulting minimum in the $E^{\text{inh}}(\rho)$ could be either stable or

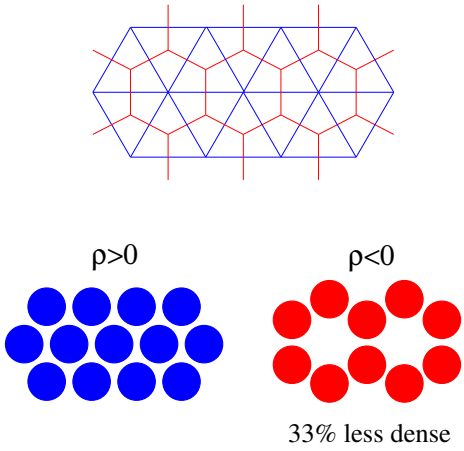

Figure 4.10: The blue and red depict the hexagonal and triangular lattices respectively. The top graphic demonstrates the two lattices mutually complement each other and thus correspond to opposite signs of the order parameter ρ.

metastable, see Fig. 4.8(a).

The above arguments are not specific to the half-filling case and thus imply that the metal-insulator transition is often discontinuous for symmetry reasons, if nothing else. In special cases when the underlying lattice has the property of consisting of two equivalent, mutually-complimentary sublattices, a continuous transition is also possible but could be undermined by polarization effects. The latter can be thought of as the formation of an excitonic lattice. Clearly such effects would not be strong enough in elemental bcc solids and hcp solids, which are metallic. From the present standpoint, the ubiquity of elemental metallic solids that are fcc is particularly obvious, since the latter lattice cannot even be represented as consisting of two equivalent, mutually-complimentary sublattices. To avoid confusion we note that the above reasoning can help rationalize the metallicity or lack thereof for a given lattice but does not, by itself, predict the lattice type.

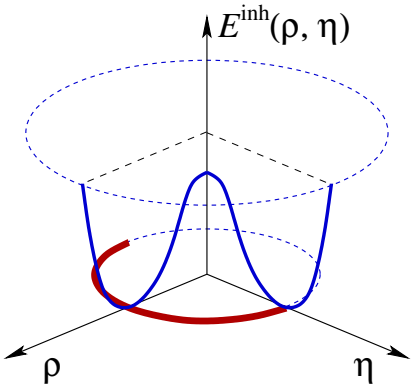

Figure 4.11: A hypothetical, rotationally-symmetric free energy profile as a function of the strength of the charge-density wave, ρ and η standing for the on-site and off-site components, respectively. The semi-circle at the bottom of the potential exemplifies a hypothetical trajectory in the (ρ, η) space for a transition between two distinct CDW states.

Next, we explicitly write out the order parameter that is useful for describing *bond*-order waves:

$$\eta \equiv \frac{1}{2}(P_{2n,2n+1} - P_{2n,2n-1}) + \text{C.C.} \tag{4.19}$$

It is straightforward to show that

$$\eta = -\frac{\partial E}{\partial t}. \tag{4.20}$$

Eq. (4.13) can be extended accordingly:

$$E^{\text{inh}}(\rho, \eta) = E + \varepsilon\rho + t\eta, \tag{4.21}$$

where the magnitude of the bond-order wave is determined by matching the value of an externally imposed hopping matrix element with the derivative of the above energy with respect to η:

$$t = \frac{\partial E^{\text{inh}}(\rho, \eta)}{\partial \eta}. \tag{4.22}$$

In the absence of interactions or externally imposed potential, the function $E^{\rm inh}(\rho,\eta)$ has a unique stable minimum at $\rho=\eta=0$, of course. With suitable interactions—even vanishingly weak would do in 1D—the symmetry could be, in principle, broken in all directions on the (ρ,η) plane. In an extreme case such a symmetry breaking could presumably yield a mexican-hat energy functional, as in Fig. 4.11. Thus we observe that even in the most minimal quantum-mechanical description, the order parameter for the metal-insulator transition or coexistence between two distinct CD phases must be generally *vectorial*. Still, the kind of symmetry breaking illustrated in Fig. 4.11 turns out to be internally inconsistent, as shown in reference [111]. Instead, the transition paths in the (ρ,η) plane ends up being largely classical, as is the case, for instance, with the Peierls dimerization of the non-interacting system (4.1). The latter can be pictured by graphing $E_0^{\rm inh}(\rho)$ as a function of ρ and t, while keeping in mind that the hopping matrix element scales exponentially with the site-site distance: $t_{n,n+1}\simeq\exp\{-c|x_{n+1}-x_n|/a\}$, where the constant c is of order (but greater than) one since the hopping matrix element decreases with distance on the lengthscale of the appropriate Bohr radius. In the lowest order, the variation of the hopping matrix element scales linearly with the bond deformation:

$$t_{n+1,n}-\bar{t}\approx\bar{t}\,c\frac{x_{n+1}-x_n-a}{a}\equiv\bar{t}\,c\frac{d_{n,n+1}}{a}(-1)^n, \tag{4.23}$$

where we have also introduced the "staggered" displacement $d_{n,n+1}$; it does not switch sign for a perfectly dimerized chain. In the presence of an elastic restoring force from the lattice, which is proportional to d, one obtains a two-well potential shown in Fig. 4.12. For sufficiently deep minima, transitions between the two can be well described by a single reaction coordinate.

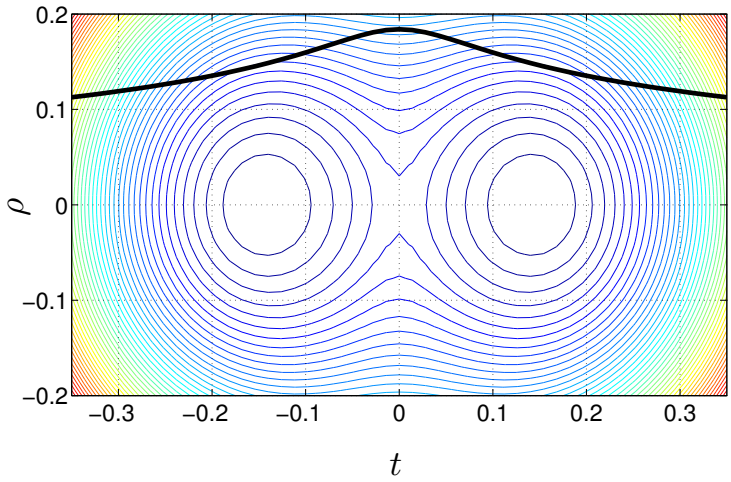

Figure 4.12: The contour plot of the energy profile corresponding to Eq. (4.1), Legendre transformed according Eq. (4.13) and with the added penalty for lattice distortion in the form of $1.5\,t^2$. The solid line corresponds with $\epsilon = 0.144$. Quantities represented on both axes are dimensionless.

The various free energies discussed above can be used for long-wavelength descriptions of charge density waves. For instance, the Hamiltonian (4.1), which is defined for fixed values of t and ε, can be generalized for parameters $t(x)$ and $\epsilon(x)$ slowly varying with the spatial coordinate x along the chain. [8, 51, 115] This is conveniently done by shifting the wavevector reference in two-level Hamiltonian (4.7) to the edge of the Brillouin zone of the original Hamiltonian (4.1), $(k - \pi/2a) \to k$, and expanding around $k = 0$:

$$\mathcal{H} = -iv\hbar\hat{\sigma}_3 \frac{\partial}{\partial x} - \varepsilon(x)\hat{\sigma}_1 - 2t(x)\hat{\sigma}_2, \tag{4.24}$$

where $v = 2\bar{t}a/\hbar$ and the operators $\hat{\sigma}_i$ are the Pauli matrices. We have relabeled the latter, $(\sigma_1, \sigma_2, \sigma_3) \to (\sigma_2, \sigma_3, \sigma_1)$, so that Hamiltonian (4.24) now operates on spinors with components $\psi_1 = (\psi^{\text{odd}} + \psi^{\text{even}})/\sqrt{2}$ and $\psi_1 = (\psi^{\text{odd}} - \psi^{\text{even}})/\sqrt{2}$, i.e., the right and left movers. Consistent with preceding conclusions, a charge density wave can be

described by a spin-1/2 dipole subject to a space-varying field whose components are $\varepsilon(x)$ and $2t(x)$. The on-site and off-site charge density waves are clearly equivalent at the continuum level. Note the quantity $2t(x)$ is proportional to (the continuum version of) the staggered deformation:

$$t(x) \propto d(x). \tag{4.25}$$

4.5 Discussion

We have taken the view of a metal-to-insulator transition as a transition between delocalized and localized particles. The latter view has led to quantitative descriptions of the liquid-to-crystal and uniform-liquid-to-glass transitions in classical systems. Both quantum and classical cases can be treated using the venerable formalism of the density functional theory. The density functional approach allows one to connect many seemingly distinct problems. On the one hand, we have established that the questions of mutual solubility of two species and the metal-to-insulator transition are intrinsically related. Except in the presence of special symmetry, the latter transition is always discontinuous; the penalty for bringing together an insulator and metal is quite analogous to that arising when one tries to mix oil and water. Exceptions to this rule are lattices that, when undistorted, consist of two equivalent, mutually complementary lattices, such as those leading to the distorted lattices in Fig. 4.9.

The non-uniform electronic density profile in solids results from a lowering of the translational symmetry due to the stationary nuclei. In the insulator, the translational symmetry is fully broken: The electrons can be regarded as fully localized. In

a metal, the translational symmetry would seem to be partially restored because the conduction electrons behave almost as free particles. This view is flawed, however: If such a metal becomes insulating, no Goldstone modes appear. Whatever optical phonons that may appear as a result of the transition are gapped excitations, of course. The story is much more interesting, however. Although known to appear in select cases, such as trans-polyacetylene, special *midgap electronic states* are argued to reside at the interfaces separating distinct, degenerate CDW states. The discrete symmetry breaking that leads to the appearance of these states and disappearance of the Goldstone modes is treated in reference [111].

Chapter 5

Bulk chalcogenides: Vestiges of Broken Symmetry and the Associated Midgap Electronic States

5.1 Overview

We explicitly demonstrate that the diverse structures formed by the family of chalcogenide alloys Pn_2Ch_3 from Fig. 1.8 can be thought of as symmetry broken version of *parent* structures defined on a much more symmetric, simple-cubic (SC) structure. Distorted octahedral coordination is characteristic of the chalcogenides. By

tracing the actual Pn_2Ch_3 structures to the SC structure, we are able to identify quasi-linear atomic motifs that underly the formation of special midgap electronic states that have been argued by Zhugeyevych and Lubchenko [8–10] to account for the mysterious light-induced phenomena in in *amorphous* chalcogenides. The latter materials are a leading candidate for the next generation non-volatile computer memory.

5.2 Chalcogenides as symmetry broken versions of symmetric parent structures

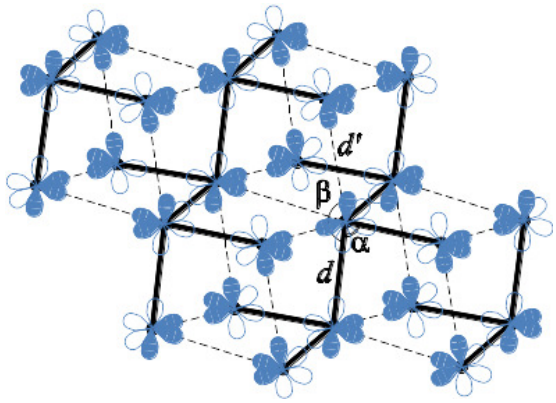

Figure 5.1: Cartoon p orbitals superimposed on the rhombohedral lattice for arsenic using the network of $pp\sigma$ bonds to illustrate the system of intersection chains model. On the lattice d and d' indicate the covalent and secondary bond lengths respectively, angles α and β show the deviation from simple cubic geometry, $\alpha \neq 90\,\text{deg}$ and $\beta \neq 180\,\text{deg}$

The notion of quasi-one-dimensional, chain-like motifs in the chalcogenides materials is motivated by the structure rhombohedral arsenic, which is indeed composed

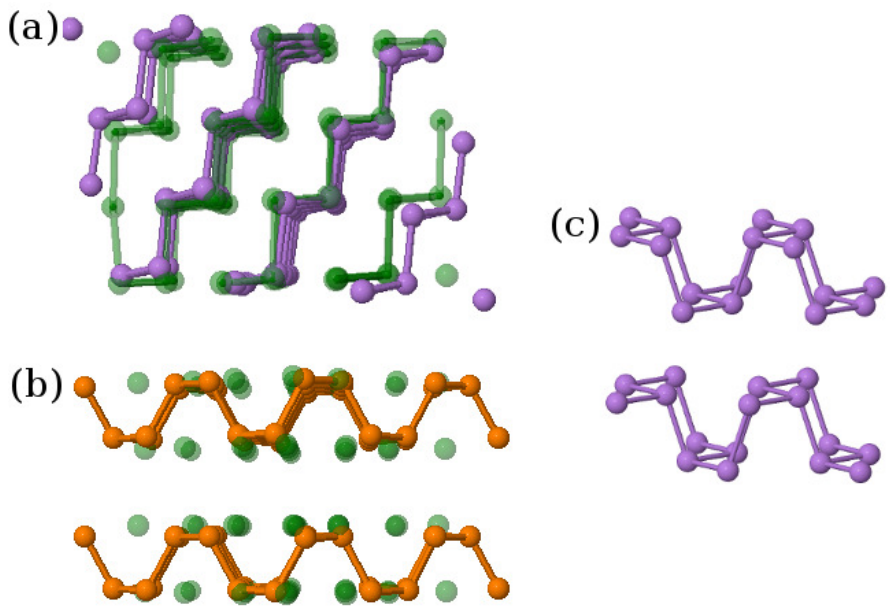

Figure 5.2: Covalent bonding example of parent structure authority. Panels (a) and (b) show elemental As and P relaxing to their native A7 and A17 structures respectively, from the parent structures shown in green. Panel (c) shows As in the metastable black phosphorus as a result of relaxation from the A17 parent structure.

of intersecting, modestly interacting chains. This is illustrated with the help of cartoon p orbitals on the rhombohedral lattice in Figure 5.1. That the rhombohedral lattice in the latter figure is a lowered-symmetry version of a parent structure defined on a simple-cubic lattice is demonstrated in Fig. 5.2.

Similarly to elemental arsenic and isolelectronic compounds from Fig. 5.12, parent structures can be devised for the compounds from Fig. 1.8. These parent structures are shown in Fig. 5.3. Like orpiment, the stibnite lattice has double layer features in the form of finite width *ribbons*. Single layers of the double layer ribbon feature are composed of intersecting symmetry broken pentamer units as shown in Figure 5.5. The slab features in the tetradymite structure of Bi_2Se_3, shown in panel (d) of

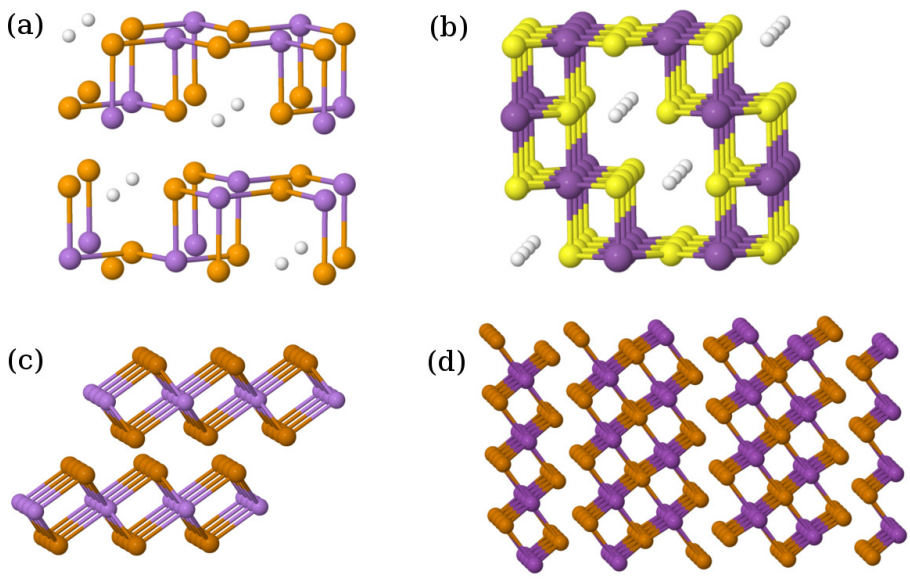

Figure 5.3: Simple cubic parent structure candidates for all four lattice types found in the group 15-16 binary intermetallics compounds.

Figure 5.8 are built up from only slightly symmetry broken pentameric units as shown in Figure 5.6. The broken symmetry in these 5 atom units is highlighted by the addition of dashed bonds to identify the secondary bonds. The symmetry broken pentameric units in the arsenic telluride crystal structure are identified in the isolated chains shown in Figure 5.7, it appears that the chain patterns of both panels (2) and (4) of Fig. 5.8 are represented in the longest chain segment. This feature may be the root of additional multiplicity.

The most important consequence of the existence of parent structures defined on the simple-cubic lattice is that such parent structures are all composed of one-dimensional chains; we have seen the chains are generally not contiguous. Zhugayevych and Lubchenko have demonstrated that when odd-numbered, such chains must host special midgap states. We have encountered the simplest examples of such midgap

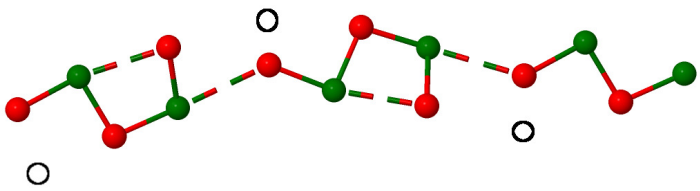

Figure 5.4: 1D chain patterns identified in the orpiment crystal structure of As_2Se_3. Double layers in orpiment structure are composed of roughly perpendicular *ladder* patterns like the one shown here. The parent structure for As_2Se_3 developed by ZL contains vacancies. Notional vacancies in the crystal structure are indicated by hollow circles. Pentameric units in As_2Se_3 are terminated by vacancies, only a single 5 atom chain is visible in this small sample.

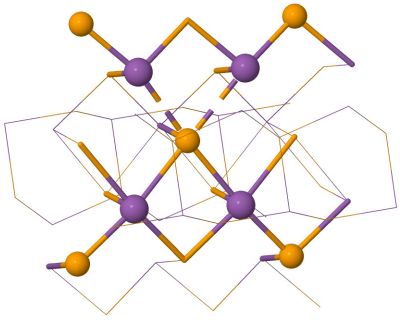

Figure 5.5: 1D chain patterns identified in a double layer of the stibnite crystal structure of Sb_2Se_3. The symmetry broken pentameric units shown have the trimer-dimer pattern identified in panel (2) of Figure 5.8.

already in the trimeric units from Chapter 2. Given a finite sample consisting of modestly interacting chains, such midgap states can generated according to the procedure [10] graphically illustrated in Fig. 5.9.

The above procedure can be implemented chemically by passivating a finite sample so that the desired chain in odd-numbered. This is illustrated for a central chain in a 3x3x5 rhombohedral arsenic cluster, is shown on the right in Figure 5.9. The

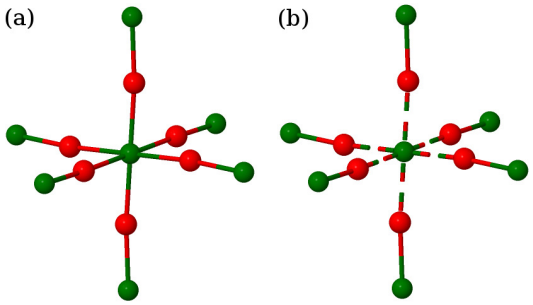

Figure 5.6: 1D chain patterns identified in the tetradymite crystal structure of Bi_2Se_3. Apparently octahedral coordinated structure in panel (a) is only slightly symmetry broken as shown by identification of slightly weaker *secondary* bonds in panel (b). This coordination corresponds to the chain dimer-monomer-dimer pattern identified in panel (3) of Figure 5.8

resulting electronic structure, following optimization in shown in Fig. 5.10. We observe that the midgap state is robustly located close to the center of the forbidden gap.

Amorphous materials are characterized by a vast multiplicity of free energy minima that scales exponentially with the sample size. [7, 116] This multiplicity gives rise to a separate contribution to the overall free energy of a glassy liquid; it exhibits itself through the excess liquid entropy of a the liquid relative to the crystal. Each such minimum corresponds with a relatively low energy, high-density structure. Wolynes and coworkers [7,116] have established that in finite dimensions, structures corresponding with indvidual free energy are of finite extent, a couple nanometers across, and co-exist spatially. The interfaces between these relatively low-free energy structures, often called domain walls, are relatively strained. Our finite samples are proxies for the domains, while the free surface approximates the domain wall. It is at the domain wall where the crystal-like alternation of bond strength is most

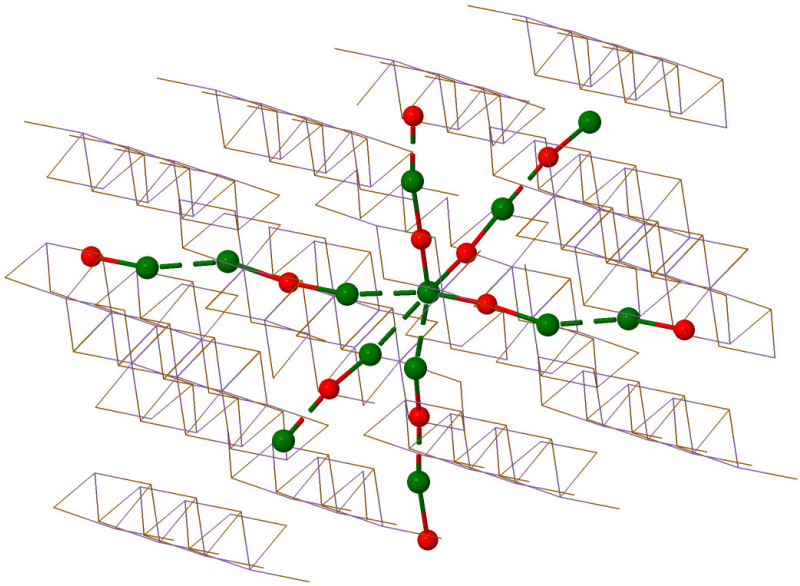

Figure 5.7: 1D chain patterns identified in the Gd_2Cl_3 crystal structure of As_2Te_3. This coordination corresponds to the chain trimer-dimer pattern identified in panel (2) of Figure 5.8

likely broken. In Fig. 5.12, we show how the surface passivation of a modestly-sized crystalline sample of As_2Se_3 leads to the emergence of a midgap state, despite the presence of vacancies. The midgap state persists despite the evident amorphization of the sample. These results are a significant improvement over the idealized situation in Fig. 5.11 since elemental arsenic is not a good glassformer, whereas As_2Se_3 vitrifies readily.

Consistent with the Rice-Mele [117] model and the previous work of ZL [118], the charged midgap state occupied by two electrons (or two holes) is stabilized (destabilized) with respect to the singly occupied neutral state. The midgap state is the highest occupied level, so adding an extra charge to the cluster (or depleting one) should populate (depopulate) this state. An external +1 charge is equivalent to

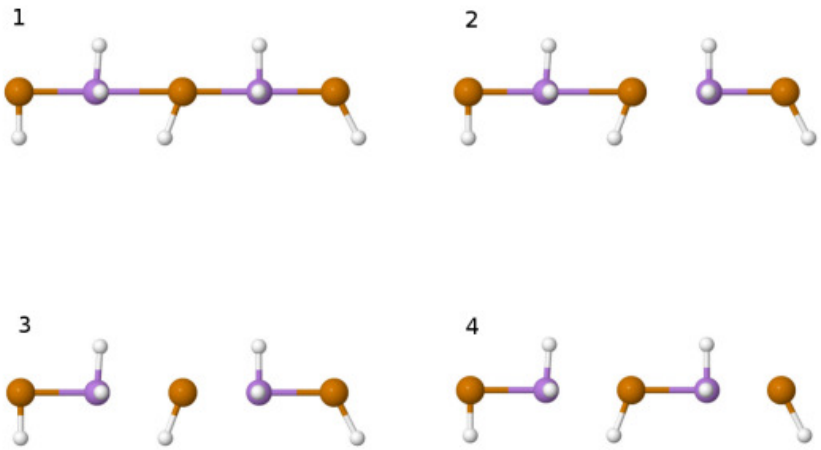

Figure 5.8: Progression of symmetry breaking in a Te-As-Te-As-Te five atom unit under uniform dilation, starting from high density symmetric pentamer (1) through dimer-monomer-dimer motif (4).

adding an extra *hole* to the formally unoccupied state. Figure 5.13 shows the shift to the under-coordinated (UC) and over-coordinated (OC) midgap state energies owing to the external charge, based on HF solutions at the MOPAC PM6 level.

We confirm the prediction of the singly occupied, paramagnetic midgap state using just the density matrix elements with $S = 1/2$ from a MOPAC restricted open-shell HF solution. Variation along the chain (z) axis is shown in Figure 5.14, elements off the chain axis were negligible, so no x and y dependence is shown. Visual inspection shows that the unpaired spin density mirrors the wavefunction amplitude for the midgap state along the central chain.

Figure 5.12 in Chapter 1 illustrated how even in the the near-crystal geometry

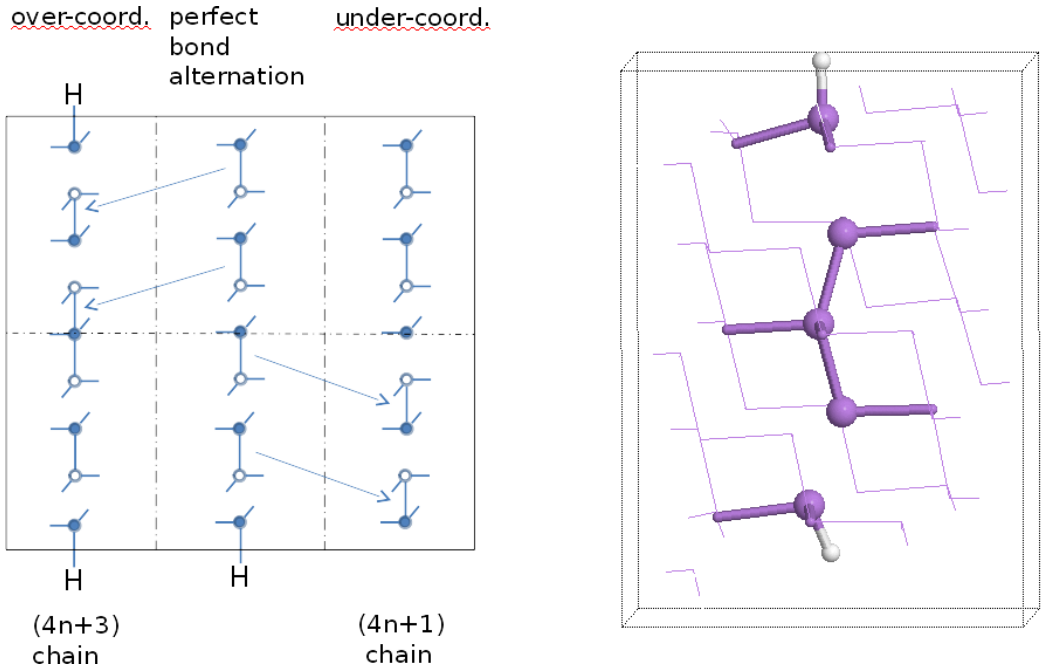

Figure 5.9: Individual chain defect prescription for an elemental material with dimerized chains such as arsenic. Arsenic cluster on right shows H addition prescription applied to form an over-coordinated defect on central chain.

of a modest size arsenic selenide cluster, the act of addition/removal of passivating hydrogen on the chain relaxed chain structure will change the resident charge density wave sufficiently to produce a midgap state, even though no formal coordination defect was introduced. Ideally, a similar defect would be planted in the parent structure so that a legitimate amorphous structure is allowed to evolve under geometry optimization. Here, some crystal field influence undoubtedly remains in addtion to reconstruction effects from the large surface area in proportion to the cluster volume. To show that we can tame the surface effects, geometry optimization of a 384 atom arsenic selenide cluster was performed using NWChem. Figure 5.15 shows the final geometry.

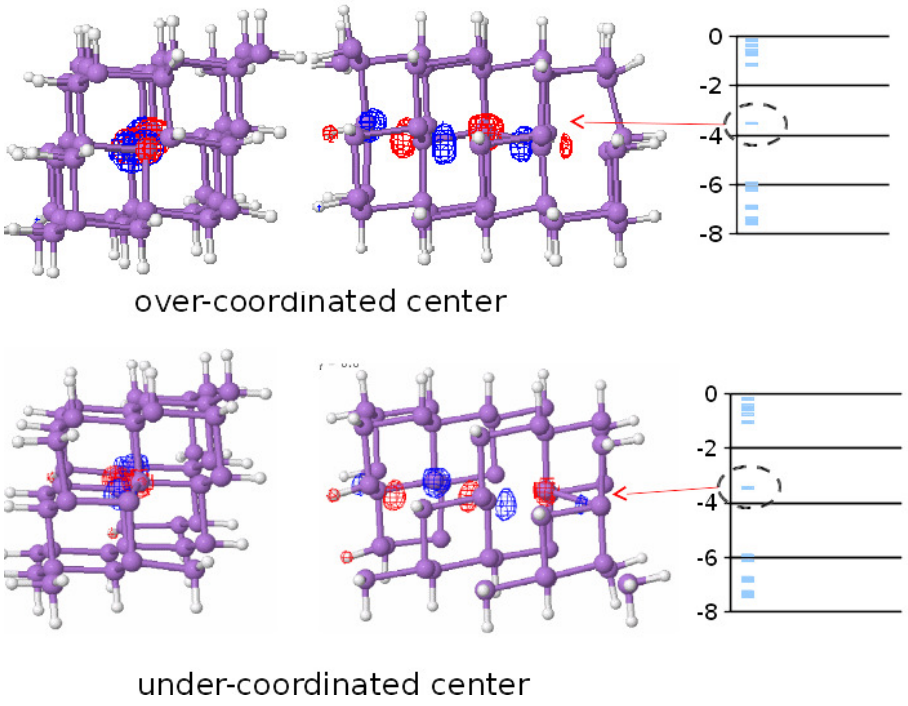

Figure 5.10: The results of over and under-coordinated defect stimulation on a single central chain in a small arsenic cluster following geometry optimization with the MOPAC PM6 method. The actual spectrum for each cluster is shown on the right, units for the vertical energy axis are (ev). The dashed outline identifies the defect associated midgap state in each case.

The volume of this arsenic selenide cluster is now large enough so that the ground state is determined by the symmetry broken molecular chains. We intend to break discrete symmetry along one chain unit in the parent structure and obtain amorphous structure under geometry optimization. Per the coordination defect prescription in Fig. 5.9, trimming a terminal hydrogen sets up an over-coordination defect. For reasons of computational efficiency, we choose a slightly larger cluster size in order to have an odd number of electrons in the system before stimulation of the defect, so that removal of one H results in an even numbered system. The open-shell and restricted open-shell Hartree-Fock methods applicable to odd numbered systems will

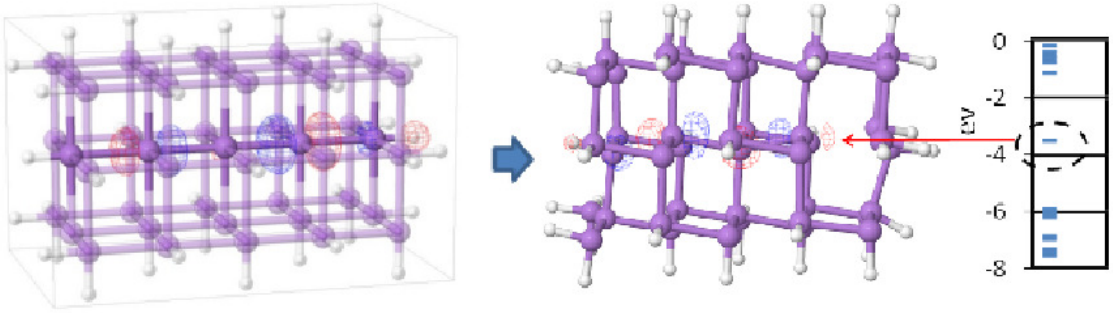

Figure 5.11: Prototype process for generating coordination defect and associated midgap state in an elemental solid, where relaxation of H passivated parent structure leads to electronic midgap state shown in spectrum on right.

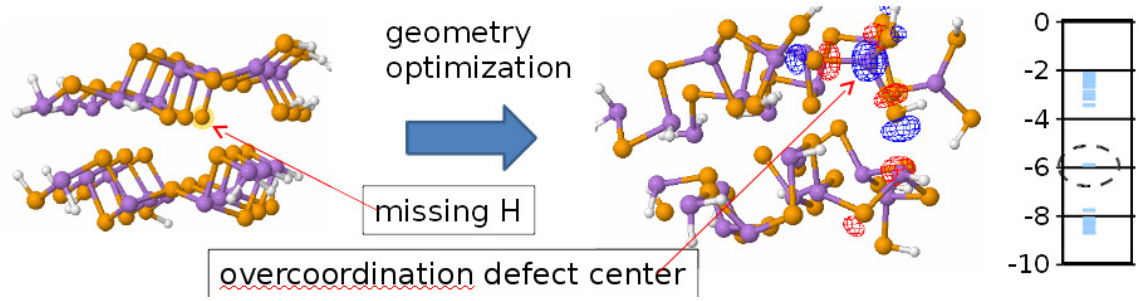

Figure 5.12: A malcoordination stimulated within a single plane layer of As_2Se_3 by removing a passivating hydrogen to shift the CDW on that pentameric unit to the complementary pattern to break symmetry. Units for the spectrum shown on the right are electron-volts.

require more computational resources than we have access to at this time.

An over-coordination defect can be considered as a midgap state occupied by two holes, and is predicted to be destabilized with respect to the charge neutral singly occupied midgap state. [111] The cluster in Figure 5.16 was optimized to the extent that our compute allocation on the Stampede cluster would allow, it did not reach an energetic minimum but there is enough encouraging information present to warrant discussion here. There is evidence that our double chain notions for parent

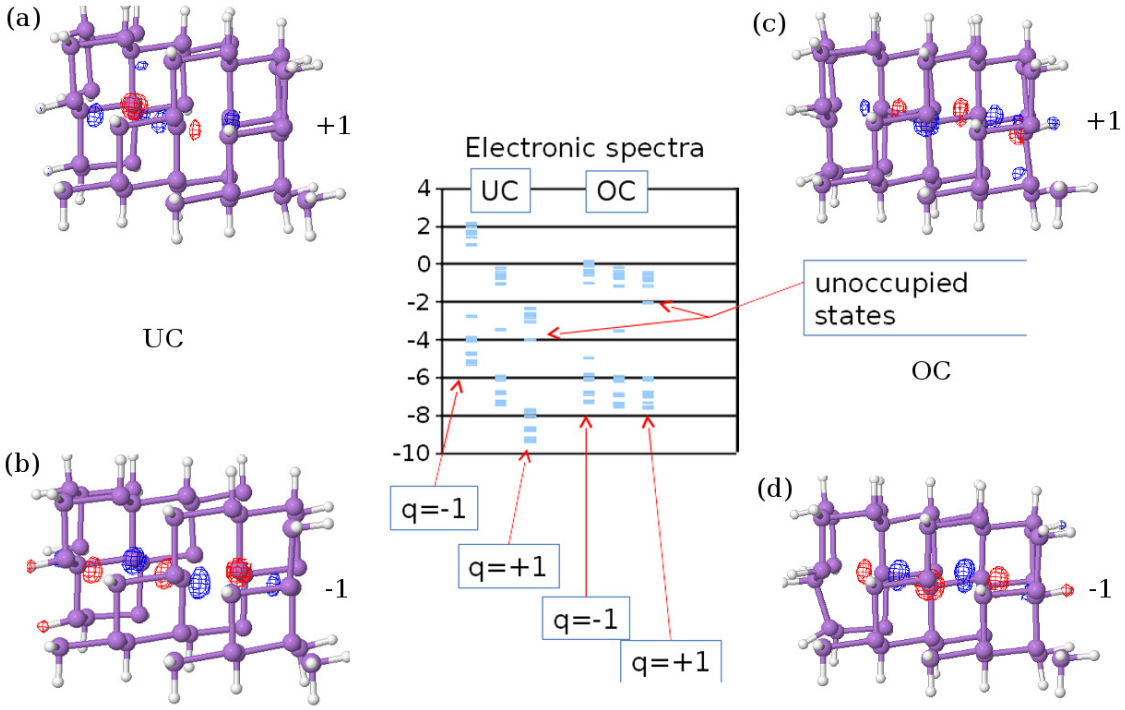

Figure 5.13: Relative energy shifts of the midgap state in response to externally imposed double occupancy. Under-coordinated charged states and their associated geometries are shown in panels (a) and (b). Over-coordinated charged states appear in panels (c) and (d). Energy units for the spectra in the central panel are (ev).

structures that contain vacancies is correct, a midgap state has been excited in the spectrum and it's destabilization is in the direction predicted. Examination of the majority contributor basis functions in the midgap state shows that they are As or Se p functions from atomic orbitals on the chain structure in panel (c) of Figure 5.16. Upon resumption of the geometry optimization process, the makeup of this electron state will evolve, but the presence of these functions early on is what we expect. A negative finding here would effectively rule out the coordination defect scheme applicable to all parent structures with vacancies, which is about half of the nine intermetallic compounds.

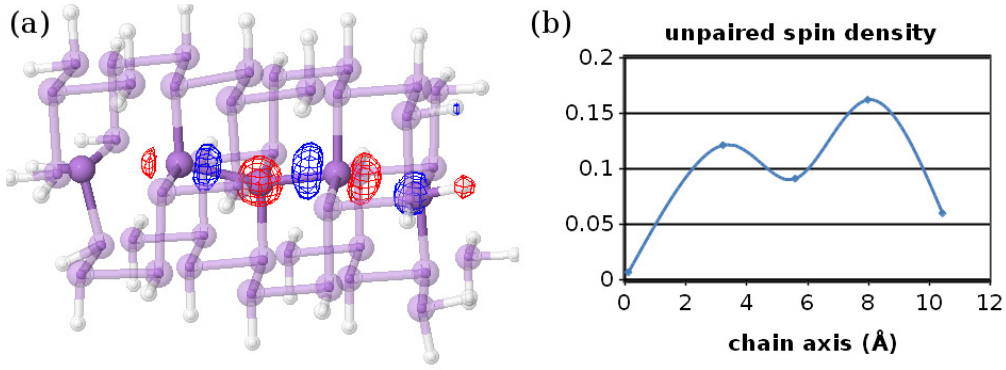

Figure 5.14: Unpaired spin density in an over-coordinated cluster of elemental arsenic. Spin density units derive from a sum over ψ^2 quantities, so they are dimensionless.

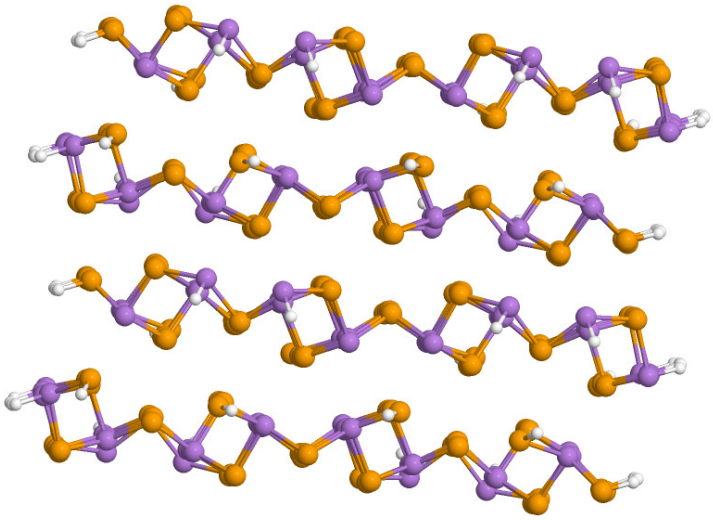

Figure 5.15: Hydrogen-passivated arsenic selenide cluster, following geometry optimization using NWChem HF method with a double-zeta basis set. Good agreement with crystal coordination is evident in the interior along with only a modest amount of surface reconstruction.

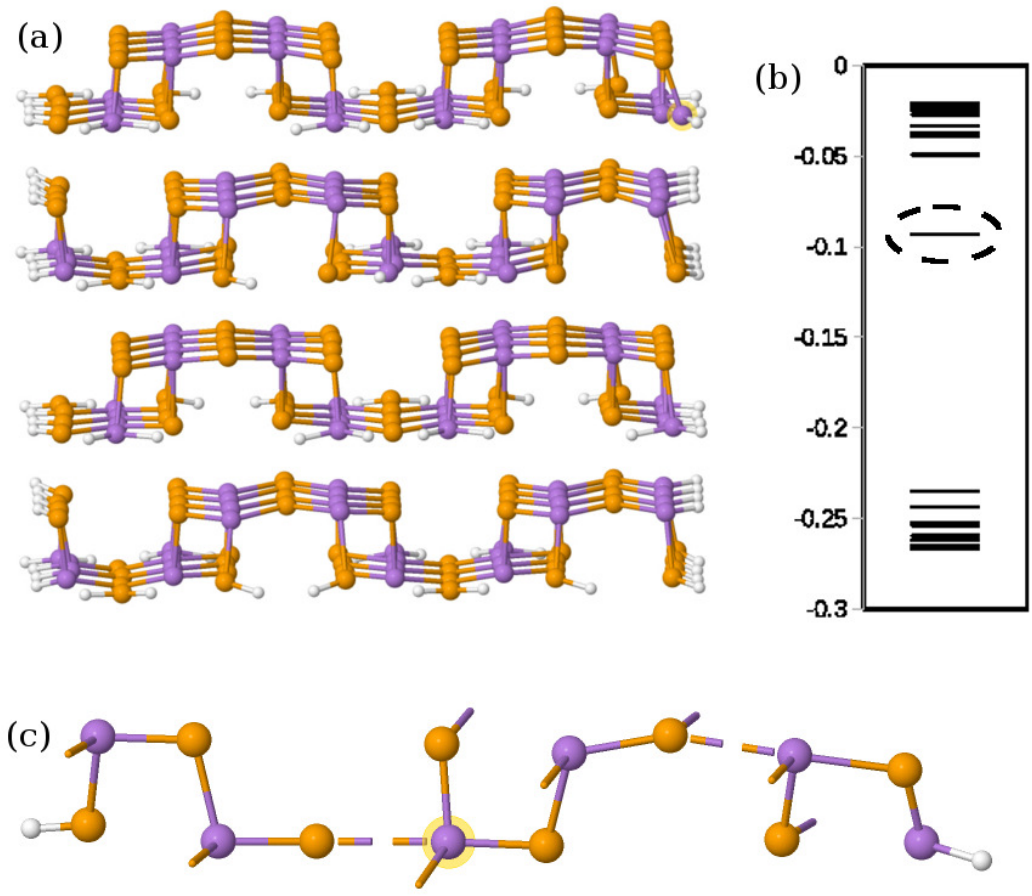

Figure 5.16: The hydrogen-passivated arsenic selenide parent structure shown in panel (a), following limited geometry optimization using the NWChem HF method with double-zeta basis set. Highlighted atom at top right has one passivating H removed to stimulate an over-coordination defect on the diagonal double chain structure as shown in panel (b). Panel (c) shows a portion of the cluster spectrum, energy units for the vertical axis are ev, the dashed line ellipse identifies the defect associated midgap state.

Chapter 6

Summary and Future Work

This work views distinct chemical interactions as mediated by electrons that are localized to a distinct degree. The classic ionic interactions are mediated by electrons that are fully localized. Metallic bonding is accomplished by itinerant electrons. In the continuum limit, such itinerant electrons exhibit full translational symmetry, which is lowered in the presence of the nuclei. For the localized electrons, the translational symmetry is fully broken. We have shown that electrons with differing degrees of localization exhibit phase-ordering behaviors similar to those characteristic of classical particles. The emergence of localization in both systems is a result of *symmetry breaking*. In contrast with classical systems, the breaking of translational symmetry for electrons could be either continuous or discontinuous, depending on the density. The emergence of energy bands and the possibility of conductivity in the present of stationary nuclei is an intrinsically wave-like phenomenon that we associate with quantum mechanics. The other significant feature that makes the

quantum case distinct from classical systems is that the interfaces between distinct patterns of charge-density waves, in the insulating regime, must host very special midgap electronic states that happen to quantitatively account for the mysterious light-induced anomalies in amorphous chalcogenide alloys.

In the present approach, the coexistence of ionic and metallic interactions corresponds with the multicenter bond, the simplest example provided by the three-center four-electron bond. At sufficiently low density, yet another symmetry lowering takes place by which the multi-center bond gives rise to a coexistence of the covalent and a closed-shell, secondary bond. We have shown that the symmetry breaking associated with the transition from multi-center to covalent/secondary interactions exhibits universality expected of critical points, whereby the detailed interactions enter the description though a very small number of parameters. As a result, the bonding near such critical-like points becomes subject to a law of corresponding states.

The spatial symmetry breaking within the three-center bond can be rationalized as an interplay between the cohesive interaction mediated by the valence electrons and the repulsion due to the ionic cores. This is quite similar to how the symmetry breaking in classical systems comes about as an interplay between cohesive and entropic forces. A Landau-Ginzburg expansion can be written down and fits the data well. The molecule's electronic structure favors distortion, but the molecule can be symmetries given the repulsion between the ionic cores is sufficiently strong. The electronic structure was found not to be driven by stabilization of the molecular orbitals near the HOMO-LUMO gap as in the Jahn-Teller mechanism, but instead it resulted from $s-p$ mixing in the lowest lying filled orbitals. We illustrated how the bonding

electron count, a common quantity used especially in coordination descriptions for intermetallics, must be determined self-consistently as a function of density, lone pairs serving as either sources or sinks for bonding molecular orbitals. At the trimer level we find a purely electronic transition that occurs well upstream of any spatial symmetry breaking; this transition was shown to be suppressed with increasing electronegativity variation between the central and terminal atoms, a finding consistent with the model for the 4-electron/3-center bond. We argued that the increasing prevalence of hypervalent coordination observed as one travels down a group in the periodic table stems from the decreasing separation between the maximum charge density radii for the outer filled d shell and valence p orbitals, the increased steric repulsion serving to stabilize the symmetric state. We have developed a method to treat electronegativity as a parameter that can be varied continuously, in order to construct a phase diagram of chemical interactions. The phase diagram is built in the plane defined by the electronegativity variation ε and mass density ρ. Construction of the high density metallic and ionic sectors revealed hysteretic behavior, which was ultimately tied to term crossings of degenerate molecular wavefunctions. This finding prompted the subsequent study of the degeneracy of charge density waves.

It is hoped that with the present framework, the complex behaviors of electronic liquids can be greatly simplified by using judiciously chosen density functionals motivated by *classical* charge-density functionals. We have seen such simplification is indeed possible so long as one is mindful that electronic systems can exhibit phenomena that are intrinsically quantum. These include the possibility of a continuous metal-insulator transition and the special midgap electronic states.

Where the structure of a material can be thought of as resulting from a symmetry-lowering distortion of a higher-symmetry parent, uniform density changes drive a purely electronic transition, consisting of an abrupt change in bond order and the number of bonding electrons. This takes place despite only modest changes in the canonical molecular orbitals and bond lengths. This electronic symmetry breaking always warns when a structural instability is close by, even if spatial symmetry remains unbroken. In the molecular examples we considered, there were always two alternative ways to assign the available set of two-center bonds, the solid-state examples suggest that the multiplicity of two-center bond patterns or bond order waves is much higher.

The hysteretic behavior observed at high densities on simple and body-centered cubic lattices where *metallic* molecular wavefunctions were found to persist well into the phase diagram sector where *ionic* solutions are found, prompted to test a proposal that the miscibility between delocalized and localized electronic states is analogous to the issue of phase co-existence and, further, the issue of miscibility of distinct substances. Using a simplified tight-binding Hamiltonian we have showed that with an interaction potential consisting of Coulomb and polarization terms both first- and second-order transitions are possible where metallic and insulating phases of electronics states coexist. True to the oil-and-water miscibility notion, the degree of mixing between these states is tied to their relative polarizabilities. Coexistence is essential to the idea where a defect associated midgap state *interpolates* between two distinct charge density waves.

We have extended the defect stimulation scheme developed by ZL [8,10] for chain

structures to molecular clusters and demonstrated how over and under-coordination defects lead to analogous midgap state in solids. We have generated both charge neutral and charged midgap states in 3D elemental arsenic samples, to confirm the stabilization (destabilization) of these states when occupied by two electrons (holes), suggested by ZL's earlier work. The 1D symmetry breaking behavior described in Chapter 2 has been extended to the fundamental pentameric units that make up the binary pnictogen/chalcogen compounds with Pn_2Ch_3 stoichiometry to reveal how three basic symmetry broken chain geometries emerge from the symmetric pentamer under dilation. With this chain framework, we have synthesized simple cubic parent structures for the four crystal structures found in these group 15/16 compounds, that support the coordination defect generating scheme successfully applied to elemental arsenic solids.

Following optimization of the MOPAC PM6 As and Se basis functions for the compound As_2Se_3, we have obtained the crystalline geometry by relaxation from the simple cubic parent structure. This optimized basis set was used on a large 384 atom H passivated As_2Se_3 cluster to confirm that near-crystalline geometry is in fact the energetic minimum in the absence of periodic boundary conditions. This result also showed that free surface effects can be tamed with a sufficiently large cluster. Using the optimized As and Se basis functions we stimulated a coordination defect in a modest sized As_2Se_3 cluster and confirmed the midgap state following MOPAC geometry optimization. This result was confirmed in an HF optimization in NWChem using the $cc-pvdz$ basis and small-core pseudo-potential. Attempts to relax a large 384 atom defect-containing As_2Se_3 cluster to a representative amorphous

geometry have been stymied in both MOPAC and NWChem calculations by the sheer size of the problem.

Convergence difficulty in MOPAC encountered early in the optimization process are believed to stem from degeneracy associated with the slightly symmetry broken parent structure as no such problems occur for crystalline geometry of the same size. Although the NWChem HF procedure converges reliably, calculation of the two-electron integrals is a severe bottleneck that effectively precludes the use of this method for relaxation of the parent structure, even on the largest computer clusters. The two-electron bottleneck may be avoided using a local exchange-correlation functional in the density functional theory method, but DFT is known to underestimate the HOMO-LUMO gap which leads to convergence problems in these intermetallic compounds, especially on slightly symmetry broken parent structures with near degeneracy. Future work in this area will determine whether more severely broken symmetry in the parent structure will lift the troublesome degeneracy suspected in MOPAC and DFT calculations. The PM6 basis optimized to give the correct coordination may not be the best choice for the initial relaxation of the sample, although the latest PM7 MOPAC basis does not give the correct geometry, it proceeds in the direction of crystal geometry quickly, so it may be possible to reserve the optimized basis for final corrections, after PM7 brings the solid within reach of crystal structure. The best approach will probably be a combination of the two methods, using the efficient MOPAC semi-empirical method for geometry optimization followed by a gradient check in NWChem HF or DFT to confirm that the resulting geometry is the actual minimum. Out of the nine potential binary Group 15/16 compounds,

only PM6 basis sets for As_2S_3, As_2Se_3 and As_2Te_3 have been satisfactorily optimized, with all success coming from a simple line-search method.

Appendix A

Appendix

A.1 Potential energy of the AsH_2-AsH-AsH_2 trimer

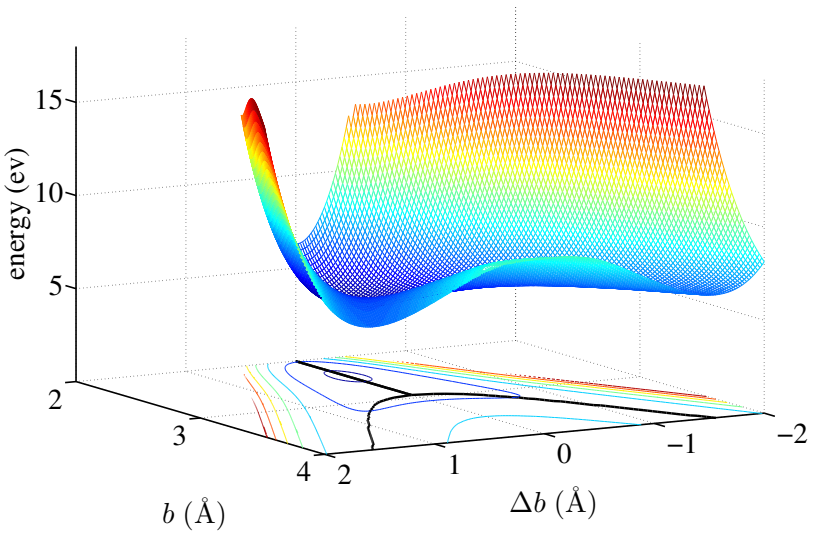

Figure A.1: Potential energy surface for 3/4 trimer AsH_2-AsH_1-AsH_2 as a function of central atom displacement and the chain length per bond. Minimum energy contour shown in bold to highlight symmetry breaking.

A.2 Fluctuation-induced lowering of the symmetry breaking

The energy surface produced by MOPAC and NWChem, such as that in Fig. A.1, gives the zero-temperature location of the nuclei in the *classical* limit. Already zero-point vibration will be sufficient to overcome the barrier separating the two minima on the symmetry broken energy surface, if the barrier is sufficiently low. For the sake of concreteness, we consider the symmetric stretch of the trimer. A harmonic oscillator with frequency ω and mass m of exhibits zero-point vibrations of magnitude [61]

$$x_{T=0} = \left(\frac{\hbar}{m\omega}\right)^{1/2}. \tag{A.1}$$

For a quadratic potential whose force constant κ matches the curvature of a symmetry-broken minimum, $\omega = (\kappa/m)^{1/2}$, where m is the mass of a terminal atom. Next, we find the point below the zero-temperature symmetry breaking such that the vibrational magnitude (A.1) exactly matches the half-width of the barrier separating the two minima, see the graphical explanation in Fig. **??**.

A.3 Lack of promotion of $3d$ electrons

We must check how much the outermost filled d shells are modified following contraction of the trimer, to test whether MOPAC's implicit treatment of the core electrons does not introduce additional error. To this end, we examine the fractional $3s$ and

$3d$ content in a filled $3d$ molecular orbital under compression using an all-electron HF calculation in Orca. [2, 3]

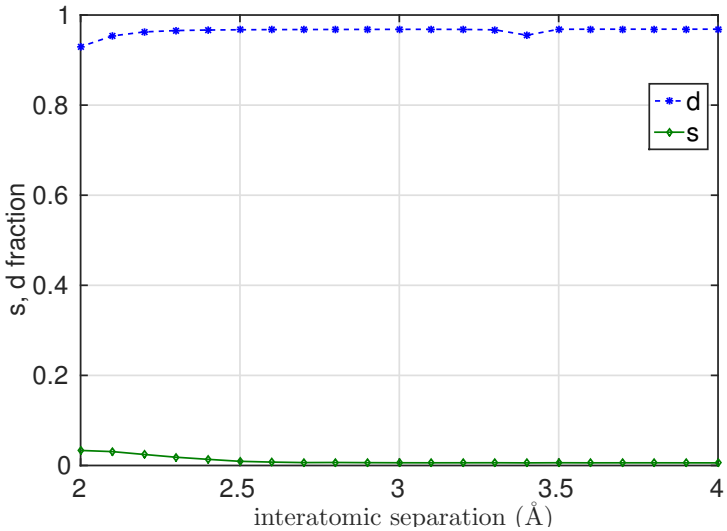

Figure A.2: Fractional contribution of atomic $3s$ and $3d$ orbitals to a molecular orbital of an arsenic trimer, as a function of atomic separation according to an Orca all-electron HF calculation. [2, 3]

A.4 Dependence of symmetry breaking on the $pp\sigma$ bond electron count

A.5 Electronegativity variation suppression of the electronic transition

Several molecular examples are considered in Figure A.4 representing a range electronegativity difference between the central and terminal atoms spanning zero to

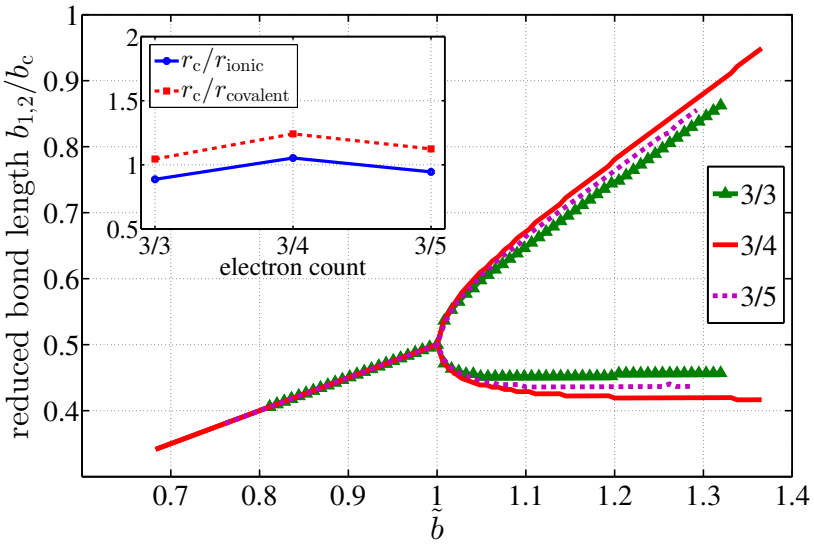

Figure A.3: Dimensionless reduced bond lengths for three arsenic trimers, AsH_2-AsH_n-AsH_2 trimer, as functions of the overall dimensionless trimer length per bond, $\tilde{b} = (b_1 + b_2)/2b_c$. The three cases, $n = 0, 1, 2$, correspond to a five, four, and three electron $pp\sigma$ bond, respectively. Both axes are scaled by the corresponding critical bond length b_c.

nearly 2 ev. To offset the effects of atomic number and ion size on the actual transition location, we have normalized the difference between the spatial and electronic critical lengths by the spatial critical length $b_c^{(\text{spatial})}$ pertinent to each molecule.

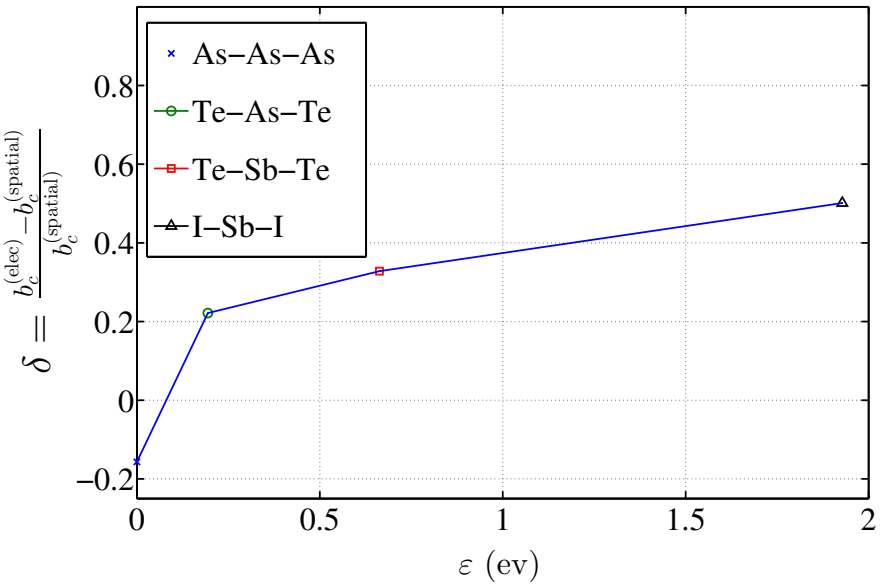

Figure A.4: Dimensionless separation length δ between the electronic and spatial transitions, normalized by the critical bond length $b_c^{(\mathrm{spatial})}$ to suppress to the atomic number and size influences, shown as a function of electronegativity variation ε between the terminal and central atoms.

A.6 Dependence of symmetry breaking on the $pp\sigma$ bond electron count

A.7 Effects of electronegativity variation

A.8 Reparametrization of antimony in PM6

MOPAC evaluates the matrix elements of the Hamiltonian using a approximation, in which their coordinate dependence is fully determined by coordinate dependence of the overlaps of the corresponding (atomic) basis orbitals. Figs. **??-??** show the

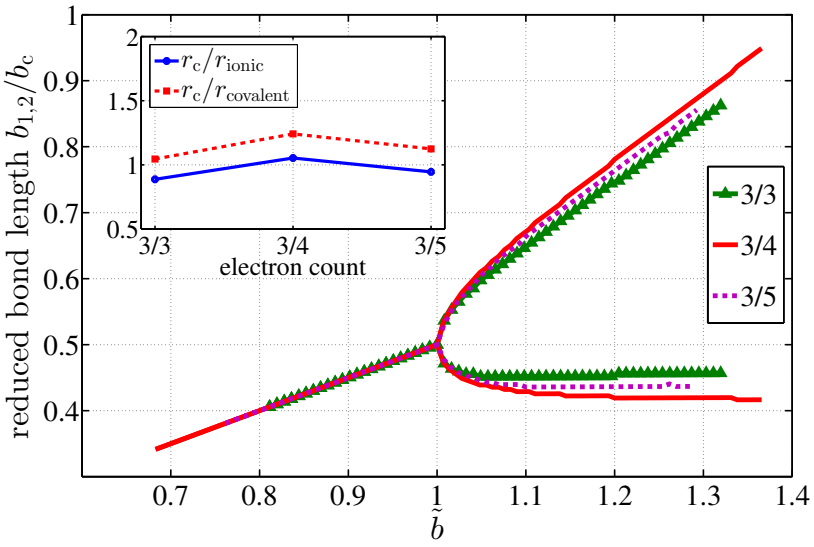

Figure A.5: Dimensionless reduced bond lengths for three arsenic trimers, AsH_2-AsH_n-AsH_2 trimer, as functions of the overall dimensionless trimer length per bond, $\tilde{b} = (b_1 + b_2)/2b_c$. The three cases, $n = 0, 1, 2$, correspond to a five, four, and three electron $pp\sigma$ bond bond, respectively. Both axes are scaled by the corresponding critical bond length b_c.

wavefunction overlaps involving the pseudo-antimony with itself and with arsenic compared with MOPAC's built-in As-As overlaps. MOPAC uses Slater-type orbitals. The quantity ξ refers to the orbital exponent that determines the decay of the wavefunction overlap.

A.9 Re-parametrization of MOPAC PM6 basis set under pressure

MOPAC employs one, Slater-type wave function per atomic orbital whose extent has been optimized to match geometries and formation enthalpies at normal conditions.

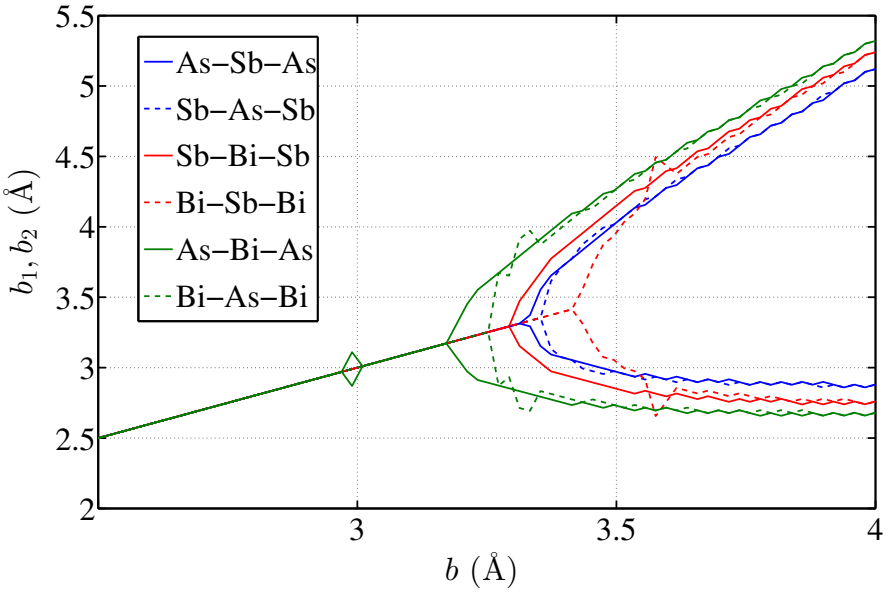

Figure A.6: Bond lengths for several heteronuclear 3/4 trimers XH_2-YH_1-XH_2 and YH_2-XH_1-YH_2, as functions of the overall trimer length per bond.

Such a single-wavefunction parametrization may not be quantitative at high pressures however. We test this by employing a Quantum Chemistry package that employs a linear combination of several five Gaussian Type Functions (GTF) whose widths span a substantial range. We then monitor the coefficients at individual GTF's as functions of density.

Fig. A.12 shows makeup of a p_z atomic orbital in the σ bond along the trimer axis as a function of the As-As bond length. The vertical axis shows the square of coefficients c_1-c_5, one representing the least extended and five representing the most extended function. As the ion cores approach each other, the wavefunction becomes less diffuse; c_3 grows while c_5 shrinks.

How our MOPAC atomic basis functions change with atomic separation will be

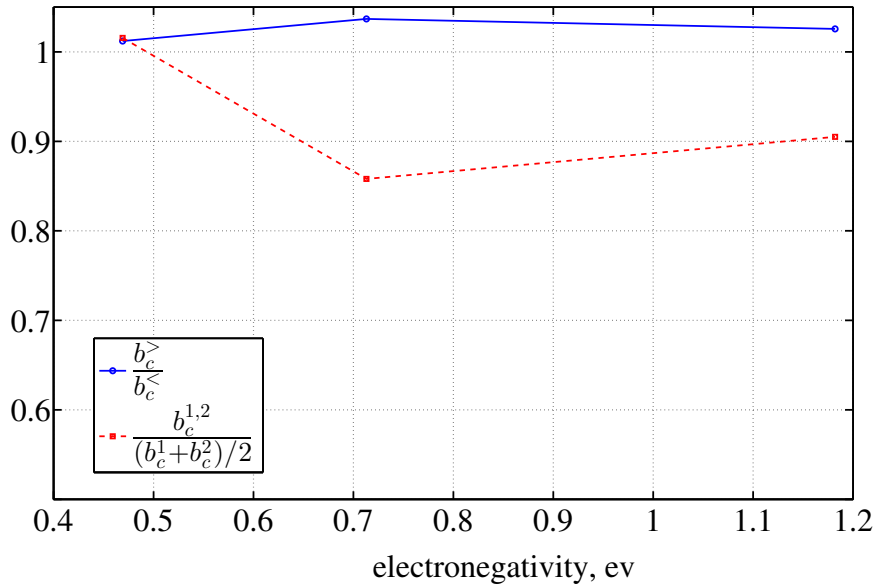

Figure A.7: Critical lengths for the heteronuclear 3/4 trimers XH_2-YH_1-XH_2 and YH_2-XH_1-YH_2 from Fig. A.6. $b_c^>$ and $b_c^<$ correspond to the situation where the more electronegative elements is placed in the central and terminal position, respectively. b_c^1 and b_c^1 denote the critical lengths for the homonuclear trimer XH_2-XH_1-XH_2 or YH_2-YH_1-YH_2.

controlled using the simple empirical function $fz(a)$ shown in Fig. A.13 that is calibrated to experimental values of density and pressure for the simple cubic and bcc phase transitions in elemental arsenic.

Within the MOPAC PM6 method, closed shell Pauli repulsion is approximated with Voityuk's diatomic expression [119]. At close approach, promotion out of overlapping closed shells reduces $4s$ electron density, as a consequence, the steric term should see a decrease. The energy increase due to $4s$ promotion is already captured in the valence-only PM6 method. Undoubtedly in the vicinity of where the pseudopotential was optimized, it's functional form accounts for this. But for large departures from the equilibrium bond length, there should be appropriate scaling of the steric

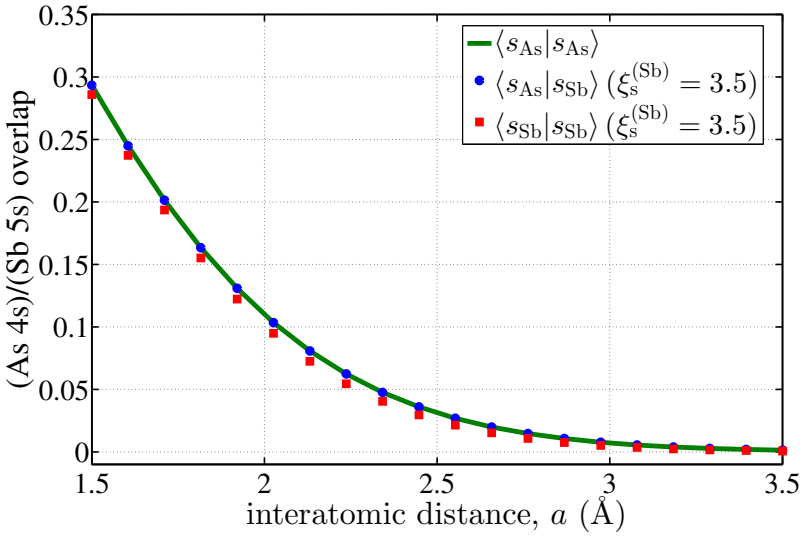

Figure A.8: Overlay of s function overlaps as a function of separation for As-As, As-Sb and Sb-Sb bonds.

repulsion term. In our model, scaling the prefactor χ in the core-core interaction term

$$\chi e^{-\alpha r} \tag{A.2}$$

with a simple function $fx(a)$ (see Fig. A.14) will serve to compensate for promotion of electron density out of the 4s shell.

To calibrate scaling of the STO orbital exponents ζ_s and ζ_p and the core-core parameter χ with nearest neighbor distance a we tune the scaling functions $fz(a)$ and $fx(a)$ to obtain the phase stability of elemental arsenic. Using the common tangent method, a first order simple cubic (sc) to body centered cubic (bcc) transition is verified at 97 Gpa and the experimental volume fraction V_T/V_0 reported in high pressure xray crystallography studies. The continuous transition from rhombohedral to simple cubic at 25 Gpa and experimental V_T/V_0 was confirmed in the susceptibility of

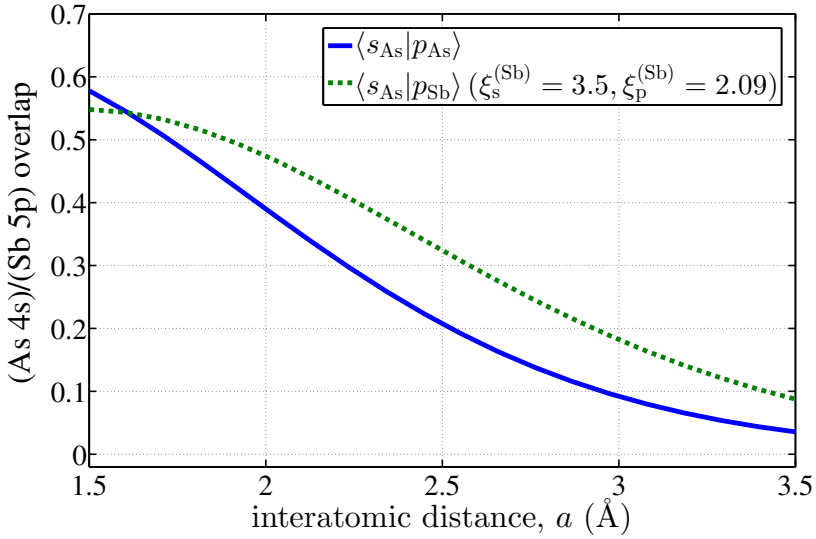

Figure A.9: Overlay of $s-p$ function overlaps as a function of separation for As-As and As-Sb bonds.

the cubic structure towards a rhombohedral [111] distortion. Both scaling functions go to unity at the experimental rhombohedral As crystal density. With the ability to continuously vary the two fundamental parameters, density ρ and electronegativity difference ϵ in our binary arsenic-like material, we will use symmetry breaking to develop a chemical interaction phase diagram, with the help of appropriately chosen order parameters.

A.10 Locating the transition densities for the simple cubic-to-bcc transition

The linear core-core and orbital exponent scaling functions shown in Fig. A.14 and Fig. A.13 were chosen so as to produce the simple cubic to body centered cubic

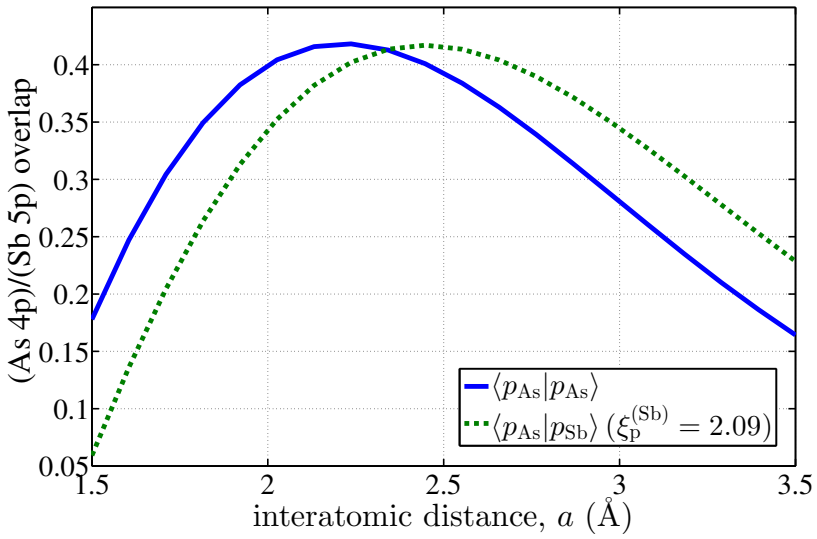

Figure A.10: Overlay of $p-p$ function overlaps as a function of separation for As-As and As-Sb bonds.

phase transition for elemental arsenic shown in Fig. A.15. The phase transition is first order, experimentally there is a coexistence region between the simple cubic and bcc where the structure is thought to be incommensurate. In the absence of information on the pressure dependence of the density within the inter-transition region, we use a simple linear form of the scaling functions in that region.

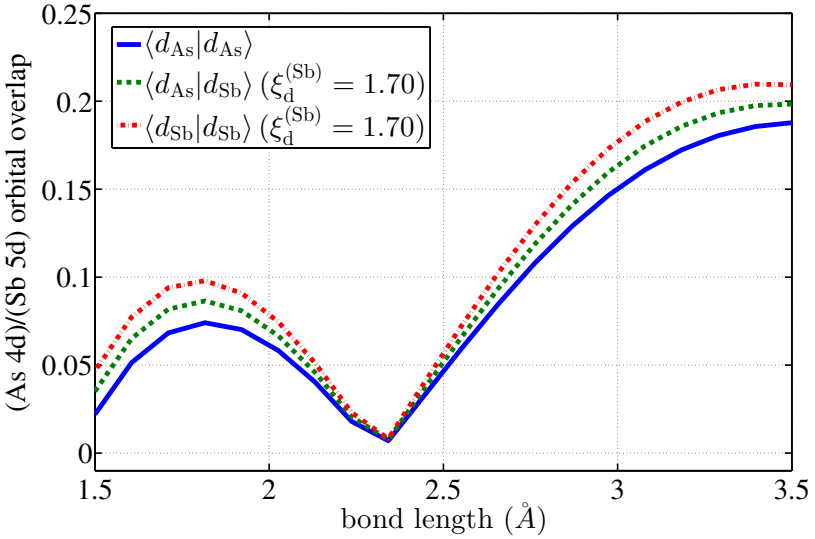

Figure A.11: Overlay of $d-d$ function overlaps as a function of separation for As-As, As-Sb and Sb-Sb bonds.

A.11 Hysteretic behavior of the energy as a function of the electronegativity variation

A.12 Stability of the simple cubic structure to rhombohedral distortion

Fig. A.17 shows the energy of a 64 atom pseudo-arsenic solid on the simple cubic lattice as a small amplitude distortion is applied along the [111] direction to represent the onset of relaxation towards the rhombohedral structure. At the higher of the two densities, the central minimum confirms that the distortion is destabilizing. This is approximately the density where a simple cubic structure is observed experimentally. The lower density curve, with it's non-central minimum confirms our expectation that

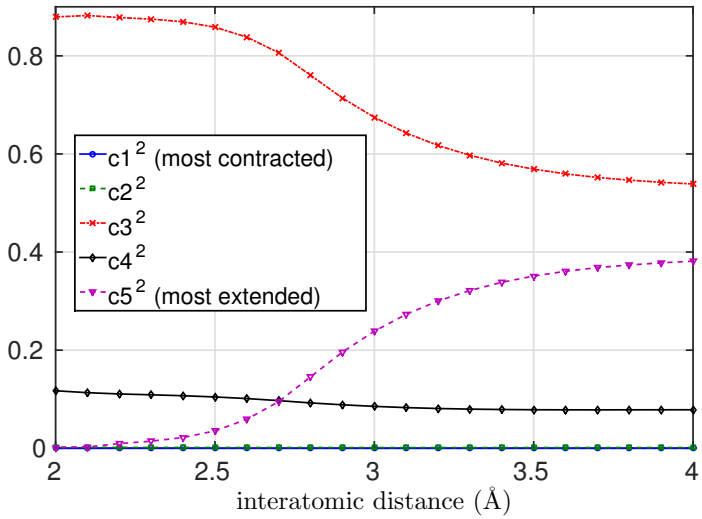

Figure A.12: Composition of the p atomic orbital in $pp\sigma$ bonding MO in arsenic trimer as a function of interatomic separation, from ORCA aug-cc-pvtz all electron HF calculations. Dimensionless amplitude-squared values for the five basis functions represented on vertical axis.

distorted rhombohedral geometry should be favored.

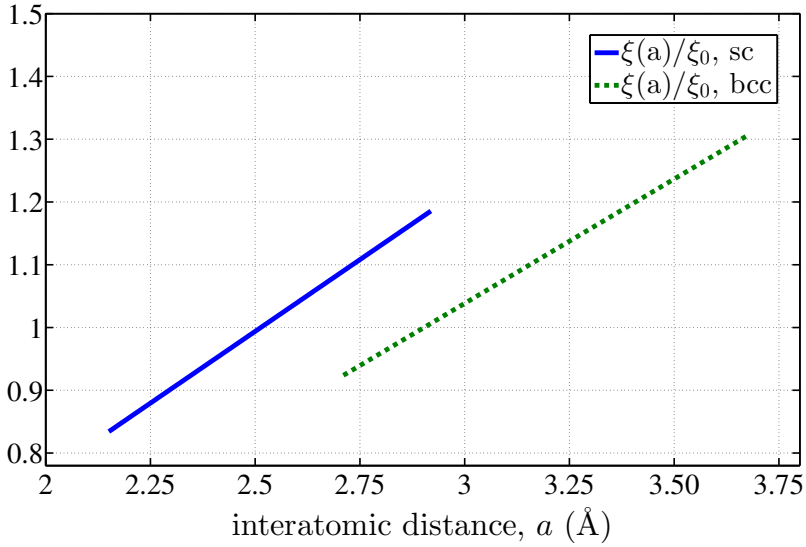

Figure A.13: Orbital exponent scaling function behavior for simple cubic and body centered cubic lattices, illustrated using the ratio of the scaled exponent $\xi(a)$ to the original PM6 value ξ_0, the dimensionless amount of scaling is represented by the vertical axis.

A.13 Ab-initio potential energy surface for the AsH_2-AsH-AsH_2 trimer

A.14 Ab-initio verification of electronic symmetry breaking for symmetric AsH_2-AsH-AsH_2 trimer

HF solution obtained using 6-311G basis. Lack of a multi-center (nC) localized molecular orbital in the analysis table at the top of the figure is one indication of symmetry breaking. Above the transition two equivalent two-center localized orbitals

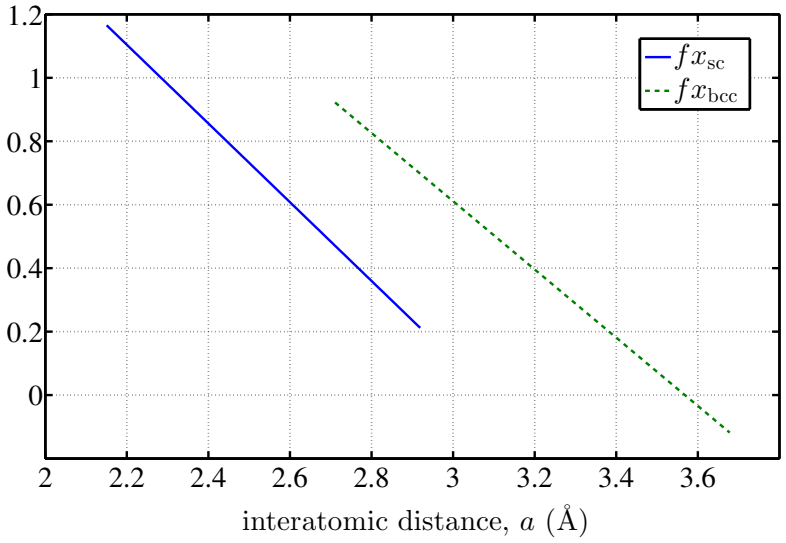

Figure A.14: Linear core-core repulsion pseudo-potential scaling functions for simple cubic and body centered cubic lattices. The amount of dimensionless scaling is represented by the vertical axis.

exist, MO 48 and 50 tabulated in the lower half of Figure A.20

A.15 Absence of MO term crossing during AsH_2-AsH-AsH_2 trimer dilation

A.16 Correspondence between two-center LMOs and spatial dimerization in 20 atom ring molecule

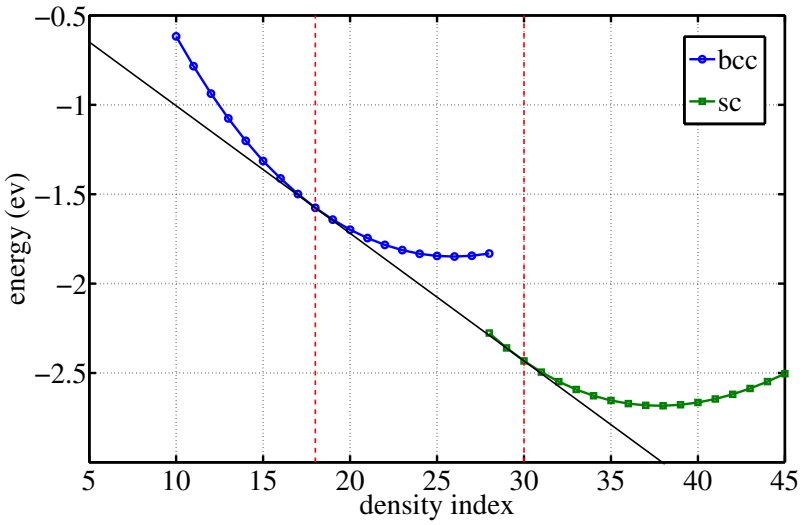

Figure A.15: Maxwell construction determination of the first order simple cubic to bcc phase transition for the pseudo-arsenic material at $\epsilon = 0$. The density index shown on the horizontal axis is an internal variable used in the PM6 calculations to set a common density in both the simple cubic and bcc lattices, the values of 18 and 30 marked with vertical dashed lines correspond to the experimentally observed boundaries of the first order transition.

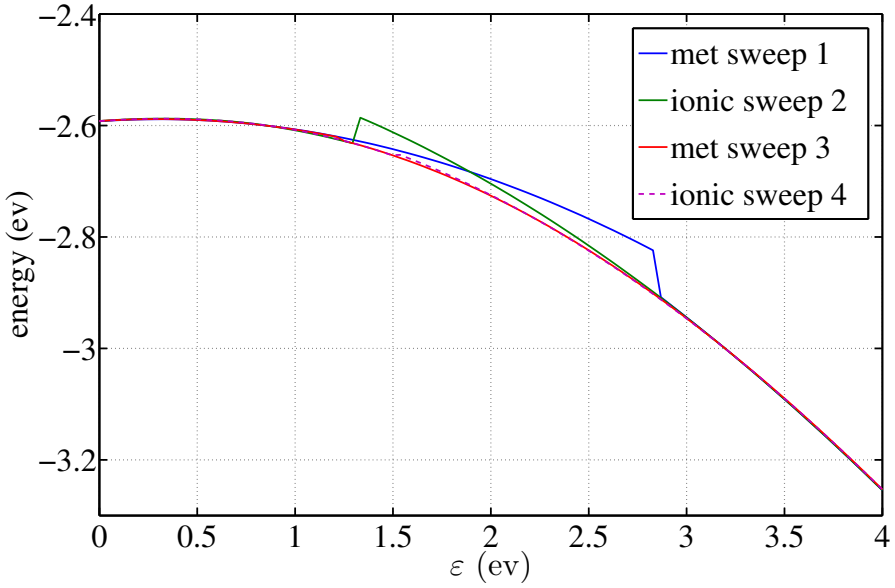

Figure A.16: A sample of the "sweep" protocol demonstrating an overshoot of a term crossing.

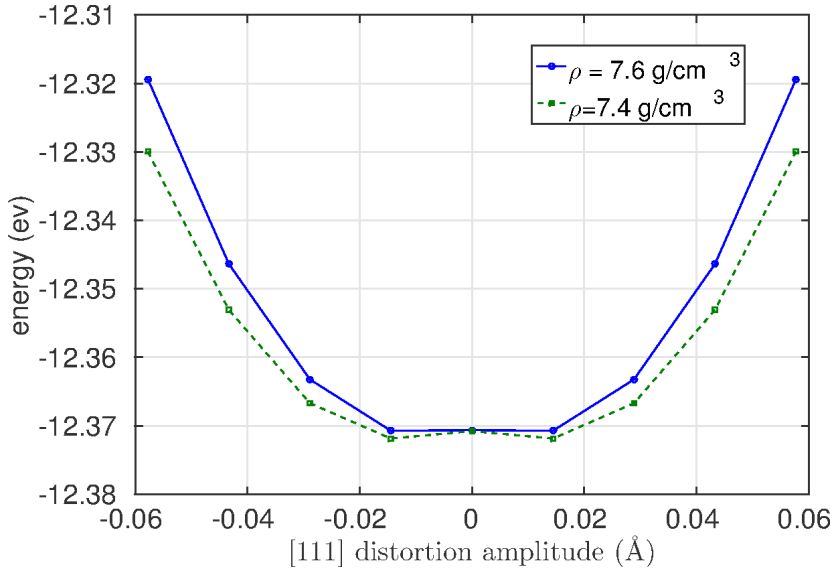

Figure A.17: Onset of susceptibility to small distortion towards rhombohedral structure marking continuous transition from metallic to multicenter bonding

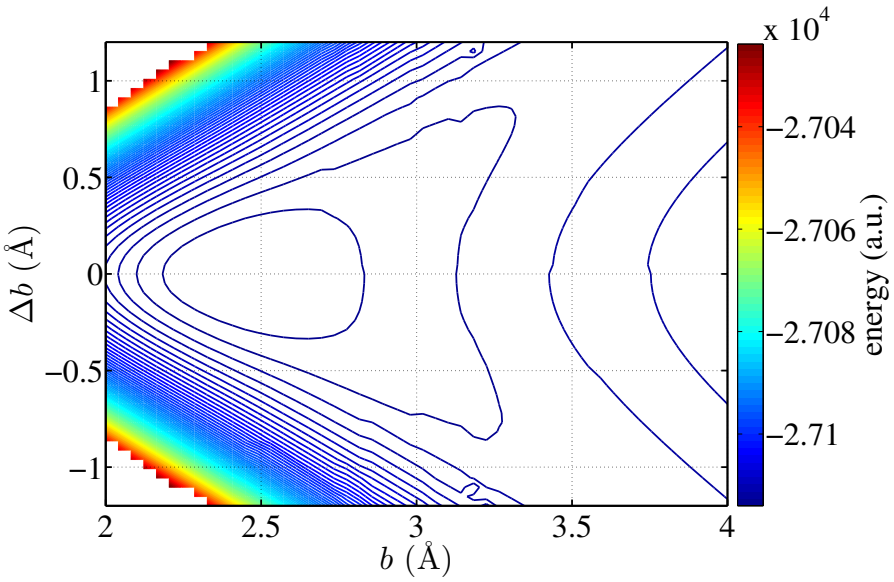

Figure A.18: Energy contour plot obtained from HF solutions using NWChem, for central As displacement as a function of average bond length $b = (b_1 + b_2)/2$. Energy units on color bar are atomic units (a.u.)

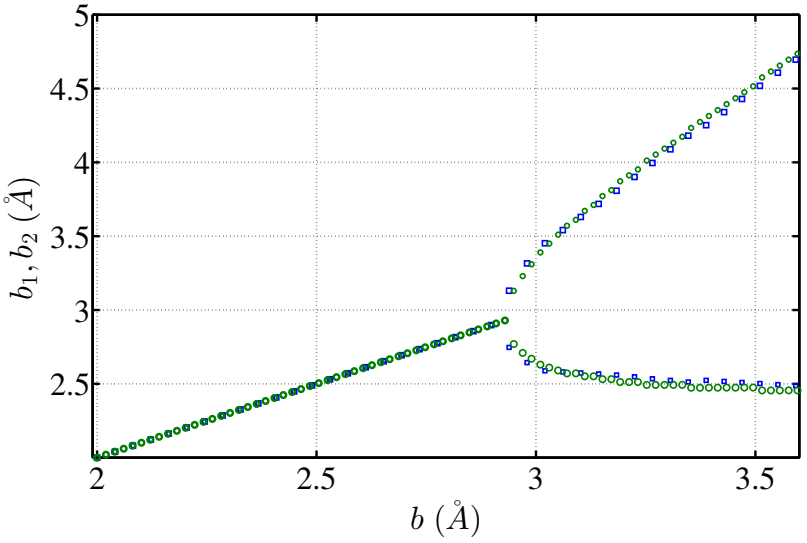

Figure A.19: Bond length plot obtained for the AsH_2-AsH-AsH_2 trimer from the potential energy surface for displacement of the central As atom. The bond lengths are developed from the minimum energy contour. Circles show semi-empirical PM6 method data, squares represent ab-initio HF data obtained with NWChem using the aug-cc-pvtz-pp basis and small core pseudo-potential.

```
NATURAL BOND ORBITAL ANALYSIS:

                          Occupancies       Lewis Structure    Low   High
         Max    Occ     --------------------  -----------------   occ   occ
 Cycle  Ctr   Thresh    Lewis    non-Lewis     CR  BD  nC  LP    (L)   (NL)
 ============================================================================
    1     2     1.90   102.60330   1.39670     42   5   0   5     2      2
    2     2     1.84   103.62410   0.37590     42   7   0   3     0      2
    3     2     1.83   102.62588   1.37412     42   5   0   5     1      2
    4     2     1.84   103.62410   0.37590     42   7   0   3     0      2
 ----------------------------------------------------------------------------

 Structure accepted: No low occupancy Lewis orbitals

 -----------------------------------------------------
   Core                    83.99723 ( 99.997% of  84)
   Valence Lewis           19.62688 ( 98.134% of  20)
  ==================      ============================
   Total Lewis            103.62410 ( 99.639% of 104)
  -----------------------------------------------------
   Valence non-Lewis        0.36772 (  0.354% of 104)
   Rydberg non-Lewis        0.00817 (  0.008% of 104)
  ==================      ============================
   Total non-Lewis          0.37590 (  0.361% of 104)
 -----------------------------------------------------


     (Occupancy)   Bond orbital / Coefficients / Hybrids
48. (1.84005) BD ( 1)As  1-As  4
              ( 30.41%)   0.5514*As  1 s(  1.59%)p61.82( 98.39%)d 0.01(  0.02%)
                                       0.0000  0.0000  0.0000  0.1224 -0.0305
                                       0.0037 -0.0001  0.0000  0.0000  0.0000
                                       0.0148  0.0152 -0.0009  0.0004  0.0000
                                       0.0000  0.0000  0.0449  0.0098 -0.0005
                                       0.0005 -0.0001  0.0000  0.0000  0.9881
                                      -0.0704 -0.0069  0.0002  0.0000  0.0000
                                      -0.0001  0.0000 -0.0045  0.0000 -0.0024
                                       0.0000 -0.0004  0.0000  0.0133
              ( 69.59%)   0.8342*As  4 s( 38.13%)p 1.62( 61.86%)d 0.00(  0.01%)
                                       0.0000  0.0000  0.0000  0.6174 -0.0109
                                       0.0001  0.0000  0.0000  0.0000  0.0000
                                      -0.3438 -0.0157 -0.0010 -0.0007  0.0000
                                       0.0000  0.0000  0.0115 -0.0002  0.0000
                                       0.0000  0.0000  0.0000  0.0000 -0.7067
                                       0.0234 -0.0004  0.0022 -0.0001  0.0000
                                       0.0001  0.0000 -0.0001  0.0000  0.0002
                                       0.0000 -0.0051  0.0000  0.0054
50. (1.84005) BD ( 1)As  4-As  6
              ( 69.59%)   0.8342*As  4 s( 38.13%)p 1.62( 61.86%)d 0.00(  0.01%)
                                       0.0000  0.0000  0.0000  0.6174 -0.0109
                                       0.0001  0.0000  0.0000  0.0000  0.0000
                                      -0.3438 -0.0157 -0.0010 -0.0007  0.0000
                                       0.0000  0.0000  0.0115 -0.0002  0.0000
                                       0.0000  0.0000  0.0000  0.0000  0.7067
                                      -0.0234  0.0004 -0.0022  0.0001  0.0000
                                       0.0001  0.0000  0.0001  0.0000 -0.0002
                                       0.0000 -0.0051  0.0000  0.0054
              ( 30.41%)   0.5514*As  6 s(  1.59%)p61.82( 98.39%)d 0.01(  0.02%)
                                       0.0000  0.0000  0.0000  0.1224 -0.0305
                                       0.0037 -0.0001  0.0000  0.0000  0.0000
                                       0.0148  0.0152 -0.0009  0.0004  0.0000
                                       0.0000  0.0000  0.0449  0.0098 -0.0005
                                       0.0005 -0.0001  0.0000  0.0000 -0.9881
                                       0.0704  0.0069 -0.0002  0.0000  0.0000
                                      -0.0001  0.0000  0.0045  0.0000  0.0024
                                       0.0000 -0.0004  0.0000  0.0133
```

Figure A.20: NBO6 localized molecular orbital analysis within Gaussian09 for symmetric trimer at $b = 3.2$ $\mathring{A}$.

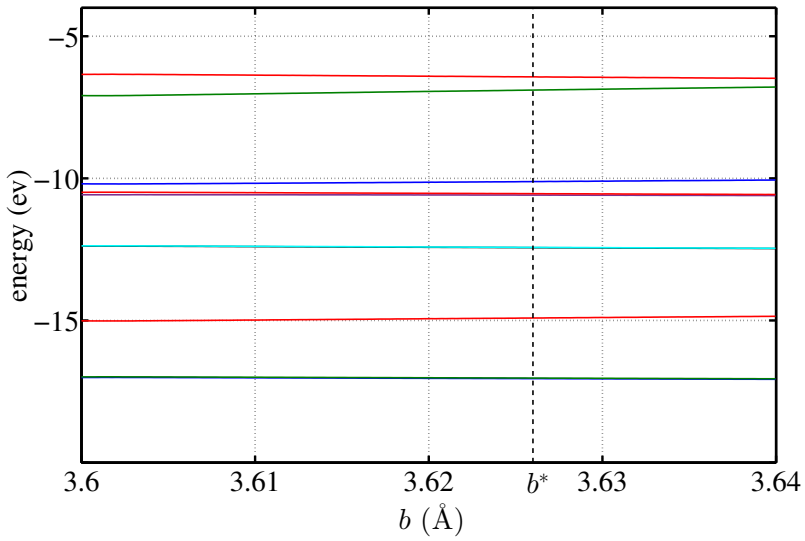

Figure A.21: Molecular orbital terms near the HOMO for a symmetric AsH_2-AsH-AsH_2 trimer as it undergoes dilation, b indicates the average bond length per atom above which symmetry is broken.

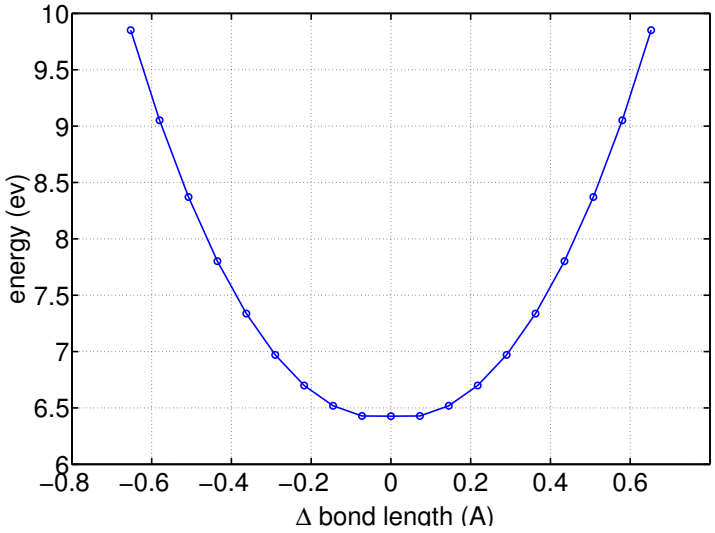

Figure A.22: At high density where every interatomic region hosts a 2-center localized bond orbital, the total energy of the molecule is stable with respect to displacement of every other atom (dimerization). The central minimum shows that a symmetry lowering distortion (bond length alternation) is energetically costly.

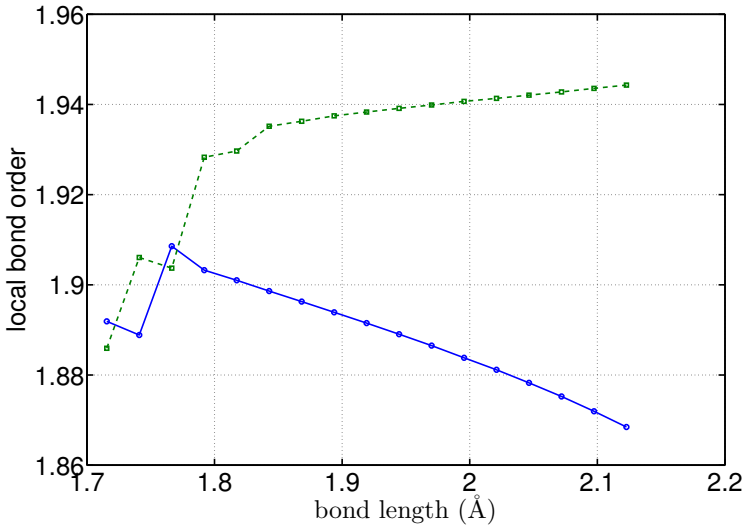

Figure A.23: At high density the two sets of LMOs have nearly identical bond order, as the ring molecule is dilated, the symmetry is broken and one set of LMOs retains 2-center character as demonstrated by BO ≈ 2 while the other set gradually decreases.

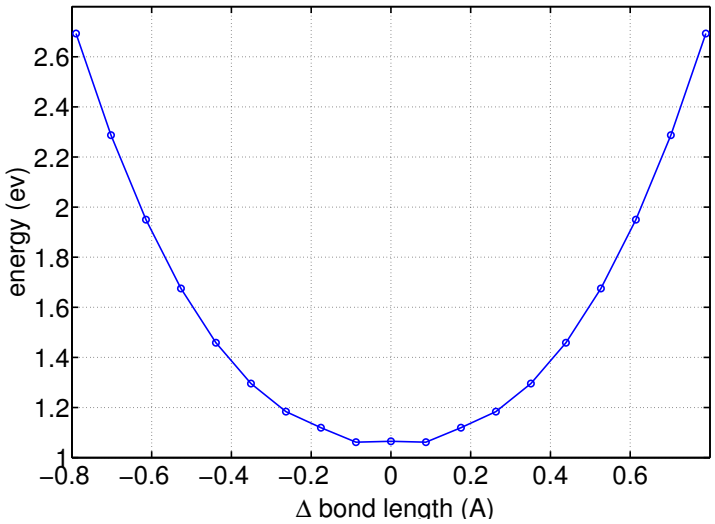

Figure A.24: Coincident with breaking of bond order symmetry a non-central minimum develops in the potential energy scan, bond length alternation is favored below this density.

Bibliography

[1] Gregory A. Landrum and Roald Hoffmann. Secondary bonding between chalcogens or pnicogens and halogens. *Angew. Chem. Int. Ed.*, 37:1887–1890, 1998.

[2] T. Petrenko and F. Neese. The ORCA program system. WIRES - Comput. Mol. Sci., 2012.

[3] E. F. Valeev. A library for the evaluation of molecular integrals of many-body operators over gaussian functions. http://libint.valeyev.net/, 2014.

[4] M. P. Lightfoot C. R. Groom, I. J. Bruno and S. C. Ward. The cambridge structural database. *Acta Cryst.*, B72, 2016.

[5] P. Hohenberg and W. Kohn. Inhomogeneous electron gas. *Phys. Rev.*, 136:B864–B871, 1964.

[6] N. F. Mott. *Metal-Insulator Transitions.* Taylor and Francis, London, 1990.

[7] V. Lubchenko. Theory of the structural glass transition: A pedagogical review. *Adv. Phys.*, 64:283–443, 2015.

[8] A. Zhugayevych and V. Lubchenko. An intrinsic formation mechanism for midgap electronic states in semiconductor glasses. *J. Chem. Phys.*, 132:044508, 2010.

[9] A. Zhugayevych and V. Lubchenko. Electronic structure and the glass transition in pnictide and chalcogenide semiconductor alloys. I: The formation of the $pp\sigma$-network. *J. Chem. Phys.*, 133:234503, 2010.

[10] A. Zhugayevych and V. Lubchenko. Electronic structure and the glass transition in pnictide and chalcogenide semiconductor alloys. II: The intrinsic electronic midgap states. *J. Chem. Phys.*, 133:234504, 2010.

[11] Gilbert N. Lewis. Valence and tautomerism. *J. Amer. Chem. Soc.*, 35(10):1448–1455, 1913.

[12] Pekka Pyykkö. Strong closed-shell interactions in inorganic chemistry. *Chem. Rev.*, 97:597–636, 1997.

[13] N.W. Alcock. Secondary bonding to nonmetallic elements. *Adv. Inorg. Chem. Radiochem.*, 15:1–58, 1972.

[14] Garegin A. Papoian and Roald Hoffmann. Hypervalent bonding in one, two, and three dimensions: Extending the zintl-klemm concept to nonclassical electron-rich networks. *Angew. Chem. Int. Ed.*, 39:2408–2448, 2000.

[15] R. E. Rundle. On the Problem Structure of XeF_4 and XeF_2. *J. Amer. Chem. Soc.*, 85:112–113, 1963.

[16] George C. Pimentel. The bonding of trihalide and bifluoride ions by the molecular orbital method. *J. Chem. Phys.*, 19:446–448, 1951.

[17] J. I. Musher. The chemistry of hypervalent molecules. *Angew. Chem. internat. Edit.*, 8:54–68, 1969.

[18] W. Conard Fernelius and Richard F. Robey. The nature of the metallic state. *J. Chem. Ed.*, 12:53, 1935.

[19] A. E. van Arkel. *Molecules and Crystals in Inorganic Chemistry*. Interscience, 1956.

[20] J. A. A. Ketelaar. *Chemical Constitution: An Introduction to the Theory of the Chemical Bond*. Elsevier, 1958.

[21] J K Burdett. *Chemical Bonding in Solids*. Oxford University Press, 1995.

[22] Gordon F. Miller. *Structure and Bonding at the Zintle Border*, pages 1–59. VCH, 1996.

[23] F. R. Wagner, D. Bende, and Yu. Grin. Heteropolar bonding and a position-space representation of the 8 - n rule. *Dalton Trans.*, 45:3236–3243, 2016.

[24] J. Schmalian and P. G. Wolynes. Electronic mayonnaise: Uniting the sciences of "hard" and "soft" matter. *MRS Bull.*, 30:433, 2005.

[25] Thomas A. Albright, Jeremy K. Burdett, and Myung-Hwan Whangbo. *Orbital Interactions in Chemistry*. Wiley, Hoboken, NJ, 2013.

[26] Leland C. Allen and Jeremy K. Burdett. The Metallic BondDead or Alive? A Comment and a Reply. *Angew. Chem. Int. Ed. Eng.*, 34:2003–2003, 1995.

[27] P. W. Anderson. Absence of Diffusion in Certain Random Lattices. *Phys. Rev.*, 109:1492–1505, 1958.

[28] N. F. Mott. *Conduction in Non-crystalline Materials*. Clarendon Press, Oxford, 1993.

[29] L. D. Landau and E. M. Lifshitz. *Statistical Mechanics*. Pergamon Press, New York, 1980.

[30] N. Goldenfeld. *Lectures on phase transitions and the renormalization group*. Addison-Wesley, Reading, MA, 1992.

[31] P. Ehrenfest and T. Ehrenfest. *The Conceptual Foundations of the Statistical Approach in Mechanics*. Dover, 1990.

[32] Patricia Silas, Jonathan R. Yates, and Peter D. Haynes. Density-functional investigation of the rhombohedral to simple-cubic phase transition of arsenic. *Phys. Rev. B*, 78:174101, 2008.

[33] Enric Canadell and Myung-Hwan Whangbo. Conceptual aspects of structure-property correlation and electronic instabilites, with applications to low-dimensional transition-metal oxides. *Chem. Rev*, 91:965–1034, 1991.

[34] Michael E. Fisher. Renormalization group theory: Its basis and formulation in statistical physics. *Rev. Mod. Phys.*, 70:653–681, 1998.

[35] Kenneth G. Wilson. The renormalization group and critical phenomena. *Rev. Mod. Phys.*, 55:583–600, 1983.

[36] Tanja Graf, Claudia Felser, and Stuart S.P. Parkin. Simple rules for the understanding of heusler compounds. *Progress in Solid State Chemistry*, 39:1 – 50, 2011.

[37] V.V. Romaka, P. Rogl, L. Romaka, Yu. Stadnyk, A. Grytsiv, O. Lakh, and V. Krayovskii. Peculiarities of structural disorder in Zr- and Hf-containing Heusler and half-Heusler stannides. *Intermetallics*, 35:45 – 52, 2013.

[38] W. Cochran. Crystal stability and the theory of ferroelectricity. *Phys. Rev. Lett.*, 3:412–414, 1959.

[39] Martin T. Dove. Theory of displacive phase transitions in minerals. *Am. Mineral.*, 82:213–244, 1997.

[40] *MOPAC2012, James J.P. Stewart, Stewart Computational Chemistry, Colorado Springs, CO, USA, HTTP://OpenMOPAC.net*, 2012.

[41] M. Valiev, E.J. Bylaska, N. Govind, K. Kowalski, T.P. Straatsma, H.J.J. van Dam, D. Wang, J. Nieplocha, E. Apra, T.L. Windus, and W.A. de Jong. NWChem: a comprehensive and scalable open-source solution for large scale molecular simulations, 2010.

[42] J B Bersuker. *The Jahn-Teller Effect*. Cambridge, 2006.

[43] István Hargittai and Magdolna Hargittai. Lev d. landau (1908–1968): in memoriam. *Struct. Chem.*, 19:181–184, 2008.

[44] D.-K. Seo and Roald Hoffmann. What determines the structures of the group 15 elements? *J. Sol. State Chem.*, 147:26–36, 1999.

[45] S. F. Boys. Construction of some molecular orbitals to be approximately invariant for changes from one molecule to another. *Rev. Mod. Phys.*, 32:296–299, 1960.

[46] C. Edmiston and K. Ruedenberg. Localized atomic and molecular orbitals. *Rev. Mod. Phys.*, 35, 1963.

[47] W. Von Niessen. Density localization of atomic and molecular orbitals. *J. Chem. Phys.*, 56, 1972.

[48] E.D. Glendening, J.K. Badenhoop, A.E. Reed, J.E. Carpenter, J.A. Bohmann, C.M. Morales, C.R. Landis, and F. Weinhold. NBO 6.0, 2013. Theoretical Chemistry Institute, University of Wisconsin, Madison.

[49] Jon C. Golden and Vassiliy Lubchenko. Bond assignment as a symmetry breaking. submitted to JACS.

[50] E. Clementi, D.L. Raimondi, and W.P. Reinhardt. Atomic screening constants from scf functions. ii. atoms with 37 to 86 electrons. *J. Chem. Phys.*, 47:1300–1307, 1967.

[51] M. J. Rice and E. J. Mele. Elementary excitations of a linearly conjugated diatomic polymer. *Phys. Rev. Lett.*, 49:1455–1459, 1982.

[52] Eugene J. Mele and Michael J. Rice. Vibrational excitations of charged solitons in polyacetylene. *Phys. Rev. Lett.*, 45:926–929, 1980.

[53] A. J. Heeger, S. Kivelson, J. R. Schrieffer, and W. P. Su. Solitons in conducting polymers. *Rev. Mod. Phys.*, 60:781–850, 1988.

[54] R. E. Peierls. *Quantum Theory of Solids*. Clarendon Press, Oxford, 1955.

[55] Jeremy K. Burdett and Timothy J. McLarnan. A study of the arsenic, black phosphorus, and other structures derived from rock salt by bond-breaking processes. I. Structural enumeration. *J. Chem. Phys.*, 75(12):5764–5773, 1981.

[56] Jeremy K. Burdett, Peter Haaland, and Timothy J. McLarnan. A study of the arsenic, black phosphorus, and other structures derived from rock salt by bond-breaking processes. ii. band structure calculations and the importance of the gauche effect. *J. Chem. Phys.*, 75:5774–5781, 1981.

[57] J K Burdett and Stephen Lee. Peierls distortions in Two and Three Dimensions and the Structures of AB Solids. *J. Amer. Chem. Soc.*, 105:1079, 1983.

[58] Shunli Shang, Yi Wang, Hui Zhang, and Zi-Kui Liu. Lattice dynamics and anomalous bonding in rhombohedral as: First-principles supercell method. *Phys. Rev. B*, 76(5):052301, 2007.

[59] Hannelore Katzke and Pierre Tolédano. Displacive mechanisms and order-parameter symmetries for the A7-incommensurate-bcc sequences of high-pressure reconstructive phase transitions in Group Va elements. *Phys. Rev. B*, 77:024109, 2008.

[60] R. S. Berry, S. A. Rice, and J. Ross. *Physical Chemistry*. John Wiley & Sons, Hoboken, NJ, 1980.

[61] L. D. Landau and E. M. Lifshitz. *Quantum Mechanics*. Pergamon Press, 1981.

[62] P. G. Perkins and J. J. P. Stewart. A new rapid method for orbital localisation. *J. Chem. Soc., Faraday Trans. II*, 76:520–533, 1980.

[63] Ho Yin Chan and Vassiliy Lubchenko. Pressure in the landau-ginzburg functional: Pascals law, nucleation in fluid mixtures, a meanfield theory of amphiphilic action, and interface wetting in glassy liquids. *J. Chem. Phys.*, 143:124502, 2015.

[64] E. Abrahams, P. W. Anderson, D. C. Licciardello, and T. V. Ramakrishnan. Scaling theory of localization: Absence of quantum diffusion in two dimensions. *Phys. Rev. Lett.*, 42:673–676, 1979.

[65] L. Landau. On the theory of phase transitions i. *Phys. Z. Sowjet.*, 11:26, 1937. English translation in "Collected Papers of Landau", 1965, Gordon and Breach.

[66] S. A. Brazovskii. Phase transition of an isotropic system to a non-unifrom state. *JETP*, 41:85–89, 1975.

[67] Y. Singh, J. P. Stoessel, and P. G. Wolynes. The hard sphere glass and the density functional theory of aperiodic crystals. *Phys. Rev. Lett.*, 54:1059–1062, 1985.

[68] Michael E. Fisher and B. Widom. Decay of correlations in linear systems. *J. Chem. Phys.*, 50:3756–3772, 1969.

[69] A.D. Becke and K.E. Edgecombe. A simple measure of electron localization in atomic and molecular systems. *J. Chem. Phys.*, 92, 1990.

[70] B. Silvi and A. Savin. Classification of chemical bonds based on topological analysis of electron localization functions. *Nature*, 371, 1994.

[71] B. Silvi and C. Gatti. Direct space representation of the metallic bond. *J. Phys. Chem. A*, 104, 2000.

[72] G.C. Allen, C.J. Carmalt, A.H. Cowley, A.L. Hector, S. Kamepalli, Y.G. Lawson, N.C. Norman, I.P. Parkin, and L.K. Pickard. Preparation and characterization of a material composition bip (bismuth phosphide) and other intergroup 15 element phases. *Chem. Mater*, 9, 1997.

[73] Stephen Lee and Roald Hoffmann. Bcc and Fcc Transition Metals and Alloys: A Central Role for the JahnTeller Effect in Explaining Their Ideal and Distorted Structures. *J. Amer. Chem. Soc.*, 124:4811–4823, 2002.

[74] Wojciech Grochala, Roald Hoffmann, Ji Feng, and NeilW. Ashcroft. The chemical imagination at work in very tight places. *Angew, Chem. Int. Ed.*, 46:3620–3642, 2007.

[75] CT Prewitt and RT Downs. High-pressure crystal chemistry. *Rev. Mineral.*, 37:283–317, 1998.

[76] Thomas Weber, Julia Dshemuchadse, Miroslav Kobas, Matthias Conrad, Bernd Harbrecht, and Walter Steurer. Large, larger, largest – a family of cluster-based tantalum copper aluminides with giant unit cells. I. Structure solution and refinement. *Acta Crystallogr. B*, 65:308–317, 2009.

[77] Julia Dshemuchadse, Sandro Bigler, Arkadiy Simonov, Thomas Weber, and Walter Steurer. A new complex intermetallic phase in the system Al–Cu–Ta with familiar clusters and packing principles. *Acta Crystallogr. B*, 69:238–248, 2013.

[78] H. W. Cahn and J. E. Hilliard. Free Energy of Nonuniform System. I. Interfacial Free Energy. *J. Chem. Phys.*, 28:258–267, 1958.

[79] J. S. Rowlinson and B. Widom. *Molecular Theory of Capillarity*. Clarendon Press, Oxford, 1982.

[80] A. J. Bray. Theory of phase-ordering kinetics. *Adv. Phys.*, 43:357–459, 1994.

[81] W. Kohn and L. J. Sham. Self-consistent equations including exchange and correlation effects. *Phys. Rev.*, 140:A1133–A1138, 1965.

[82] Szafrański, Marek and Katrusiak, Andrzej. Mechanism of Pressure-Induced Phase Transitions, Amorphization, and Absorption-Edge Shift in Photovoltaic Methylammonium Lead Iodide. *J. Phys. Chem. Lett.*, 7:3458–3466, 2016.

[83] M. Mézard and G. Parisi. *Glasses and Replicas*, pages 151–191. John Wiley & Sons, Hoboken, NJ, 2012.

[84] J. Schmalian and P. G. Wolynes. Stripe glasses: Self-generated randomness in a uniformly frustrated system. *Phys. Rev. Lett.*, 85:3456, 2001.

[85] D. Bevzenko and V. Lubchenko. Stress distribution and the fragility of supercooled melts. *J. Phys. Chem. B*, 113:16337–16345, 2009.

[86] Pierfrancesco Urbani and Giulio Biroli. Gardner transition in finite dimensions. *Phys. Rev. B*, 91:100202, 2015.

[87] Matthew S. Dyer, Christopher Collins, Darren Hodgeman, Philip A. Chater, Antoine Demont, Simon Romani, Ruth Sayers, Michael F. Thomas, John B. Claridge, George R. Darling, and Matthew J. Rosseinsky. Computationally assisted identification of functional inorganic materials. *Science*, 340:847–852, 2013.

[88] Christopher C. Fischer, Kevin J. Tibbetts, Dane Morgan, and Gerbrand Ceder. Predicting crystal structure by merging data mining with quantum mechanics. *Nature Materials*, 5:641–646, 2006.

[89] P Villars, K Brandenburg, M Berndt, S LeClair, A Jackson, Y.-H Pao, B Igelnik, M Oxley, B Bakshi, P Chen, and S Iwata. Binary, ternary and quaternary compound former/nonformer prediction via Mendeleev number. *J. Alloys Comp.*, 317–318:26 – 38, 2001.

[90] Sason Shaik, Henry S. Rzepa, and Roald Hoffmann. One molecule, two atoms, three views, four bonds? *Angewandte Chemie International Edition*, 52:3020–3033, 2013.

[91] P.G. Perkins and J.J.P. Stewart. A new rapid method for orbital localisation. *J. Chem. Soc., Faraday Trans.*, 78, 1982.

[92] I. N. Levine. *Quantum chemistry*. Prentice Hall, 2009. 6th edition, page 714.

[93] Gregory A. Landrum, Norman Goldberg, and Roald Hoffmann. Bonding in the trihalides (x_3^-), mixed trihalides (x_2y^-) and hydrogen bihalides (x_2h^-). the connection between hypervalent, electron-rich three-center, donor-acceptor and strong hydrogen bonding [double dagger]. *J. Chem. Soc., Dalton Trans.*, pages 3605–3613, 1997.

[94] Jon C. Golden and Vassiliy Lubchenko. The chemical bond as an emergent phenomenon. submitted to JACS.

[95] D.R. Armstrong, P.G. Perkins, and J.J.P. Stewart. Bond indices and valency. *J.C.S. Dalton*, 627, 1972.

[96] http://openmopac.net/manual/index.html.

[97] M. J. S. Dewar and W. Thiel. Ground states of molecules. 39. mndo results for molecules containing hydrogen, carbon, nitrogen adn oxygen. *J. Am. Chem. Soc.*, 99:4907–4917, 1977.

[98] J. J. P. Stewart. Optimization of parameters for semiempirical methods v: Modification of NDDO approximations and application to 70 elements. *J. Mol. Model.*, 13:1173–1213, 2007.

[99] Jennifer R. Casey, Argyris Kahros, and Benjamin J. Schwartz. To be or not to be in a cavity: The hydrated electron dilemma. *J. Phys. Chem. B*, 117:14173–14182, 2013.

[100] Dor Ben-Amotz. Unveiling electron promiscuity. *J. Phys. Chem. Lett.*, 2:1216–1222, 2011.

[101] László Turi and Peter J. Rossky. Theoretical studies of spectroscopy and dynamics of hydrated electrons. *Chem. Rev.*, 112:5641–5674, 2012.

[102] N. David Mermin. Thermal properties of the inhomogeneous electron gas. *Phys. Rev.*, 137:A1441–A1443, 1965.

[103] R. Farchioni, G. Grosso, and P. Vignolo. *Recursive Algorithms for Polymeric Chains*, volume 41 of *Springer Series in Materials Science*, pages 89–126. Springer-Verlag, Berlin, Heidelberg, 2001.

[104] M. Steślicka. *Kronig-Penney Model (for Surface States)*, volume 5 part 2, pages 158–259. Pergamon Press, Oxford, 1974.

[105] Felix Plasser, Matthias Ruckenbauer, Sebastian Mai, Markus Oppel, Philipp Marquetand, and Leticia González. Efficient and Flexible Computation of Many-Electron Wave Function Overlaps. *J. Chem. Theory Comput.*, 12(3):1207–1219, 2016.

[106] D. M. McQuarrie. *Statistical Mechanics*. Harper-Collins, New York, 1973.

[107] Eduardo Fradkin and Jorge E. Hirsch. Phase diagram of one-dimensional electron-phonon systems. i. the su-schrieffer-heeger model. *Phys. Rev. B*, 27:1680–1697, 1983.

[108] D. N. Zubarev. 2-time Green Functions in Statistical Physics. *Sov. Phys. Uspekhi*, 3:320, 1960.

[109] P. M. Chaikin and T. C. Lubensky. *Principles of Condensed Matter Physics*. Cambridge University Press, Cambridge, 2000.

[110] GD Stucky, SR Marder, and JE Sohn. Linear and nonlinear polarizability. In SR Marder, JE Sohn, and GD Stucky, editors, *Materials for Nonlinear Optics: Chemical Perspectives*, volume 455 of *ACS Symposium Series*, pages 2–30, 1991.

[111] V. Lubchenko and J. Golden. Degenerate charge density waves: From a continuum theory of miscibility to the metal-insulator transition, quantum glasses, acid-base chemistry, and high temperature superconductivity. *unpublished*, 2016.

[112] N. F. Mott and E. A. Davis. *Electronic Processes in Non-crystalline Materials*. Clarendon Press, Oxford, 1979.

[113] S. Alexander and J. McTague. Should all crystals be bcc? landau theory of solidification and crystal nucleation. *Phys. Rev. Lett.*, 41:702–705, 1978.

[114] P. W. Anderson. *Concepts in Solids*. W. A. Benjamin, New York, 1963.

[115] Hajime Takayama, Y. R. Lin-Liu, and Kazumi Maki. Continuum model for solitons in polyacetylene. *Phys. Rev. B*, 21:2388–2393, 1980.

[116] T. R. Kirkpatrick, D. Thirumalai, and P. G. Wolynes. Scaling concepts for the dynamics of viscous liquids near an ideal glassy state. *Phys. Rev. A*, 40:1045–1054, 1989.

[117] M.J. Rice and E.J. Mele. Elementary excitations of a linearly conjugated diatomic polymer. *Phys. Rev. Lett.*, 49, 1982.

[118] Andriy Zhugayevych and Vassiliy Lubchenko. Electronic structure and the glass transition in pnictide and chalcogenide semiconductor alloys. *J. Chem. Phys.*, 132:234503–1,16, 2010.

[119] A.A. Voityuk and N. Rosch. Am1/d parameters for molybdenum. *J. Phys. Chem. A*, 104, 2000.